Point Defects in Carbon Nanostructures Studied by *in-situ* Electron Microscopy

Dissertation

zur Erlangung des Grades
"Doktor der Naturwissenschaften"
im Promotionsfach Chemie

Am Fachbereich
Chemie, Pharmazie und Geowissenschaften
der Johannes Gutenberg-Universität Mainz

Yanjie Gan
geb. in Anhui Province / V. R. China

Mainz, 2008

Contents

Chapter 1 Introduction

It was well known that there are two types of carbon crystalline structure, the natural allotropes diamond and graphite, until Kroto *et al* discovered fullerenes (C_{60}) in the mid 1980s [1]. This momentous discovery inspired the unprecedented worldwide activity in the investigation of elemental carbon and started a new era in carbon material [2–5]. The most important success in this research was the discovery of carbon nanotubes by Iijima in 1991 [6]. Carbon nanotubes and C_{60} have to be investigated with very precise instruments. Transmission electron microscopy (TEM) is one of them. It can not only characterize nanostructures with high resolution, but also lead to the formation of unexpected and very exciting new structures. The discovery of the spherical carbon onions in 1992 by Ugarte during an electron irradiation study of graphite soot is a convincing example [7]. Carbon nanostructures, including zero-dimensional carbon onions, one-dimensional carbon nanotubes and two-dimensional graphene layers, have been considered as some of the most promising and hottest research fields due to their novel mechanical, electronic, magnetic, and optical properties which can lead to extensive applications [8, 9].

Undoubtedly, TEM is the most powerful tool to study the size, morphology and structure of nanoparticles. Under the irradiation with electrons of high energy, structural alterations of the specimen are inevitable in some cases [10–12]. It turned out that carbon nanostructures are very sensitive to electron irradiation.

On the one hand, misinterpretations of the structural alterations due to electron irradiation should be avoided. On the other hand, electrons with high energy can also be used to form new exciting structures [7, 13] and obtain a lot of important information for further studies.

The effects of particle irradiation in solids have been studied for over 50 years, and the early study mainly focused on radiation damage in metals, semiconductors and insulators in nuclear technology. When solids are bombarded with particles (e.g., ions, electrons, neutrons, and protons, etc.) electrons may be excited, or the atoms may be knocked out of their sites. Furthermore, impurities may be introduced. As a result, solids under irradiation are apt to change their properties slightly or drastically.

Radiation damage in graphite which can be used as a reactor material has attracted much attention for several decades. However, the nature of defect agglomeration remained unknown for a long time, because the resolving ability of electron microscopes was insufficient for lattice imaging at that time. With the development of microscopy, especially the appearance of modern high-resolution electron microscopes, one can observe the structure of lattice defects on the atomic scale, and get a new understanding of irradiation defects in graphite and eventually in carbon nanostructures. Carbon nanostructures became preferred objects for irradiation investigations due not only to their technical importance but also to their unique ability to reconstruct after atom displacements under the electron beam. It is expected that irradiation has different effects in nanostructures than in bulk solids because of the large fraction of surface atoms and the general proximity of surfaces [14]. Generally, the atoms on the surface are much easier to be displaced than those within the bulk. Meanwhile, many earlier results on the formation and migration of point defects in graphitic structures [15, 16] are out-dated and a new treatment is required.

Earlier work has shown that irradiation can have beneficial effects on nanostructural materials when combined with heat treatment. Irradiation-mediated engineering, self-assembly and self-organization in carbon nanostructures are examples [17–21]. The structure and morphology of carbon nanostructures can be tailored by irradiation [7, 13, 22–26], and they can be interconnected with each other or merged in a controllable way with nearly atomic precision [22, 25, 27, 28]. Irradiation can also lead to extremely high pressure inside multi-walled carbon nanotubes (MWCNTs) [29] and spherical carbon onions [13], and make these nanostructures be useful as compression cells to induce high-pressure transformations of materials on nanometer scale. Even diamond can nucleate and grow under an intense electron or ion beam inside carbon onions [13, 30–32].

Under an intense electron irradiation carbon nanotubes can be cut or bent by a predefined angle. Even single-walled carbon nanotube (SWCNT) bundles can be transformed to MWCNTs and MWCNTs can locally be transformed to an onion-like bulge [33]. Moreover, SWCNTs can be merged with each other to form a nanotube junction [28] or a new tube with a double diameter [25]. In addition, irradiation can be used to tailor the mechanical [23], electronical [24, 34–36], and magnetic [37, 38] properties of carbon nanostructures. All these phenomena result from a delicate balance

between defect creation, migration and annealing during irradiation. Therefore, detailed knowledge about migration and annihilation of defects in nanostructured carbon materials is indispensable.

In this work, point defects induced by electron irradiation in carbon nanostructures, including carbon onions, nanotubes and graphene layers, were investigated by *in-situ* TEM. The prominent advantage of the study of point defects by *in-situ* TEM is that point defects can be generated and their evolution can be recorded in a real time at atomic resolution with the same electron beam.

1.1 Irradiation Effects

Different mechanisms of energy or momentum transfer take place, when a high-energetic particle such as an electron or ion strikes the atoms of a target. The most important primary radiation effects are [17]:

- electronic excitation or ionization of individual atoms,
- collective electronic excitations, e.g., plasmons,
- breakage of bonds or cross-linking,
- generation of phonons, leading to a heating of the target,
- displacement of atoms in the bulk of the target,
- sputtering of atoms from the surface.

Secondary effects are:

- emission of photons, e.g., X-rays or visible light,
- emission of secondary or Auger electrons, leading to a charging of the target.

Here, one important concept has to be introduced: the cross section σ in units of barns (1 barn = 10^{-28} m^2). It expresses the likelihood of the respective interactions between the particles and reflects how important this interaction is. It depends on the energy of the projectile particle and the specimen material.

Here, we will focus on electron irradiation effects in carbon materials, so it is useful to divide these contributions into two groups: knock-on effects, which result in the displacements of atoms, and electronic excitations. The possibility of *in-situ* observation makes electron beams more suitable than ions as projectiles.

In insulators electronic excitations are essential, so that ionization can play the dominant role. In metals knock-on atom displacements are substantial, and excitation effects become unimportant because of the presence of conduction electrons, so that metals are more stable than insulators under irradiation, particularly at low projectile energies. Graphite is a semi-metal and behaves like metals under irradiation where knock-on atom displacements are the main source of radiation damage and ionization is negligible. It turns out that knock-on atom displacements dominate in all graphitic nanostructures [17–21]. However, diamond is an insulator, and behaves completely different from graphite.

Generally, with the increase of the projectile energy knock-on effects become more and more significant due to the occurrence of displacement cascades, whereas excitations are less important. It is worthy to be noted that it is impossible for atoms to be displaced by an electron beam with the energy below a certain threshold energy. Thermal effects caused by irradiation can be neglected in TEM, because the mean free path of the electrons in typical specimen materials is much larger than the specimen thickness for TEM studies, which leads to the dissipation of only a very small fraction of the electron energy in the specimen.

Knock-on Displacements

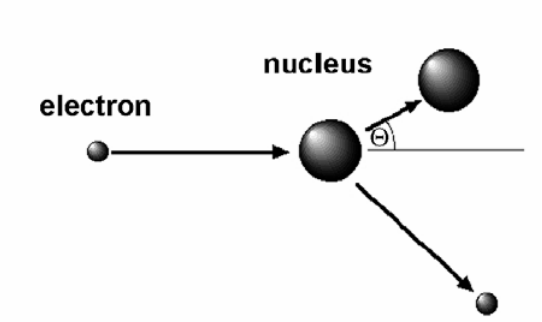

Figure 1.1: Schematic drawing of scattering of an electron at a nucleus [17].

As mentioned above, knock-on atom displacements are the most substantial irradiation effect in carbon nanostructures. When energetic particles strike the nuclei of the atoms in a solid, a part of the energy of the particles is transferred to the atoms

because of the law of momentum conservation. Only when sufficient energy is transferred to break the bonds and to transfer the atoms onto interstitial sites, the atoms will leave their original lattice sites. This process is called atom displacement, as shown in Figure 1.1.

The energy T transferred to the nucleus depends on the scattering angle Θ:

$$T(\Theta) = T_{\max} \cos^2 \Theta \tag{1.1}$$

where $T_{\max}$ is the maximum energy transferred by a head-on collision ($\Theta = 0$). The law of momentum conservation gives $T_{\max}$ with correction of relativistic effects, as a function of the electron energy E:

$$T_{\max} = \frac{2E(E + 2m_e c^2)}{Mc^2} \tag{1.2}$$

where m_e is the electron mass, M is the nucleus mass, and c is the speed of light in vacuum. It is intuitively clear that a head-on collision has a rather low probability. Therefore, large-angle scattering dominates.

There are two cases according to the original position of the displaced atoms in a solid: at the surface or within the solid. Surface atoms can be ejected easily due to the open space on one side. However, for the atoms within a solid knock-on displacements are less likely. The atom has to be moved onto an interstitial site and neighboring atoms have to be shifted slightly. More energy is required to displace an atom from a lattice site within a solid than from a surface, as more bonds have to be broken to displace an atom inside. Only the sublimation energy transfer is required to eject an atom from the surface. The displaced atoms at the surface either leave the specimen completely, known as sputtering [39], or migrate on the surface. For sputtering the atoms must have high enough energy to leave the surface.

Another very important concept is the threshold energy T_d, the minimum energy transferred to the atom which is required to produce a stable so-called Frenkel pair (vacancy-interstitial pair). Frenkel pairs would be stable in the crystal when the interstitial-vacancy separation exceeds the recombination radius. Otherwise, they would recombine spontaneously. For displacements both the cross-section and the threshold energy depend on the direction of the electron beam relative to the crystal lattice. In rather open structures atoms are more easily displaced into open spaces in the lattice,

which means atoms prefer to be displaced into the space between the basal layers rather than within the layers for layered structures of graphite under irradiation.

A value of σ for light elements like carbon (assuming an isotropic displacement energy) can be given by [40]:

$$\sigma = \frac{4Z^2E_R^2}{m^2c^4}\left(\frac{T_{\max}}{T_d}\right)\pi a_0^2\left(\frac{1-\beta^2}{\beta^4}\right)\left\{1+2\pi\alpha\beta\left(\frac{T_d}{T_{\max}}\right)\right.$$
$$\left.-\frac{T_d}{T_{\max}}\left[1+2\pi\alpha\beta+\left(\beta^2+\pi\alpha\beta\right)\ln\left(\frac{T_{\max}}{T_d}\right)\right]\right\} \quad (1.3)$$

where Z is the atomic number of the displaced atom, E_R is the Rydberg energy (13.6 eV), a_0 is the Bohr radius of the hydrogen atom (5.3×10^{-11} m), $\beta = \upsilon/c$, $\alpha = Z/137$, T_d is the threshold energy and $T_{\max}$ is the maximum energy transferred by a head-on collision (Θ = 0, projectile particle is reflected backwards). As mentioned above, the displacement cross section, a meaningful parameter in the experimental studies, depends on the energy of the beam and the specimen material. It increases with the electron energy and the atomic number but decreases with increasing threshold energy.

The displacement rate p of each atom which shows how often each atom is displaced per second is given by:

$$p = \sigma j \quad (1.4)$$

where σ is the displacement cross section and j is the beam current density. Typical beam current densities in TEM range between 10 A/cm^2 for high-resolution imaging and 10^4 A/cm^2 for a fully focused beam in a field emission microscope. Then the displacement rates range between 10^{-3} displacements per atom per second (dpa/s) (j = 10 A/cm^2) and 1 dpa/s (j = 10^4 A/cm^2) with a displacement cross-section of 20 barns (graphite with $T_d \approx 17$ eV) [17].

Only head-on collisions are possible when the beam energy is just slightly above the displacement threshold energy, while large-angle scatterings dominate for higher beam energies. When the beam energy exceeds twice the displacement threshold energy, some of the displaced atoms may get enough energy to cause further displacement, so-called displacement cascades. Such a displacement cascade is important not only in ion irradiation, but also in high-energy electron irradiation experiments. At low displacement thresholds, many secondary displacements can take place, and the total displacement cross section is increased.

1.2 Defects

As mentioned above, various defects can be generated in solids when solids are irradiated by particles. In this section, the classifying and evolution of defects are presented.

1.2.1 Classifying of Defects

Defects are usually classified according to their dimensionality.

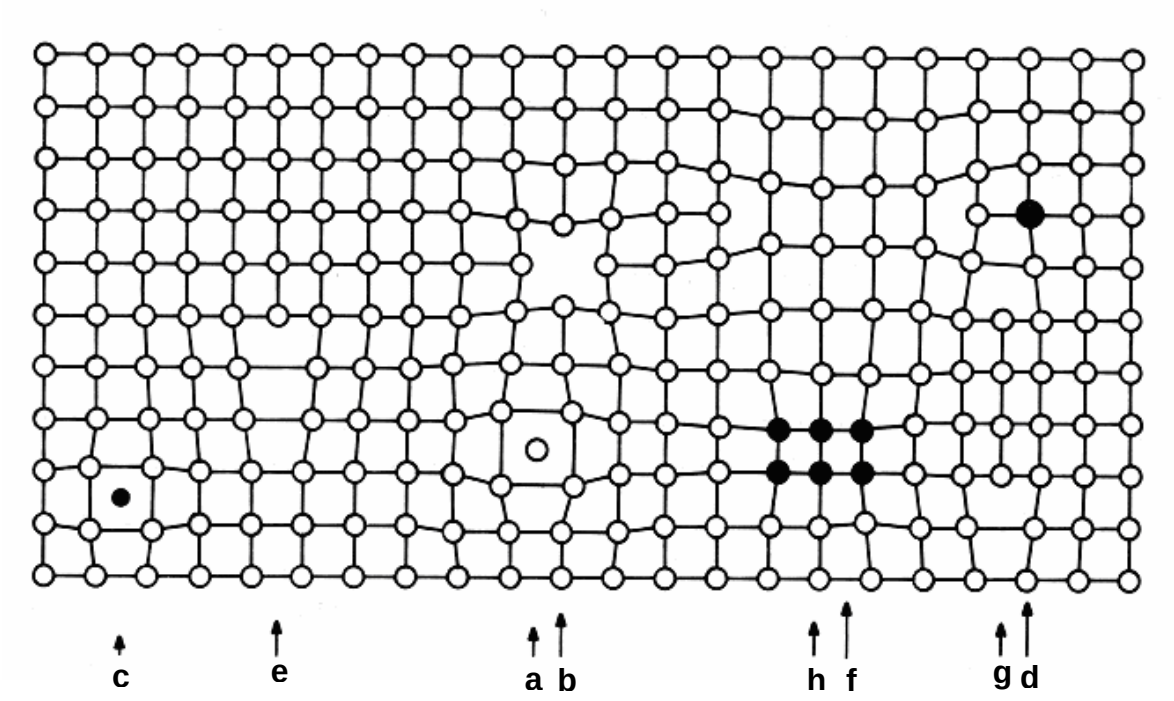

Figure 1.2: Schematic drawing of various crystal lattice defects [41].

Zero-dimensional defects

This kind of defect is normally called “point defect” or “atomic size defect”. Of most prominence are interstitials ((a) in Figure 1.2) and vacancies (b), which are the only intrinsic point defects in element crystals. A defect where the interstitial is close to the vacancy is called Frenkel pair. If extrinsic atoms are in the crystal lattice, there are another two kinds of defects: impurity atoms on interstitial sites (c) and on lattice sites (d).

One-dimensional defects

This kind of defect includes all kinds of dislocations, such as edge dislocations (e), and screw dislocations.

Two-dimensional defects

This includes grain boundaries, phase boundaries, stacking faults, vacancy type dislocation loops (f) and interstitial type dislocation loops (g).

Three-dimensional defects

This kind of defect is normally produced by the precipitation of impurity atoms or agglomeration of point defects.

In the following section, the defects generated under irradiation which are important in carbon nanostructures will be focused on.

1.2.2 Evolution of Defects

An energy transfer is required for the endothermal formation of defects in solids. It can be achieved either close to equilibrium at high temperatures or far from equilibrium by deformation or irradiation. As mentioned above, Frenkel pairs are stable in the crystal when the interstitial-vacancy separation exceeds the recombination radius. Single point defects can disappear in two ways: one is to annihilate with a point defect of the opposite sign, the other is to form clusters by aggregation with defects of the same sign. With increasing irradiation intensity, each configuration tends towards a dynamic equilibrium where the rate of recombination or aggregation of the defects is equal to their production rate.

The evolution of defects is mainly controlled by the mobility of interstitials and vacancies depending on the temperature. The temperature dependence of the diffusivity D of an interstitial or a vacancy follows an Arrhenius law:

$$D = D_0 \exp(-E_m / kT) \tag{1.5}$$

where D_0 is the pre-exponential factor (containing the migration entropy), E_m is the migration energy, k is Boltzmann's constant and T is the absolute temperature. The

mobility of the interstitials and vacancies increases with the temperature. Generally, the mobility of interstitials is higher than that of vacancies, because a rearrangement of the lattice by site exchange of atoms is required for the migration of vacancies. In the exchange process several bonds have to be broken. However, interstitials are located between the lattice sites and do not form bonds to adjacent atoms. The migration of interstitials and vacancies is generally anisotropic due to the particular symmetry of the crystal, which leads to the occurrence of some easier migration pathways.

Under continuous irradiation, the system reaches a saturation state depending on the temperature. Already existing defects accumulate, then new defects form clusters with the existing defects of same sign or recombine with those of opposite sign. Thus, the damage rate goes down to zero as soon as each new defect is generated within the recombination volume of an already existing defect or a cluster of opposite sign.

Point defects, interstitials and vacancies, have a tendency to aggregate into clusters to reduce their free energy. Agglomeration of the defects with the same sign is very important under irradiation at low temperatures. Once defect agglomerates form, annealing of damage is difficult and requires a very high temperature to disperse the agglomerates.

In electron microscopy studies of radiation phenomena, irradiation is normally carried out at specimen temperatures below 1500K, which is limited by the heating stages. At lower temperatures, interstitials have a much higher mobility than vacancies in carbon materials, which may result in an aggregation of interstitials between basal planes which have the largest spacing. However, at rather high temperatures, both interstitials and vacancies are mobile enough to recombine before an agglomeration happens.

1.3 Diffusion

So far, interstitials and vacancies, induced by electron irradiation in solids, have been introduced. These defects can jump from one position to another randomly. This process results in the transport of atoms and is called diffusion. Collisions by energetic electrons can lead to irradiation-induced diffusion.

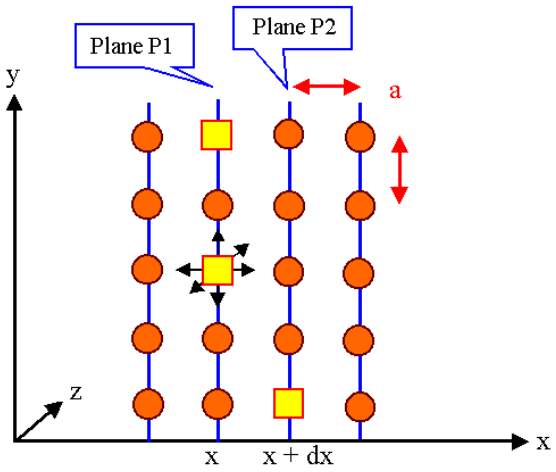

Figure 1.3: Schematic drawing of lattice planes with diffusing particles shown with squares [41].

At first, let us assume that jumps can be achieved with a frequency v and over a distance a within a time interval t. For random jumps, the mean diffusion distance is

$$\bar{x} = a\sqrt{n} = a\sqrt{vt} \tag{1.6}$$

where n is the number of jumps. Then, it is clear that the diffusion distance $\bar{x}$ is proportional to the square root of time t.

Let us look at two lattice planes of a simple cubic crystal with the lattice constant a which contain the diffusing particles and are perpendicular to the x-direction considered (Figure 1.3). For simplicity the diffusion current j, only in the x-direction is considered. But in the real three-dimensional crystal lattice, for each jumping, the possibility for each direction ($+x$, $-x$, $+y$, $-y$, $+z$, or $-z$) should be equal.

According to Fick's first law, j_x can be expressed by

$$j_x = -\frac{a^2 \times r}{6} \times \frac{dc(x)}{dx} \equiv -D \times \frac{dc(x)}{dx} \tag{1.7}$$

where the constant of proportionality D is called the diffusion coefficient or diffusivity in units of m^2s^{-1}. This equation shows that the rate of transport is governed by the diffusion coefficient and the concentration gradient. It applies to steady state flux in a uniform concentration gradient. Therefore, equation (1.6) for the mean diffusion distance can be expressed in terms of the diffusion coefficient D:

$$\bar{x} = \sqrt{6Dt} \tag{1.8}$$

$$\bar{x} = \sqrt{4Dt} \tag{1.9}$$

$$\bar{x} = \sqrt{2Dt} \tag{1.10}$$

Equations (1.8), (1.9) and (1.10) show the relationship between the mean diffusion distance and the diffusion coefficient *D* in three, two and one-dimensional lattice, respectively.

1.4 Motivation

As mentioned above, irradiation, especially when combined with high-temperature annealing, can have beneficial effects on nanostructural materials, which has been demonstrated by the irradiation-mediated engineering, self-assembly and self-organization in carbon nanostructures [17–21]. All of these phenomena are results of a balance between creation, migration and annealing of point defects (interstitials and vacancies) during irradiation. Therefore, detailed knowledge of migration and annihilation of defects in nanostructured carbon materials is indispensable. A lot of theoretical work has been done already [42–46]; however, the quantitative information on diffusion of point defects has never been given by experiments due to the resolution limit of the instruments. Moreover, recent theoretical results [47, 48] are not in accordance with the old experimental data on migration energies of point defects obtained from planar graphite [15]. It shows that the curvature of the graphite network in nanostructures leads to a completely different migration of defects in carbon nanostructures than in graphite.

In this work, the diffusion of point defects induced by electron irradiation in carbon nanostructures, including zero-dimensional carbon onions, one-dimensional carbon nanotubes and two-dimensional graphene layers, were investigated quantitatively by *in-situ* TEM.

1. In Chapter 2 carbon nanostructures and the irradiation effects on them are treated in detail.

2. Chapter 3 focuses on the principles and instrumentations of the experimental setups, including the arc-discharge technique for the synthesis of carbon nanotubes and onions, the basic theory and experimental techniques of *in-situ* TEM, and ultrahigh vacuum furnace for annealing.

3. Chapter 4 describes the investigation of the migration of carbon atoms in carbon onions by the study of the influence of the high-temperature (1200~2000^{o}C) annealing effects.

Carbon onions made by arc-discharge technique can be in a state of heavy self-compression when irradiated with an electron beam. Annealing at high temperatures can relax the pressure in the centre of the onions by exchange of atoms between the shells, which make it possible to determine the activation energy for atom migration between graphitic layers.

4. Chapter 5 describes the investigation of the migrations of the interstitial carbon atoms inside one-dimensional SWCNTs by cutting the bundles repeatedly with a focused electron beam at different temperatures.

The mobility of interstitial carbon atoms in SWCNTs is determined by the combination of electron irradiation experiments in TEM with kinetic Monte Carlo simulations. The irradiation dose which is necessary to cut nanotubes with a focused electron beam is measured repeatedly as a function of separation between the cuts at different temperatures. As the cutting speed is related to the migration of displaced carbon atoms trapped inside the tube and their recombination with vacancies in the gap, information about the mobility of interstitial carbon atoms is getting available.

5. Chapter 6 describes the study of migration of individual metal (Au and Pt) atoms or clusters in graphene layers (two-dimensional diffusion) and carbon nanotubes (one-dimensional diffusion).

Individual Au and Pt atoms in layers of one or two graphene planes and carbon nanotubes are monitored in real time at high temperature by high-resolution TEM. The direct observation of the behavior of Au and Pt atoms in graphenic structures allows us to determine the position of the atoms and their diffusivities.

6. In Chapter 7 the conclusions drawn from the present work are summarized.

Chapter 2 Carbon Nanostructures

In this chapter, the carbon nanostructures, including two-dimensional graphene, one-dimensional carbon nanotubes, and zero-dimensional carbon onions are introduced. Afterwards, irradiation effects in carbon nanostructures are introduced in detail.

2.1 The Structures

2.1.1 Diamond and Graphite

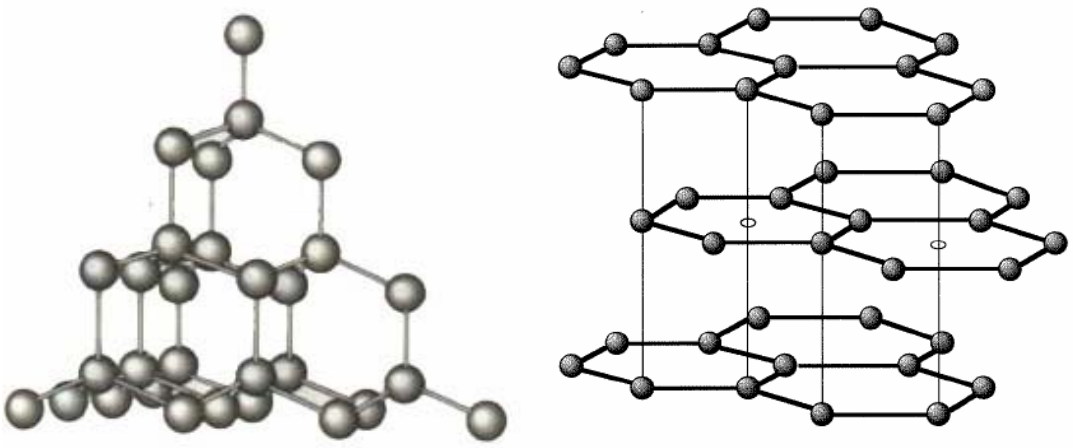

(a) **(b)**

Figure 2.1: The structures of diamond (a) and graphite (b).

It was generally assumed that the natural allotropes diamond and graphite are the only two carbon crystalline structures until the discovery of C_{60} [1]. At extremely high pressures carbon occurs in the form of diamond with a three-dimensional tetrahedral crystalline structure, in which each carbon atom is covalently bonded to four others (in Figure 2.1 (a)). All of the bonds have the same length of 0.154nm.

At ambient pressure graphite with a planar structure (shown in Figure 2.1(b)) is the

stable modification of carbon. Within the layer, each carbon atom is covalently bonded to three others in a planar pattern composed of hexagonal rings. These covalent bonds in the plane have the same length of 0.142nm, shorter than those in diamond. A two-dimensional stack is formed, and the flat sheets are loosely bonded with each other by weak Van der Waals force with the inter-layer distance of 0.335nm.

A free carbon atom has the electronic structure $(1s)^2(2s)^2(2p)^2$. In order to form covalent bonds one of the 2s electrons is promoted to 2p, and the orbitals are then hybridized with two possibilities. In diamond, one s-orbital and three p-orbitals undergo a sp^3 hybridization with a tetrahedral symmetry. However, in graphite one s-orbital and two p-orbitals undergo a sp^2 hybridization with a trigonal planar geometry. The nature of these different bonds leads to the variety of physical and chemical properties of the carbon allotropes.

2.1.2 Two-Dimensional Graphene

Graphite can be split into monoatomic layers by mechanical exfoliation or chemical intercalation. This kind of flat single layer of carbon atoms tightly packed into a two-dimensional structure composed of six-membered rings is called graphene (top in Figure 2.2). It provides a possible platform for integrated electronics and more importantly it is the basic building block for graphitic materials with all other dimensionalities. It can be wrapped up into zero-dimensional fullerenes, rolled into one-dimensional nanotubes and stacked into three-dimensional graphite, as shown in Figure 2.2 [49].

Figure 2.3 (a) shows a monolayer of graphene observed in TEM at 700°C. The layer is rolled slightly at the end (top) due to its instability under irradiation with electrons in TEM. A monoatomic layer is determined because of the absence of graphitic fringes with inter-distance of 0.335nm compared with the four-layered graphene sheet as shown in Figure 2.3 (b).

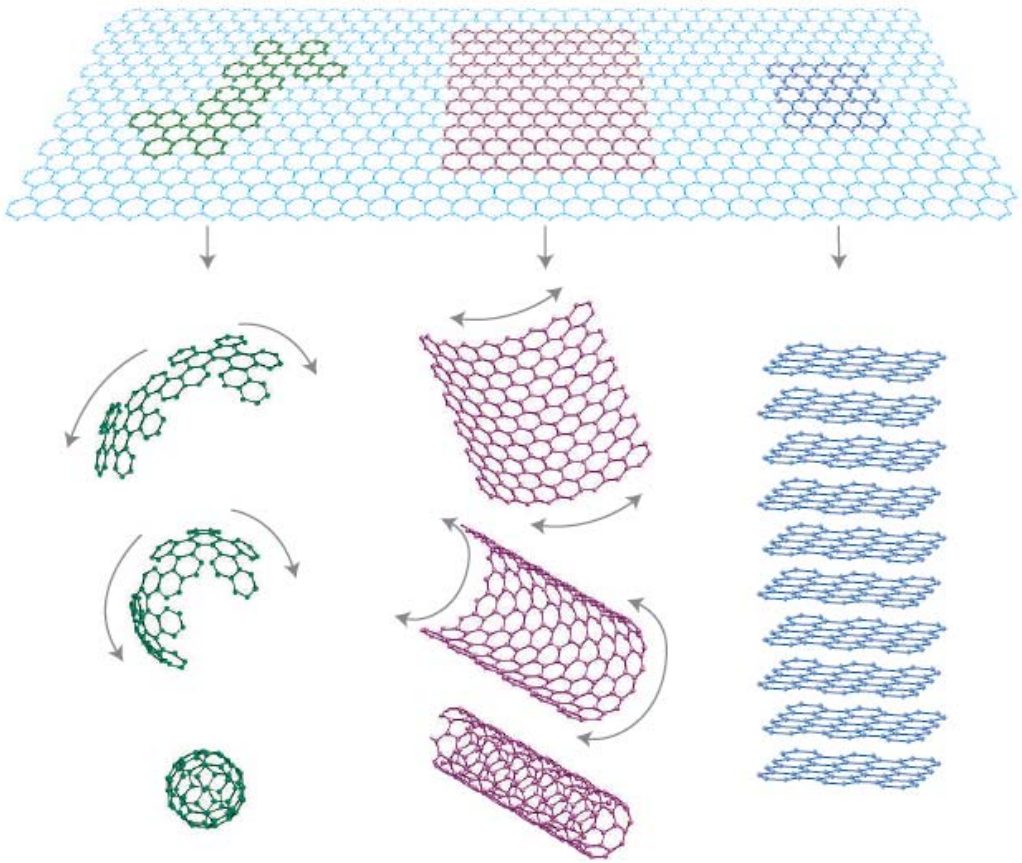

Figure 2.2: Graphene is a two-dimensional building block for graphitic materials of all other dimensionalities. It can be wrapped up into zero-dimensional buckyballs, rolled into one-dimensional nanotubes or stacked into three-dimensional graphite [49].

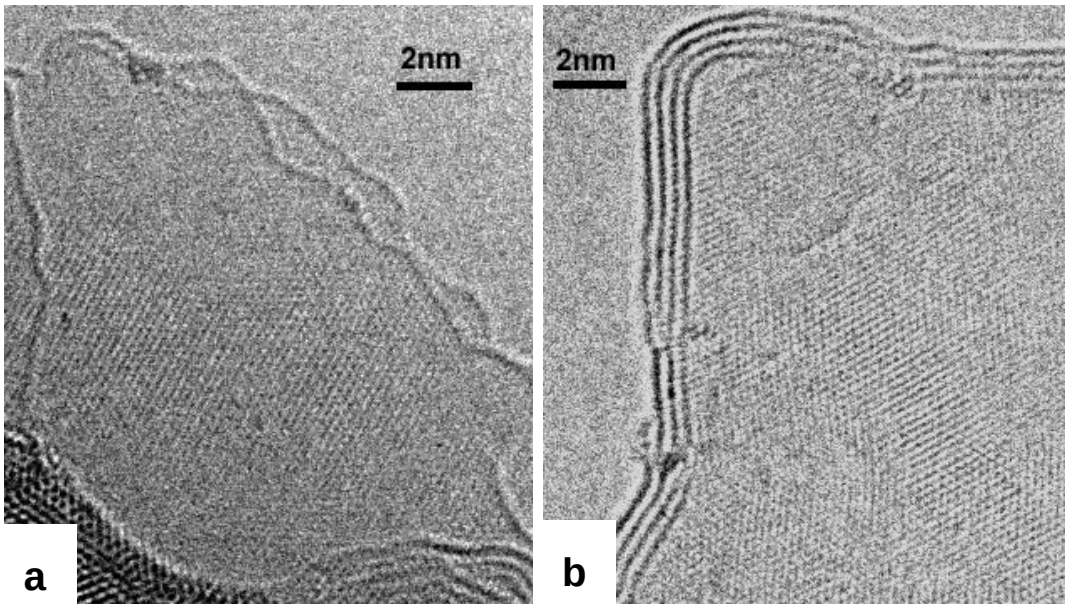

Figure 2.3: TEM images of a mono-(a) and a four-(b) layer of graphene at 700°C.

2.1.3 Zero-Dimensional Carbon Nanoparticles

2.1.3.1 Fullerenes

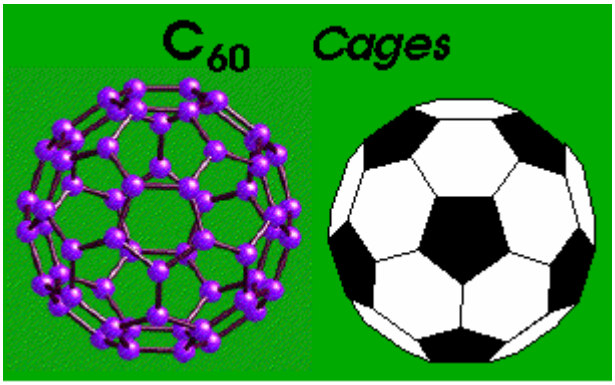

Figure 2.4: Structure of C_{60}.

Fullerenes (C_{60}) were discovered by Kroto and Smalley in 1985 with a laser vaporization technique and are composed entirely of carbon atoms [1]. Their spherical structure can be considered as the wrapping up of graphene but with the presence of non-hexagonal rings. C_{60} which has a similar shape as a soccer ball consists of twenty hexagons and twelve pentagons (shown in Figure 2.4). Each carbon atom is bonded to three others, so essentially the bonding is sp^2, although there is a certain degree of sp^3 hybridizations due to the curvature of the graphene sheet. This unique structure has shown unique physical and chemical properties [50].

2.1.3.2 Carbon Onions

In 1992, Ugarte found almost perfect spheres made up of concentric fullerenes during the irradiation of carbon nanoparticles with an intense electron beam, and described this kind of fullerene-like structures as “carbon onions” [7] (in Figure 2.5). Now it is well known that almost any form of carbon [51, 52], even diamond [53], will evolve into onions when irradiated with a sufficiently intense electron beam in an electron microscope, which means onions are the only stable form of carbon under the conditions of intense electron irradiation. When onions are fully developed, their

structure is perfectly spherical, and almost no lattice defects are visible. In the relaxed state, the distance between successive shells is about 0.34 nm, close to that in graphite.

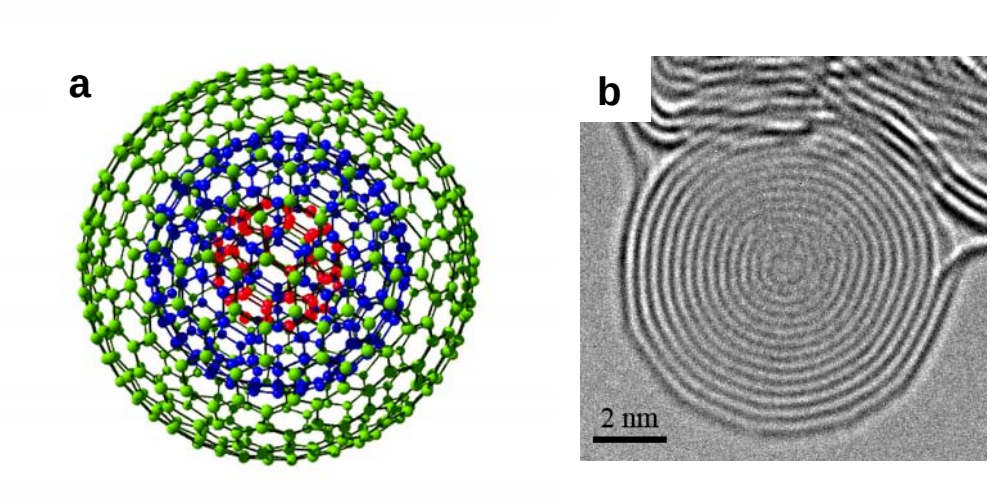

Figure 2.5: Structure of onion (a) and a TEM image (b).

For the detailed atomic structure model of carbon onions it was assumed by Kroto that the particle consists of nested fullerenes [54]. A plausible model assumes concentric 'magic number' (or Goldberg Type I) fullerenes. These fullerenes have N carbon atoms, where $N = 60\ b^2$, so that the first five are C_{60}, C_{240}, C_{540}, C_{960} and C_{1500} (with all fullerenes having the I_h symmetry) [55].

2.1.4 One-Dimensional Carbon Nanotubes

Carbon nanotubes were described by Iijima who applied the arc-discharge method in 1991 [6] as seamless cylinders of rolled graphene layers whose aspect ratio (diameter vs. length) is so high that it can be considered as a one-dimensional structure. They are classified as SWCNT and MWCNT, as shown in Figure 2.6. A MWCNT consists of several concentric SWCNTs with the interlayer distance of 0.335nm corresponding to the interlayer {0002} distance in graphite. Figure 2.7 shows TEM images of a SWCNT (a) and a MWCNT (b). The bonding in carbon nanotubes is primarily sp^2.

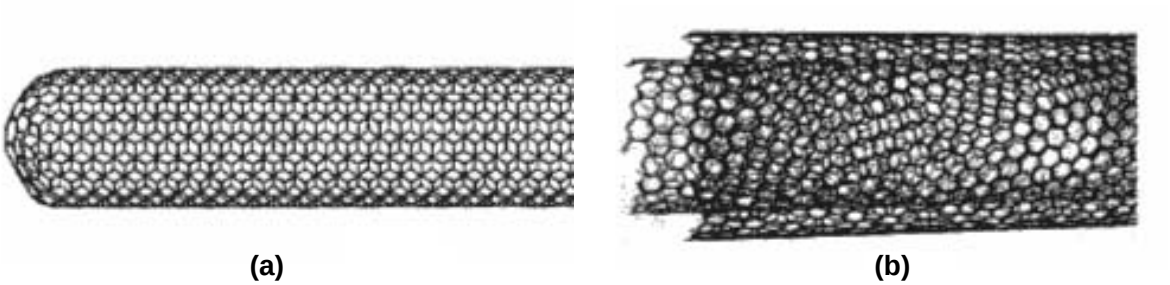

Figure 2.6: Structures of a SWCNT (a) and a MWNT (b).

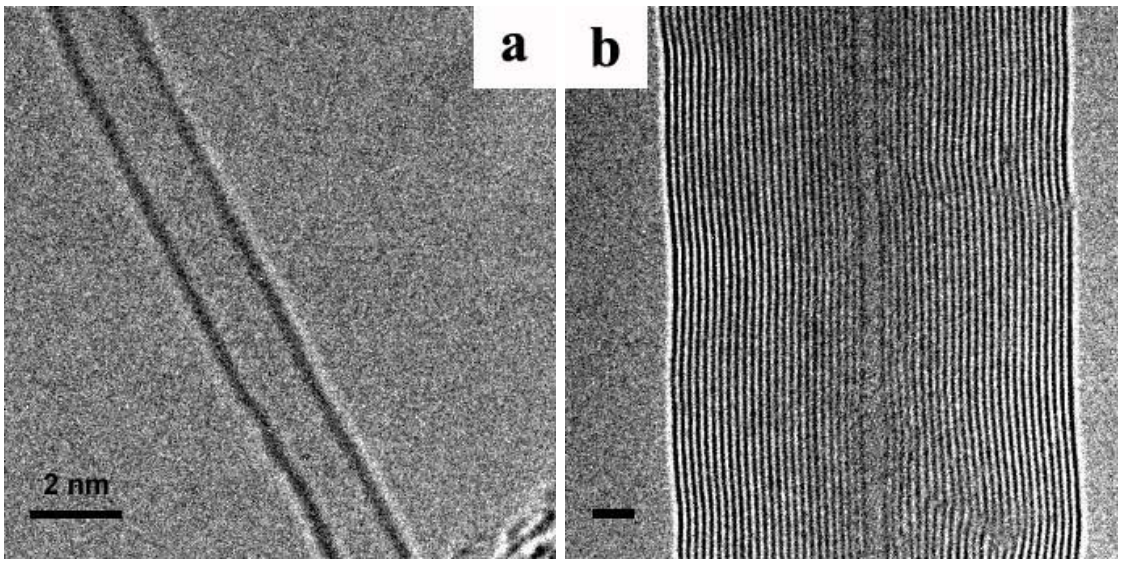

Figure 2.7: TEM images of SWCNT (a) and MWCNT (b) at 600°C. The scale bar is 2nm.

Carbon nanotubes have many novel mechanical, electronic, magnetic and optical properties that make them potentially useful in many applications [8, 9, 56, 57]. For example, a SWCNT is unique among solid state materials because every atom is on the surface. The properties of carbon nanotubes depend on their atomic arrangement (how the graphite sheets are 'rolled') and the diameter of the tubes [50, 56, 58–61]. The atomic structure of nanotubes can be described in terms of the tube chirality, or helicity, which is defined by the chiral vector $\vec{C}_h$ and the chiral angle θ.

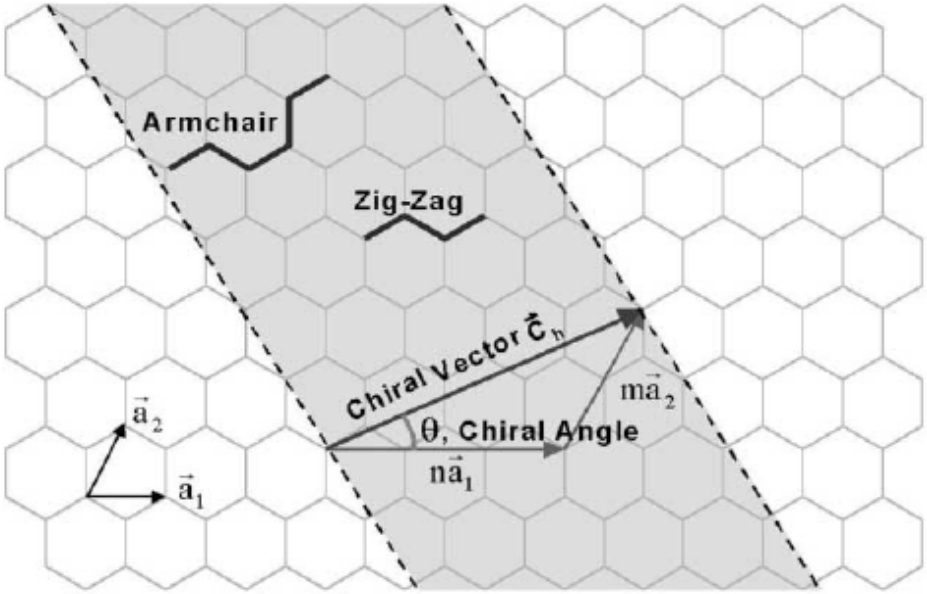

Figure 2.8: Schematic diagram showing how a hexagonal graphite sheet is 'rolled' into a carbon nanotube [56].

It can be visualized by cutting the graphite sheet along the dotted lines and rolling the tube so that the tip of the chiral vector touches its tail, as shown in Figure 2.8. The chiral vector $\vec{C}_h$ can be expressed as:

$$\vec{C}_h = n\vec{a}_1 + m\vec{a}_2 \tag{2.1}$$

where $\vec{a}_1$ and $\vec{a}_2$ are the unit cell base vectors of the graphite sheet, and the integers (n,m) are the numbers of steps along the zig-zag carbon bonds of the hexagonal lattice, shown in Figure 2.8. Each pair of integers (n,m) represents a possible tube structure.

There are two possible symmetries of nanotubes, known as armchair ($\theta = 30°$) and zig-zag ($\theta = 0°$). Figure 2.9 shows, from the viewpoint of the chiral vector $\vec{C}_h$, m = n for all the armchair nanotubes, and m = 0 for all the zig-zag nanotubes. All other nanotubes are chiral ($m \neq n$).

The chirality of the carbon nanotube has significant implications on its properties, especially on the electronic properties. For example, carbon nanotubes can be either metallic or semiconducting, depending on their chirality, although graphite is considered as a semi-metal [50, 56].

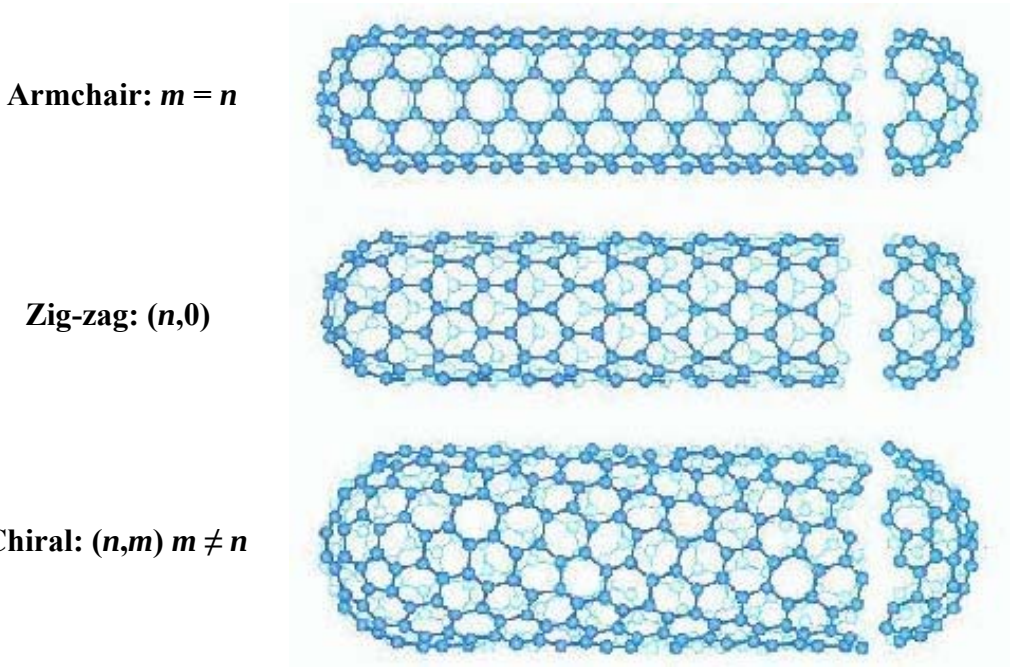

Figure 2.9: Illustrations of the atomic structure of an armchair, a zig-zag, and a chiral nanotube.

2.2 Irradiation Effects in Carbon Nanostructures

2.2.1 Graphite

Most carbon nanostructures are based on graphite, so irradiation defects in graphite are treated in detail in this part. Irradiation studies by using different particles (neutrons, protons, ions, electrons) have been done for a long time [16]. Here only the irradiation with electrons will be treated due to its importance in TEM studies.

As mentioned in Chapter 1, under irradiation graphite behaves like a metal because of its metallic character, although only in two dimensions. Excitation effects are not important, because ionization and electronic excitations are rapidly quenched by conduction electrons. Knock-on atom displacements govern the behavior of graphite and graphitic nanostructures under irradiation.

It is well known that the displacement threshold energy depends on the direction of the electron beam relative to the crystal lattice. Furthermore, previous work also

demonstrated that atoms are displaced rather into the open channels between the basal planes than within the basal planes in graphite.

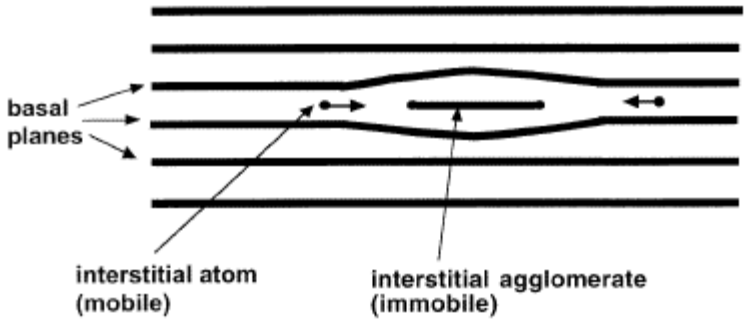

Figure 2.10: Schematic drawing of the aggregation of self-interstitials which are mobile in the open space between the basal planes of graphite. A dislocation loop develops between two basal planes [17].

Figure 2.10 schematically shows the rupture of basal planes due to the ejection of atoms out from the planes and the aggregation of interstitials into small dislocation loops between the basal planes. These are the essential types of irradiation damage in graphite at low temperatures below 200°C, where the mobility of vacancies and interstitials is low.

The formation, aggregation and annealing of defects are determined by the defect formation energy (E_f) and migration energy (E_m) which are listed in Table 2.1 for graphite. It shows that the formation energies of both vacancies and interstitials are much higher than migration energies. Both vacancies and interstitials would rather migrate within basal planes than between them.

A graphene sheet has a unique ability to reconstruct after the generation of vacancies. In Table 2.1, the formation energy of a divacancy is 8.7 eV by simulation [63], which is quite close to that of a monovacancy (7.3 [62]–7.5 [47, 63]). Furthermore, the migration energy of a monovacancy in the *ab*-plane is rather low [62–64] whereas divacancies are almost immobile due to their high migration energy of 7 eV [63]. Therefore, monovacancies can migrate and tend to coalesce to form stable and

immobile divacancies.

Table 2.1: The defects formation energy E_f and migration energy E_m for some point defects in graphite. (*a*-*b* means in *ab* plane and *c* means parallel to *c*-axis.)

defects	E_f **(theory)**	E_m **(theory)**	E_m **(exp.)**
monovacancy	7.3 [62]–7.5 [47, 63]		
a-*b*		1.0 [62]–1.6 [63, 64]	3.1 [15]
c		4.7 [62]	large
divacancy (*a*-*b*)	8.7 [63]	7 [63]	
adatom	6.4 [47]	0.4 [65]	
interstitial	6.8 [47]		
a-*b*		1.5 [47]	0.1 [15]
c		2.3 [62]	>5 [15]

Figure 2.11 shows that a monovacancy in a curved graphenic sheet cannot reconstruct because there is always one open bond left no matter how the new bonds form. However, divacancies can reconstruct without any dangling bonds. Hexagonal rings change to pentagonal rings, even heptagonal or octagonal rings may occur in more complicated cases. Such a reconstruction always leads to a local change of curvature because the hexagonal lattice is flat while pentagons or heptagons lead to a positive or negative curvature, respectively. Additionally, the surface area of the graphene sheet becomes smaller due to the removal of atoms and reconstruction. As a result, carbon nanotubes or onions, cylindrically or spherically closed graphite structures, shrink due to the loss of atoms but remain coherent due to their ability to close divacancies.

Of course, this reconstruction can only happen when each mononvacancy is mobile enough to coalesce with another one. Therefore, the specimen has to be heated to a temperature high enough for allowing the reconstruction. At low temperatures monovacancies would be stationary until their concentration is so high that the lattice

loses its coherence. This critical temperature may depend on the rate of defect production, and it was in the range of 200 – 300°C in irradiation studies in the TEM [66–68]. So in this work, all specimens were heated above this temperature range to be sure that no artefacts due to agglomeration of defects occur, even when only inspection of the material is desired and no deliberate irradiation is planned.

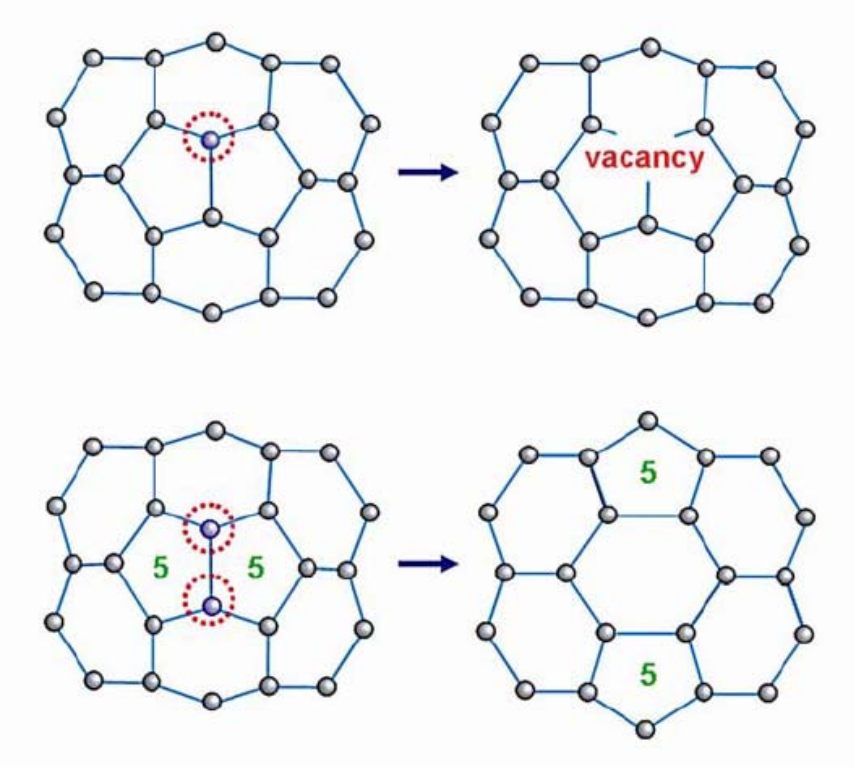

Figure 2.11: The removal of one atom from a graphene layer leaves a monovacancy (top). When two adjacent atoms are removed (bottom), the divacancy can close by reconstruction of the bonds. The number of hexagons decreases by one. For simplicity of the reconstruction of a structure with pre-existing pentagons was chosen [21].

The next section will focus on the carbon nanostructures which are different from crystalline graphite. As mentioned above, there is an anisotropy for the displacements of the atoms in graphite. However, this anisotropy can be neglected in most TEM studies of graphitic nanostructures due to two reasons: one is that the structures are curved so that all possible directions of incidence prevail, the other is that the energy of the

electrons in an electron microscope is much higher than the displacement threshold so that large angle scatterings dominate and knocks in different directions occur.

2.2.2 Carbon Nanotubes

Carbon nanotubes are made up of cylindrically curved graphene layers, consisting of a net of hexagons. SWCNTs or MWCNTs can change their structures and collapse under electron irradiation, which has been observed in early TEM studies [69, 70]. The use of heating stages makes controllable structural modification possible [33].

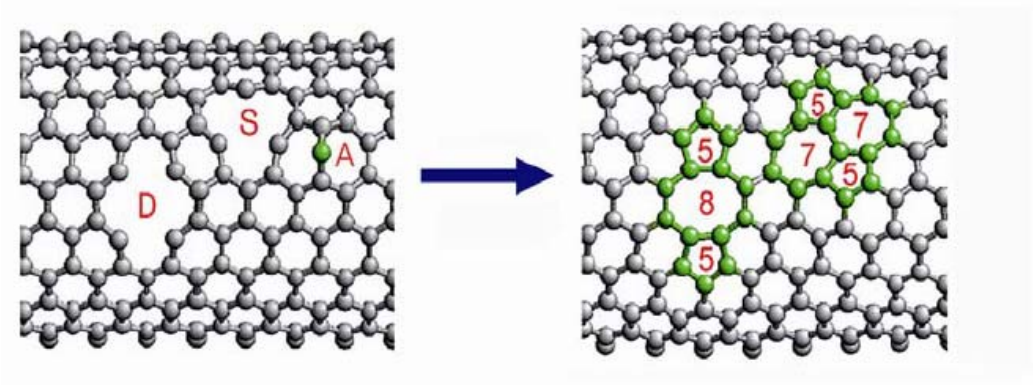

Figure 2.12: Model of a SWCNT with a single vacancy (S), a divacancy (D), and an interstitial as adatom (A). Reconstruction of the lattice obtained by computer simulation leads to the formation of 5-, 7-, and 8-membered rings. The decreasing surface area causes shrinkage of the tube [71].

The number of basal layers is a characteristic feature of carbon nanostructures. In the single-layered structure, there is no van de Waals interaction, and a knocked atom would rather leave the object than displace another atom. This is the reason why SWCNTs are less stable than MWCNTs under the electron beam. Above 300°C SWCNTs shrink under electron irradiation due to the loss of atoms and self-reconstruct by the closure of divacancies. Therefore, the initially perfect cylindrical surface becomes wavy and the diameter of the tube decreases. Figure 2.12 shows a simulation of this process [71]: after the formation of interstitials and vacancies, reconstruction of

the lattice leads to the transformation of hexagons to pentagons, heptagons, or octagons. Therefore, the tube shrinks and the curvature of the graphene layer changes, but the lattice remains coherent. The shrinkage of the tube can give rise to an internal pressure up to 40 GPa so that metal crystals encapsulated in the tube are deformed [29, 72].

2.2.3 Carbon Onions

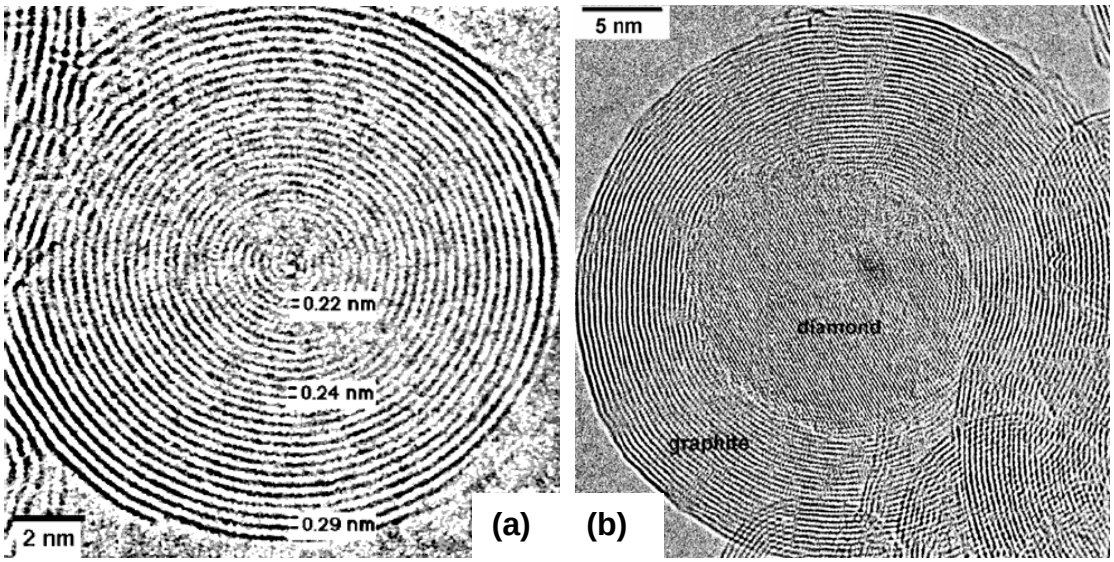

Figure 2.13: (a) The distance between the graphitic shells decreases towards the centre of the onion [67]. (b) The nucleation and growth of a diamond crystal in the centre of the onion [21].

Carbon onions consist of concentric fullerene-like spherical graphitic layers. Under an electron beam carbon onions can be set in a state of heavy self-compression above 500°C. The distance between the graphitic shells decreases towards the centre of the onion, which is smaller than that of the interlayer {0002} in graphite (0.335 nm), a decrease from 0.29 nm near the surface down to 0.22 nm in the centre has been observed [67, 73], as shown in Figure 2.13 (a). Continued irradiation of self-compressed carbon onions induces the nucleation of diamond crystals in the centre due to the extreme pressure, as shown in Figure 2.13 (b) [13]. Once nucleated, diamond crystals can grow under continuous electron irradiation until almost the whole graphitic onions

have transformed to diamond crystals [74]. Thus, the maximum size of the diamond is limited by the size of the onion.

Chapter 3 Experimental Methods

In the present study, the arc-discharge method was used to synthesize the specimens of MWCNTs, carbon onions and graphene layers. The specimens containing carbon nanostructures were prepared for electron microscopy by dispersing in ethanol, ultrasonicating and then depositing onto Cu, Mo or homemade graphite grids. Carbon nanostructures were observed and irradiated in the TEM from room temperature to 900°C. An high-vacuum furnace with a graphite crucible heated by an electron beam was used for *ex-situ* annealing studies.

In this chapter, the principles and instrumentations of these techniques are briefly described.

3.1 Specimen Preparation

3.1.1 Synthesis of Graphitic Nanostructures

Since the first synthesis of carbon nanotubes by the arc-discharge technique more than 15 years ago [6], several other techniques have been developed to form carbon nanotubes, including laser ablation [75–77], and chemical vapour deposition (CVD) from hydrocarbon using various metal particles as catalysts [78–80], etc. Each technique has advantages and disadvantages [8, 81]. The arc-discharge technique is a technique which has been widely used. Its disadvantages are that the production is a mixture of carbon nanotubes, polyhedral carbon nanoparticles and some amorphous carbon, and the yield is low (about 30% by weight). But the most prominent advantage of this technique is that the produced carbon nanotubes have the best quality owing to the high temperature during arc-discharge process. Laser ablation has a yield of 70% and can produce high-quality SWCNTs with a controllable diameter by controlling the reaction temperature. However, a large setup is necessary. Compared with the

arc-discharge and laser ablation techniques, CVD is an efficient technique for the synthesis of carbon nanotubes at low temperature and ambient pressure, however at the cost of structural perfection.

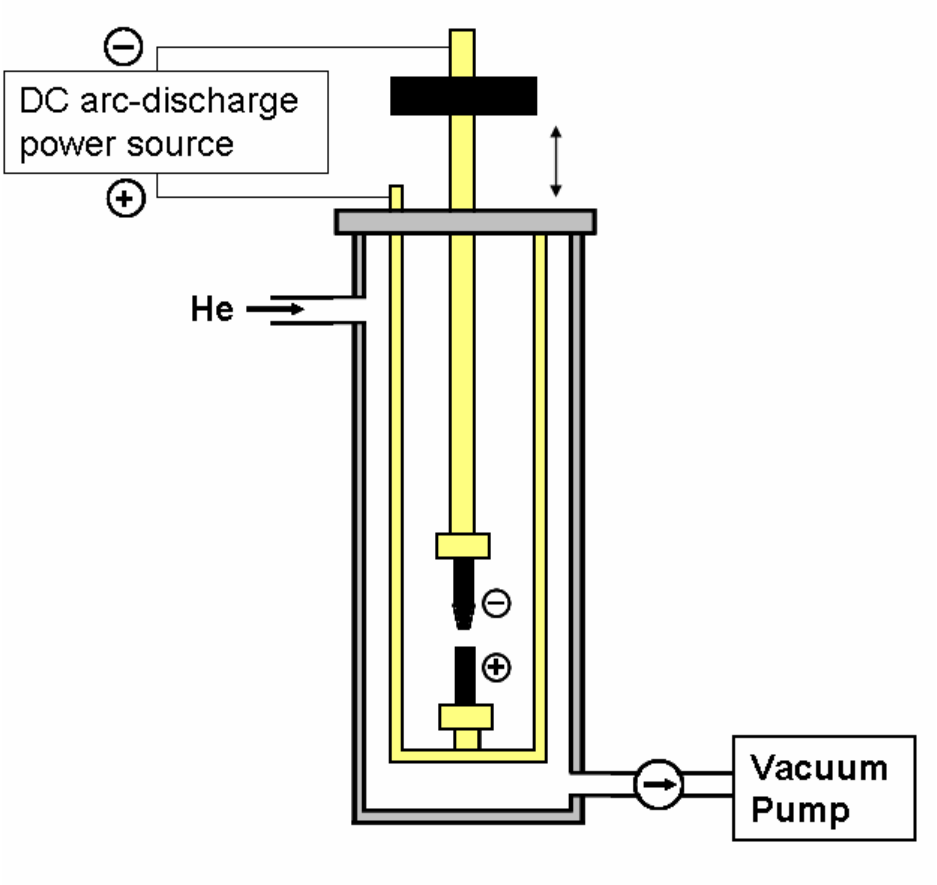

Figure 3.1: Schematic diagram of a carbon nanostructure formation apparatus by the arc-discharge method.

The arc-discharge technique was used in the present work to synthesize MWCNTs and carbon onions. Figure 3.1 shows the apparatus of arc-discharge schematically. Two graphite rods of high purity are used as the anode and cathode in the chamber, respectively. The position of the cathode is adjustable from the outside of the chamber. After evacuating the chamber with a vacuum pump, a continuous flow of helium is introduced to the desired pressure (about 300 Torr in the present study). When the pressure is stable, a DC voltage of 80V is applied between the two graphite rods. At the

beginning of the experiment the two electrodes are not in contact, so there is no current. Then the cathode is gradually moved towards to the anode until arcing occurs. When a stable arc is achieved, the gap between the rods is kept at about 1 mm or less. During the operation, a deposit grows on the cathode rod. After around 1minute the power is turned off and the chamber is cooled down before opening.

There are several important factors in producing a good yield of high quality nanotubes, such as the pressure of the helium [82–84], the current [83, 85, 86], and the cooling of the electrodes in the chamber [87]. When a graphite rod containing metal catalyst (Fe, Co, Ni, etc.) is used as the anode and a pure graphite rod is used as the cathode, SWCNTs can be produced instead of MWCNTs [88, 89].

3.1.2 Specimen Preparation for Transmission Electron Microscopy

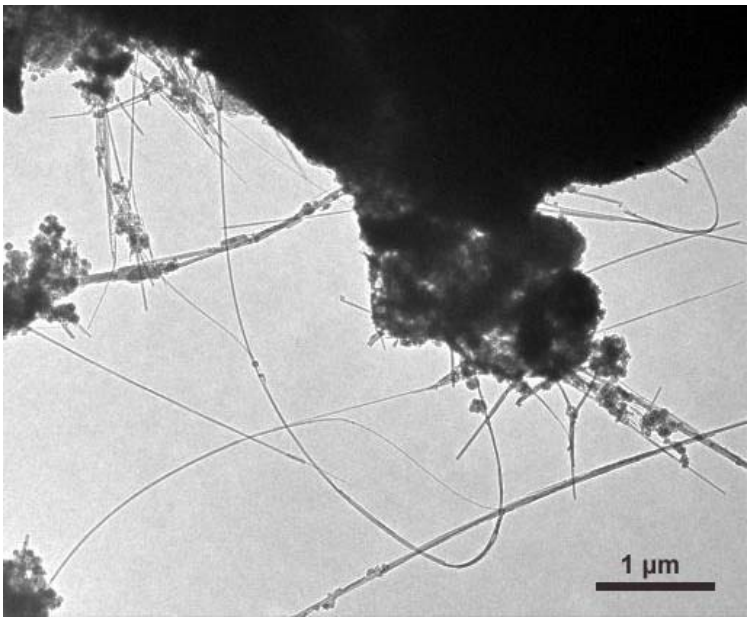

Figure 3.2: TEM image of core material from the deposit containing both carbon nanotubes and nanoparticles.

A typical deposit on the cathode rod consists of a hard gray outer shell and a soft fibrous black core. The fibrous core which contains a lot of MWCNTs and polyhedral nanoparticles was removed and dispersed in ethanol. After ultrasonication for a few minutes, the soot was deposited directly onto pure Cu, Mo, or homemade graphite grids for TEM studies. Figure 3.2 shows an image of the soot in the TEM.

In many studies, nanoparticles are deposited on a grid with an electron-transparent carbon film. However, in the present work pure metal grids without carbon film were used for two reasons: the image of the carbon film overlaps the images of the investigated objects; and the carbon films are not stable and tend towards wrapping or rolling at high temperatures and under irradiation. It is also important that in the desired temperature range, the metal grids are stable, do not evaporate or react with the carbon nanoparticles or material of the heating stage. Generally commercially available Cu grids are useful in the range of room temperature to 600°C, but above this temperature range Mo grids are needed. In this work some grids had to be heated up to 2000°C for annealing experiments, thus homemade pure graphite grids were used because molybdenum reacts with carbon above 1100°C. The graphite rods of high purity with the diameter of 3 mm were cut into many platelets. The platelets were rubbed and polished on sandpapers until they were thin enough to fit the holder of the TEM. A hole with a diameter of about 1 or 2 mm was made in the center of a graphite platelet and there were many soot particles attached on the edge of the hole after deposition. Some marks were made by a needle on the platelets in order to find the position when the platelets were put on the stage of the TEM before and after *ex-situ* annealing.

3.2 Transmission Electron Microscopy (TEM)

3.2.1 Basic Setup of TEM

As mentioned in Chapter 1, TEM is the most powerful tool for the investigation of nanostructures due to its high spatial resolution. It works with an electron source instead

of light in a normal light microscope whose resolution is limited by the wavelength of light. The electrons coming from the source are accelerated by an electric field and focused by electromagnetic lenses onto the specimen. The electrons interact in different mechanisms with the specimen (shown in Figure 3.3), and most of these signals which give us chemical information and a lot of other details about the specimen can be detected by different accessories in TEM, for example energy-dispersive X-ray analyzer (EDX) and electron energy-loss spectrometer (EELS). Firstly and most importantly, elastically scattered electrons which go through the specimen (red arrow in Figure 3.3) were used to form an image of the specimen in TEM.

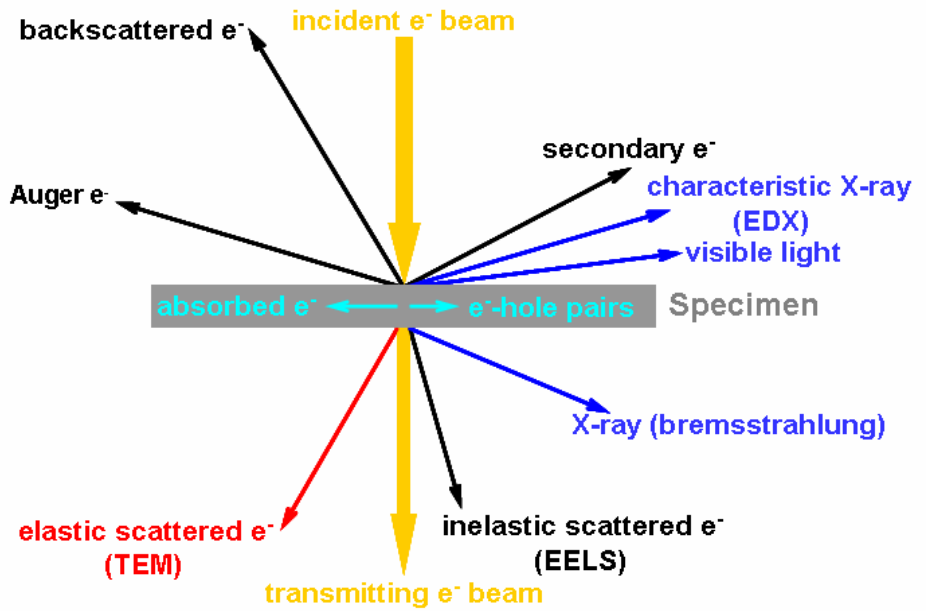

Figure 3.3: Signals generated when a high-energy electron beam interacts with a thin specimen. The directions shown for each signal do not always represent the physical directions of the signal but indicate, in a relative manner, where the signal is strong or where it is detected.

A more detailed explanation of a TEM is as follows (in Figure 3.4 (a)):

1. Electrons are generated by the electron gun at the top either by thermionic emission or by field emission. Thermionic sources are either tungsten filaments or lanthanum hexaboride (LaB_6) crystals, whereas the field-emission source is a fine tungsten needle. In the present work, all specimens were observed in TEM (FEI Tecnai F-30)

(shown in Figure 3.4 (b)) with a Schottky field-emission source and an acceleration voltage of 300 keV. A higher resolution can be achieved with higher energy of the electrons. However, more damages of the specimen may occur.

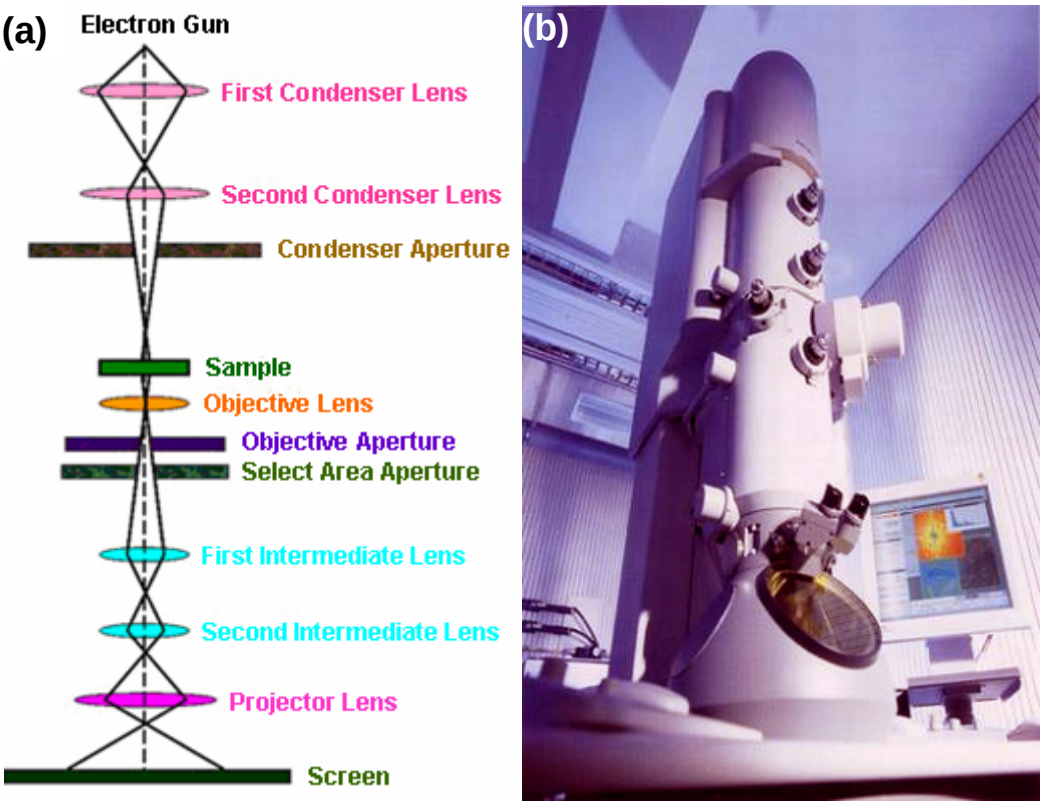

Figure 3.4: Schematic drawing of the ray diagram in a TEM (a) and the microscope used in this work (FEI Tecnai F-30) (b).

2. The electrons are focused to a small and coherent beam by the use of the first and the second condenser lens. With the first lens the “spot size” can be adjusted, whereas the second lens is used to focus the beam onto the specimen and control the illuminated area.
3. The beam is restricted by the condenser aperture which blocks the high-angle electrons far from the optical axis.
4. The electrons are transmitted through the specimen.
5. The transmitted electrons are focused by the objective lens on the focal or image plane.

6. The objective aperture is used to determine the contrast by transmitting or blocking diffracted electrons. The selected area aperture is used in the diffraction mode to obtain a diffraction pattern from a selected area within the illuminated specimen.
7. The image is magnified by the intermediate and projector lenses.
8. The image strikes the image screen and light is generated to make the image visible by eyes. With the development of computer technology, charge-coupled device (CCD) cameras became available for on-line viewing and processing, particularly of high-resolution TEM images. Spectroscopy can be carried out by detecting the corresponding signals with special detectors. More details can be found in the TEM textbook written by D. B. Williams and C. B. Carter [90].

In the present study the electron dose in the TEM is a very important parameter. It is defined as the charge density hitting the specimen, and can be measured in units of e/nm^2s in the TEM.

3.2.2 Experimental Techniques of *In-Situ* TEM Study

The advantage of the study of defects by *in-situ* TEM is that the defects can be generated and their evolution can be recorded in real time at atomic resolution with the same electron beam. However, it is worthy to be noted that the electrons causing the structural alterations are not the same as the electrons for imaging in TEM. The former strike the specimen and lose energy, and cannot be used for imaging. Therefore, the optimum beam settings for both are often not achieved at the same time. It is clear that for high-resolution imaging the optimum is coherent illumination of the specimen with a parallel beam of moderate intensity. For irradiation the optimum beam setting depends on the problem to be studied. In most cases a beam current density higher than that for imaging is needed, which can be achieved by using the largest condenser aperture and the lowest excitation of the first condenser lens (large spot size). Of course this kind of settings cannot give a coherent illumination of the specimen. The highest possible beam current density of up to 4×10^5 A/cm^2 is achieved when the beam is fully focused onto a

spot with a diameter of less than 1 nm in the field emission TEMs with an aberration-corrected condenser system. However, in this case the illuminated specimen area is too small for imaging and a spreading of the beam is required to observe the result of irradiation. Images with lattice resolution are recorded with a CCD camera. In order to reduce noise and get higher signal-to-noise ratio, exposure times of typically 0.1–0.5 seconds were chosen than in real-time recording.

The temperature of the specimen is very important for the evolution of irradiation defects. Heating caused by the dissipation of phonons under electron irradiation is very low. Therefore, a special specimen stage is necessary to ensure that a desired temperature can be achieved, adjusted and measured. A Gatan Model 628 single tilt heating holder with a water cooling system in the rod of the holder and a Philips PW 6550 heating holder without a cooling system were used here, and maximum operating temperatures of 1300°C and 900°C were achieved, respectively.

3.3 Annealing of Graphitic Nanoparticles

In order to study the migration of carbon atoms in carbon onions, the specimens were annealed at temperatures up to 2000°C in a high-vacuum furnace where electron beam heating is applied, as shown in Figure 3.5.

The specimen was placed in a pure graphite container which is applied a positive potential (0–2000 V). Electrons are emitted from W wires on ground potential that were heated by a current of about 1.7 A. The electrons gain energy in the electric field between the W wires and the crucible and lose their energy by dissipation on the crucible. Thus the container for the specimen could be heated to a desired temperature by adjusting the high voltage or the heating current through the W wire. The temperature can be either calculated by applying Stefan-Boltzmann’s law or measured with a pyrometer through a view window.

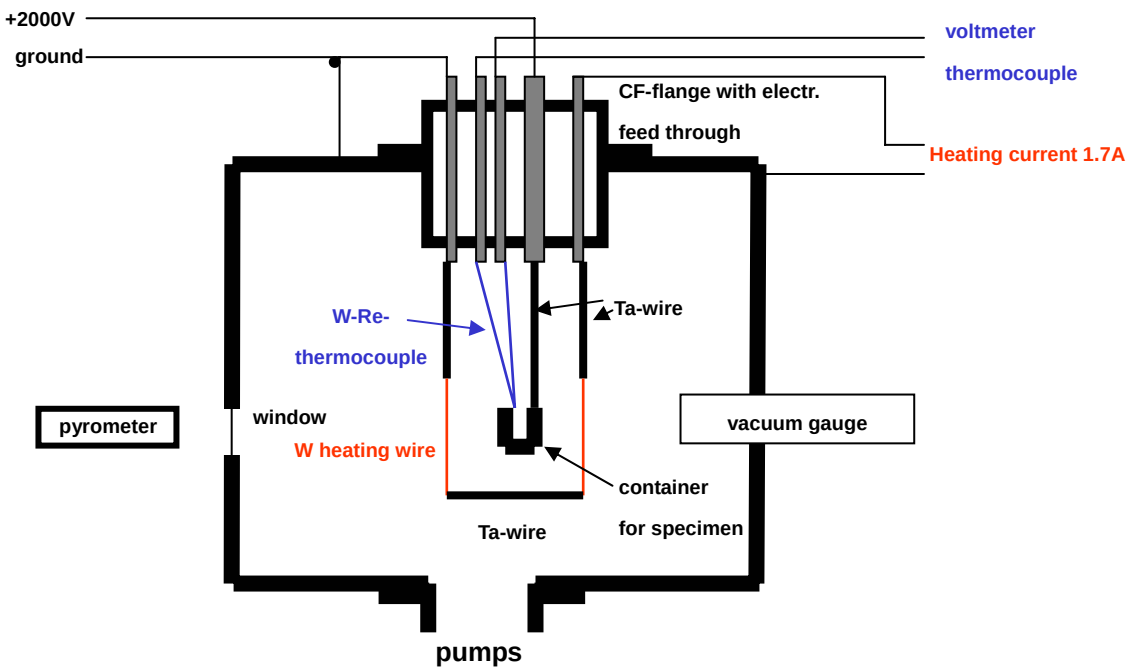

Figure 3.5: Schematic drawing of the high vacuum furnace heated by an electron beam.

The crucible can be considered as a black body which absorbs all thermal radiation incident on it. All black bodies heated to a given temperature emit thermal radiation. The heat emitted by a black body (per unit time) at an absolute temperature of T is given by Stefan-Boltzmann's Law:

$$Q = A\sigma T^4 \tag{3.1}$$

where Q is the heat transfer per unit time in units of Watts, A is the total radiating area of the black body in units of m^2, and $\boldsymbol{\sigma}$ is the Stefan-Boltzmann constant with a value of 5.7×10^{-8} W/m^2K^2.

However, a “grey” body is a more realistic case, and Stefan-Boltzmann's Law can be expressed as:

$$Q = \varepsilon A\sigma T^4 \tag{3.2}$$

where ε is the emissivity of a material, which is the ratio of the energy radiated by the material to that by an ideal black body at the same temperature.

In our furnace, a cylindrical graphite crucible with a diameter of 12 mm and a height of 10 mm was used to avoid possible contamination with metal. The total

radiating area A is about 6×10^{-4} m^2 and the emissivity of graphite is about 0.8. Therefore, a power of 1 kW is needed in order to reach 2000°C.

In the present annealing experiment the specimen was covered by another polished pure graphite platelet in the crucible to avoid the contamination from the evaporation of W wires. Before annealing the pressure in the furnace was about 10^{-6} Pa after pumping overnight and heating the recipient. Heating from room temperature to 2000°C took typically 45 seconds, cooling from 2000 to 1000°C took 15 seconds. The specimen was taken out from the furnace after cooling down to room temperature and then observed in the TEM.

Chapter 4 Diffusion of Carbon Atoms in Graphitic Structures and Stability of Carbon Onions

There are two diffusion mechanisms of carbon atoms in graphitic structures: migration within the graphitic layers and jump between the layers. The latter is more important and interesting because it has a considerable influence on the stability of the graphitic structures. Early studies [13, 67] have demonstrated that carbon onions made by arc-discharge technique can be in a state of heavy self-compression when irradiated with an electron beam. The present work shows that annealing above 1500°C can relax the pressure in the centre of the onions by an exchange of atoms between the shells. An activation energy of 5.0 eV is obtained from estimating the diffusivity of carbon atoms at different temperatures. Such a high activation energy not only prevents the exchange of carbon atoms between the layers at low temperatures but also ensures the high morphological and mechanical stability of graphite nanostructures. It is also shown that spherical carbon onions, even when they are in a self-compressed state, are surprisingly stable at temperatures up to 1200°C. In addition, the stability of carbon onions at 600°C under extremely intense electron irradiation was investigated and the results show that the smaller the onion is, the more stable it is under electron irradiation.

4.1 Introduction

The self-diffusion in macroscopic graphite crystals has already been a subject since the 1960s [15, 91, 92] in reactor technology, but unfortunately no reliable data have been obtained due to the lack of graphite single crystals with high perfection. However, with the renewed interest in graphitic structures after the discovery of carbon nanotubes, the diffusion of carbon or boron atoms in graphite has been subject of theoretical studies

[93–95], and the migration energy for atom jumps between the layers has been calculated. The migration of carbon atoms, including migration within the layers and jumps between the layers in the graphitic lattice, is important in the technology of carbon nanomaterials. As mentioned in Chapter 2, single vacancies in graphitic layers are mobile enough to lead to a reconstruction by coalescing with others *within* the layers above 200 – 300°C [46, 66–68]. However, an exchange of atoms *within* a shell can only lead to a reconstruction of the shell with minor change of its surface area [96–98]. It is the exchange of atoms *between* the shells that needs a higher activation energy and results in a considerable morphological alteration of the whole graphite particle. So the ability of carbon atoms to jump between the graphenic layers is particularly interesting. The thermally induced exchange of atoms between the layers not only leads to a relaxation of the particle towards an equilibrium structure but also determines its morphological or mechanical stability at high temperatures. Therefore, a microscopic measurement of the diffusivity of carbon atoms between the layers of graphitic structures is highly desirable. Some recent experiments have indicated that morphological changes induced by thermal relaxation do not occur much below 2000°C. For example, superplasticity [99] and dislocation climb [100] in carbon nanotubes, the collapse of nanotubes under heating [101], the thermal transformation of nanotube bundles [102], and the coalescence of nanotubes [103] have been observed at high temperatures.

The present study focuses on the mobility of carbon atoms normal to graphenic basal layers by observing the thermal relaxation of heavily compressed carbon nanostructures. Self-compression phenomena are observed both in carbon onions [13] and carbon nanotubes [29] when they are irradiated by electrons or ions at high temperatures. Under electron irradiation a MWCNT shrinks, which can give rise to an internal pressure of up to 40 GPa so that metal crystals encapsulated in it deform and may even break [29, 72]. Carbon onions are multi-shelled fullerenic clusters [7, 104] and may be considered as the spherical analogon to carbon nanotubes. Their perfectly spherical symmetry makes them an ideal system for studying the thermal relaxation of

the graphitic lattice. Under particle irradiation the distance between the compressed graphenic shells in carbon onions decreases towards the centre of the onion to smaller values than those of the interlayer {0002} in graphite (0.335 nm) and can reach values as low as 0.22 nm, which may eventually lead to the transformation of the graphitic core to diamond [13, 105]. The pressure in the centre of the compressed carbon onion is hydrostatic and may reach values even higher than those inside compressed carbon nanotubes. It is a remarkable fact that particles of a few nanometers in size are able to hold pressures of tens of GPa permanently (an order of 100 GPa might even be possible) just due to the high tensile stability of their shells. The complete relaxation towards an uncompressed state can only occur by an exchange of atoms between the graphenic layers in all directions due to their perfectly spherical symmetry. The self-compressed onions were generated by electron irradiation and observed at 600°C by TEM both before and after annealing at temperatures in the range of 1200–2000°C. The quantitative experimental information about the diffusion of carbon atoms normal to the graphenic layers was obtained by observing the relaxation of the onions towards an uncompressed state. The observations also shed light on the morphological stability of carbon nanoparticles at high temperatures. Furthermore, the stability of carbon onions was investigated by observing them under sustained electron irradiation with an extremely intense beam up to 1500 A/cm^2 at 600°C in the TEM.

4.2 Experimental

4.2.1 Annealing Experiments

Graphitic soot which contains MWCNTs and polyhedral nanoparticles formed on the cathode in the arc-discharge apparatus was used as the starting material for the experiments. The soot was dispersed in ethanol and ultrasonicated for a few minutes. It was then deposited on homemade pure graphite grids and dried in air.

Firstly, the pristine specimens were irradiated by electrons with an energy of 300

keV and an intensity of 500 A/cm^2 for approximately 10 minutes in the TEM where they were held at 600°C during both irradiation and inspection by a heating stage. The elevated specimen temperature in the TEM was chosen to prevent uncontrolled beam-induced defect formation in the graphitic material. Whereas the graphitic nanoparticles before irradiation were polyhedral and showed the usual spacing of 0.33 nm between the shells, the spherical onions after irradiation were in a compressed state where the interlayer spacing decreased from 0.31 nm near the surface down to 0.25 nm in the centre.

In order to study the stability of the compressed carbon onions under annealing, the homemade graphite grids were taken out from the TEM after the formation of some self-compressed onions and transferred to a graphite crucible in an ultrahigh-vacuum chamber. The crucible was heated by an electron beam (2 kV, 0.5–1 A) to temperatures in the range of 1200–2000°C. The temperature was measured by a pyrometer through a viewing window. The pressure in the chamber was about 2×10^{-6} Pa before annealing. The average heating rate from room temperature to 2000°C and cooling rate from 2000°C to 1000°C were about 44 and 67 °C/s, respectively. The specimens were then annealed for a certain time. After cooling down to room temperature, they were transferred back to the TEM and inspected again at a temperature of 600°C, but at low electron beam dose (15 A/cm^2 for a typical observation for less than one minute) to avoid the build-up of new pressure in the centre of carbon onions. By marking the graphite grids and taking series of images at high and low magnifications, the irradiated structures could be found again after the *ex-situ* annealing.

4.2.2 Irradiation Experiments

For studying the stability of carbon onions under extremely intense electron irradiation, graphitic soot made by arc-discharge technique was deposited on pure Cu grids. The specimens were exposed to electron irradiation with an intensity up to 1500 A/cm^2 in the TEM where they were held at a temperature of 600°C during irradiation

and inspection by using a heating stage. The morphological evolutions of the carbon nanoparticles were recorded.

4.3 Results and Discussions

4.3.1 Annealing Experiments

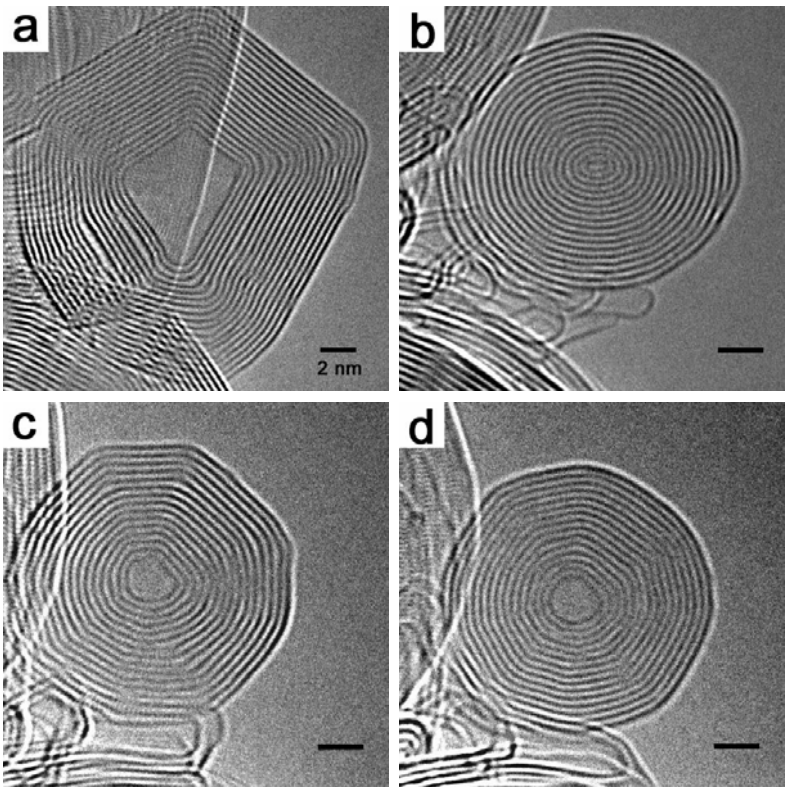

Figure 4.1: (a): a faceted carbon onion in the starting material before irradiation; (b): the same particle after intense electron irradiation; (c) and (d): after *ex-situ* annealing at 2000°C for 120 and 300 seconds, respectively. Whereas the shells in the centre in (b) are compressed (seen as a decreased spacing), the shells in (c) and (d) are relaxed.

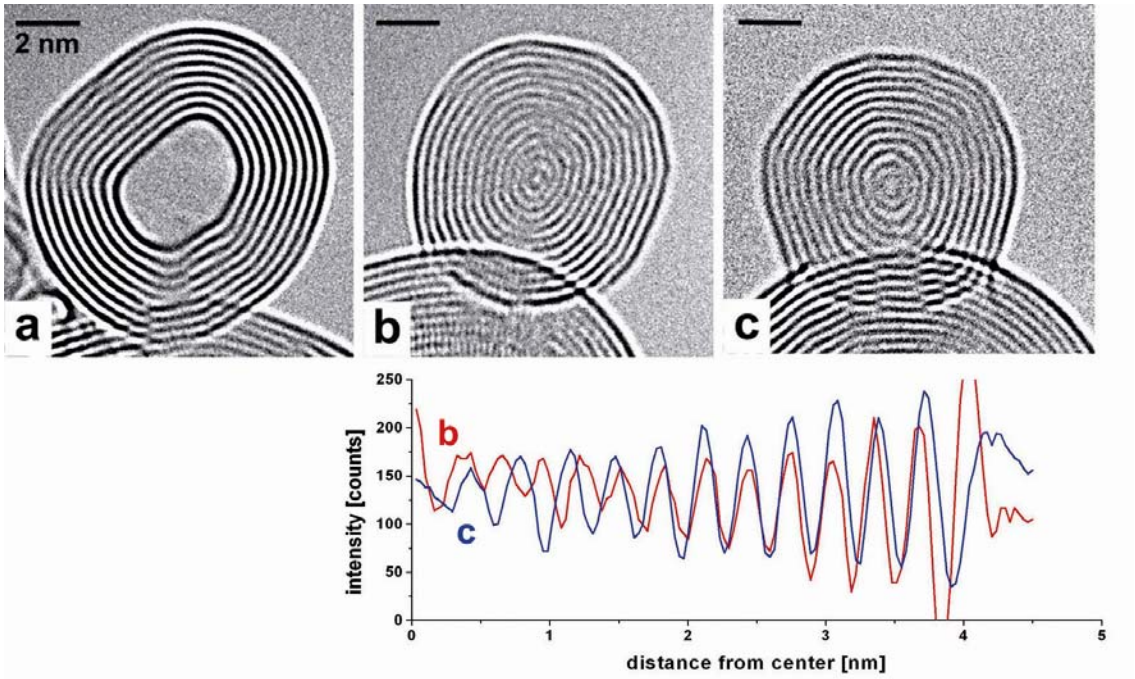

Figure 4.2: A small carbon onion (a): before irradiation; (b): after electron irradiation; (c): after annealing for 120 seconds at 2000°C. The relaxation upon annealing in (c) is visible as an increase of spacing between the shells. The plot shows an intensity profile through the onion from image (b) in red and (c) in blue. The profiles extend from the center (distance 0) to the surface (distance 4.3 nm). The profile of (b) has been stretched vertically to match the amplitude of (c).

The results of annealing at 2000°C of a large carbon onion and a small carbon onion are shown in Figures 4.1 and 4.2, respectively. The onions in the starting material before irradiation are shown in the respective figures (a). After electron irradiation they are transformed to a spherical compressed particle in (b), and the onions after *ex-situ* annealing at 2000°C for 120 seconds are shown in (c). The spacing between the layers in the starting material (figures (a)) is approximately 0.33 nm, as in bulk graphite. After irradiation (figures (b)), the onions are in a self-compressed state and the spacings between the shells range from 0.33 nm at the surfaces to 0.27 nm close to the centres. Generally, the distances between the shells in the centers of the larger onions are smaller than those in the centers of the smaller onions, indicating that larger onions have higher pressure in the centers due to the cumulative action of more shells. After annealing for approximately 120 seconds at 2000°C (figures (c)), the spacings between the shells

relax towards the initial value of 0.33 nm, even in the centres, so that a complete relaxation of compressive strain occurs. Further annealing at 2000°C for another 180 seconds (300 seconds totally) does not result in obvious morphological changes (Figure 4.1 (d)) which further demonstrates that the relaxation has finished completely in the first annealing step (120 seconds). The minor difference between Figure 4.1 (c) and (d) can be attributed to the electron irradiation during inspection in the TEM. Larger onions such as the one shown in Figure 4.1 develop an internal hollow during annealing and a tendency towards faceting of the surface. In some cases, annealing caused an internal hollow of up to 5 nm and a corresponding expansion of the onions. Due to the relaxation and expansion of the structures, the number of shells decreases during the annealing. For reasons of mass conservation, the number of shells decreases during expansion (18 layers in Figure 4.1 (b) and 15 layers in 4.1 (c); 13 layers in Figure 4.2 (b) and 12 layers in 4.2 (c)). An intensity profile through the images of the onion is shown in Figure 4.2. Maxima correspond to bright and mininma to dark fringes. The increase in spacing between the shells during relaxation is seen as the increase in “wavelength” from (b) to (c).These observations were reproduced for many other onions.

Figure 4.3 shows the results of annealing at 1500°C for 120 and 420 seconds. Figure 4.3 (a) and (b) shows that the onion is in the relaxed and self-compressed state before and after irradiation in the TEM before annealing, respectively. The spacings between the shells decreased from 0.33 nm (Figure 4.3 (a)) to 0.33 nm at the surface and 0.30 nm in the centre (Figure 4.3 (b)). After annealing at 1500°C for approximately 120 seconds (Figure 4.3 (c)), the onion is still in a self-compressed state and the spacings between the shells range from 0.33 nm at the surface to 0.31 nm in the centre, larger than those before annealing (Figure 4.3 (b)). The compression decreased, but did not vanish. After annealing at 1500°C for another 300 seconds (Figure 4.3 (d)), the spacing between the shells relaxes completely towards the initial value of 0.33 nm as shown in Figure 4.3 (a). However, a considerable expansion of the onions did not occur. In the whole process, the number of shells decreased from 22 before annealing to 20 after annealing for 120 seconds and finally to 19 after annealing for 420 seconds.

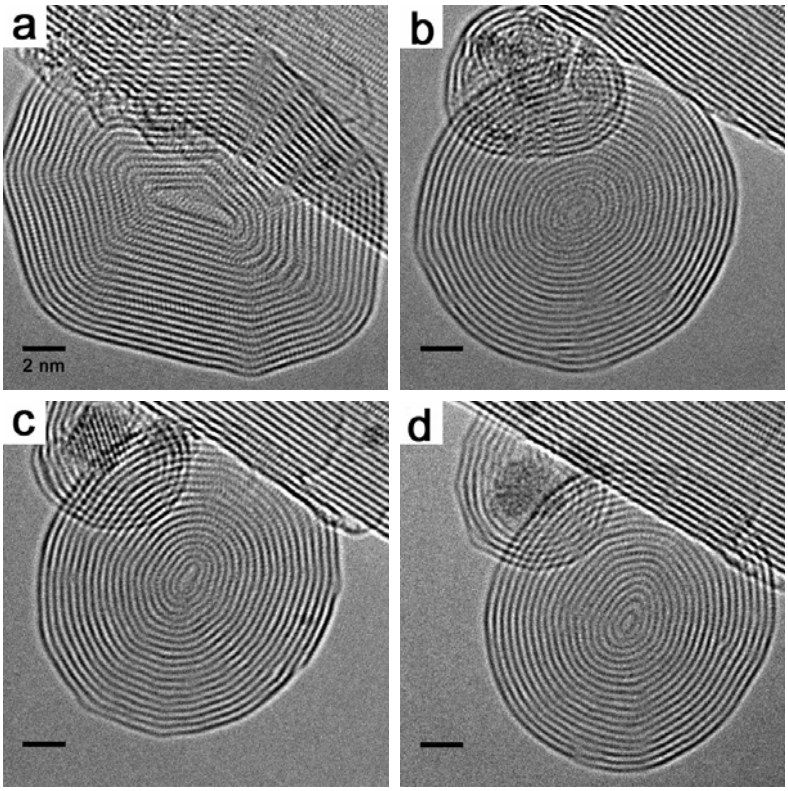

Figure 4.3: Annealing of a carbon onion at 1500°C. (a): before irradiation; (b): after electron irradiation; (c) and (d): after annealing at 1500°C for 120 and 420 seconds, respectively. Whereas the shells in the centre in (b) are compressed (seen as a decreased spacing), the shells are relaxed partly in (c) and completely in (d).

The results of annealing at 1200°C are shown in Figure 4.4. Before and after annealing at 1200°C the spacings between the shells remain 0.33 nm at the surface and 0.29 nm close to the centre (Figure 4.4 (b)–(d)). The compression of the onion is preserved and no considerable relaxation occurs. But there is a slight change of the shape of the shells.

Another experiment was carried out at 1300°C for a very long time up to 3 hours, and the results are shown in Figure 4.5. After annealing for 3 hours at 1300°C, the compression of the onion is preserved and no measurable relaxation occurs, demonstrating their stability under sustained heating.

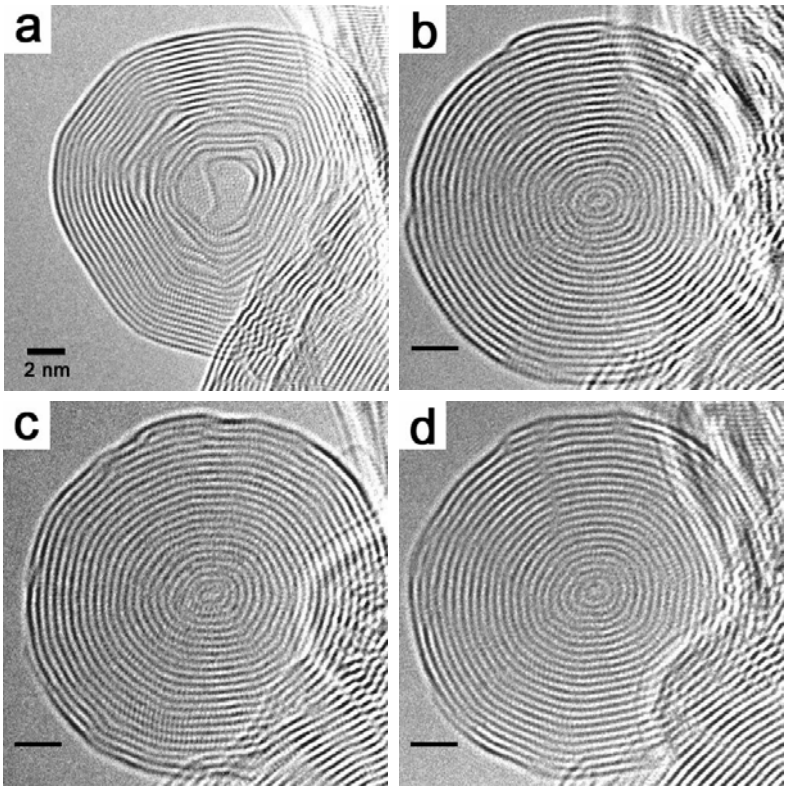

Figure 4.4: Annealing of a carbon onion at 1200°C. (a): before irradiation; (b): after electron irradiation; (c) and (d): after annealing at 1200°C for 120 and 420 seconds, respectively. The compression of the shells is completely preserved after annealing. Scale bar: 2 nm.

Early studies have suggested that the self-compression happens in carbon onions under electron irradiation when carbon atoms are sputtered from planar or curved graphitic layers, leading to the formation of pentagonal and heptagonal rings that induce curvature in the network [17, 106]. Graphenic layers can heal irradiation-induced vacancies by a reconstruction of the lattice, which allows a contraction of a closed graphenic shell due to removal of atoms [20]. Therefore, a tension in each shell arises from the continuous removal of atoms from the outermost layer by sputtering and a redistribution of interstitials within the particle which eventually results in the spherical shape and the contraction of the onions [73]. Onions with coherent shells which were generated under irradiation at high temperature appear to have a lasting stability at room temperature and at least for several hours at temperatures up to 1000°C, although some early studies have indicated that defective carbon onions generated under irradiation at

room temperature might be unstable on a longer time scale [52, 107]. Specimens with self-compressed onions remain unchanged even after keeping at room temperature in air for several months. Thus, it turns out that no non-thermal interstitials exist after the irradiation process in the specimen.

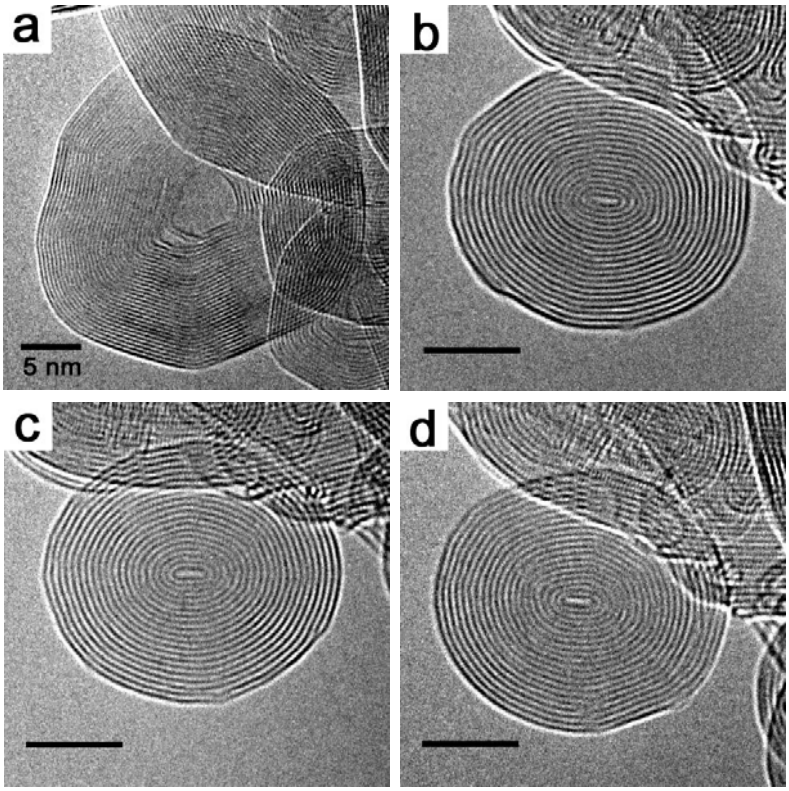

Figure 4.5: Annealing of a carbon onion at 1300°C. (a): before irradiation; (b): after electron irradiation; (c): after *ex-situ* annealing at 1300°C for 1 hour; (d): after *ex-situ* annealing for 3 hours totally. The compression of the shells is completely preserved after annealing. Scale bar: 5 nm.

Figures 4.4 and 4.5 show that there is no obvious increase in the distance between the shells at 1200°C and 1300°C and only a slight change in diameter of the shells, which might be explained by defect reconstruction within the shells, for example, non-hexagonal rings such as in a Haeckelite structure [108]. Many of the energetically unfavourable non-hexagonal rings can be eliminated by the exchange of atoms between the shells and eventually the spherical onion transforms back to the faceted shape. However, Figures 4.1 and 4.2 show the observed relaxation of carbon onions during

annealing at high temperature of 2000°C, which can only be explained by an exchange of carbon atoms between the shells. During relaxation the atoms have to migrate normal to the layers outwards, because the diffusion in a pressure gradient is generally directed towards the low-pressure region. The appearance of the internal hollow as shown in figure 4.1 (c) further proves that an exchange of atoms between the shells has occurred because a considerable expansion of the inner shells is observed.

The morphological change after annealing allows us to obtain information about the long-sought migration of interstitials normal to the layers. It can be estimated that the atoms must travel along a length $\bar{x}$ of at least one interlayer distance and most likely a few spacings (≤ 1 nm) during the annealing time t to lead to the slight relaxation of the particle as observed at the onset temperature 1500°C (Figure 4.3 (c) and (d)). According to the expression for the diffusion coefficient D of one-dimensional diffusion given in Chapter 1:

$$D = \frac{\bar{x}^2}{2t} \tag{4.1}$$

A value of the order $D \approx 3\times10^{-22}$ m^2s^{-1} at 1500°C is obtained. Uncertainties are caused by the difficulty of measuring the mean travel distance $\bar{x}$ of the atoms and the annealing time precisely (it takes some time to heat up and cool down the crucible). The range of error of the measurement is within 8×10^{-23} and 1×10^{-21} m^2s^{-1}. The diffusion coefficient D is related to the activation energy E_a by

$$D = ga^2\nu_0 \exp\left(-\frac{E_a}{k_B T}\right) \tag{4.2}$$

$$= D_0 \exp\left(-\frac{E_a}{k_B T}\right) \tag{4.3}$$

where g is a geometrical factor of the order 0.1, a is the jump distance (here the spacing between the basal planes), ν_0 is an attempt frequency for atom jumps of the order of the Debye frequency, k_B is Boltzmann's constant (1.38×10^{-23} J/K), and T is the absolute temperature. A prefactor D_0 can be estimated by $D_0 = ga^2\nu_0 \approx 4\times10^{-8}$ m^2s^{-1}. An

activation energy of $E_a = 5.0 \pm 0.3$ eV for atom jumps between the layers is obtained with the above diffusion coefficient (3×10^{-22} m^2s^{-1}) at the temperature of 1500°C. The pre-exponential factor is somewhat uncertain [15], but it has only minor influence on the activation energy. With the activation energy E_a of 5.0 eV, the diffusion coefficient at the temperature of 1300°C can be calculated by the equation (4.3) $D \approx 4\times10^{-24}$ m^2s^{-1}. After calculation with equation (4.1) it takes approximately 4 hours for atoms to diffuse over one interlayer distance of 0.33 nm. As expected no detectable relaxation of the shells was observable after annealing at 1300°C up to 3 hours, as shown in Figure 4.5.

The error of ±0.3 eV was given by taking into account the uncertainty of this particular measurement, excluding the possible influence of stress and structural defects. There is a considerable number of non-hexagonal rings in spherical carbon onions. The removal of atoms from these defects might require a slightly lower vacancy formation energy than in planar graphite, which would lead to a lower activation energy for inter-layer jumps. Since the curvature of large onions is low and even the outermost shells of the structures expand, it is reasonable to assume that the activation energy for atom migration normal to the layers in planar graphite is somewhat higher but not too far from the value of 5.0 eV. It is in moderate agreement with diffusion data obtained from ^{14}C tracer (E_a > 5 eV) [92] or boron (E_a = 6.6 eV) [91] diffusion in macroscopic graphite crystals in the 1960s. Theoretical studies have given interstitial migration energies of 2.3 eV [93] or 1.2–1.7 eV [94]. The activation energy for diffusion is the sum of defect formation energy and migration energy, but in the present case (jump of a carbon atom between two layers) these two energies can hardly be separated because no stable Frenkel pairs are generated. In the initial stage of relaxation the exchange of the atoms between the compressed layers might need a lower activation energy than that between the relaxed planar layers because of the presence of stress. But the ongoing expansion of the shells, as shown in Figure 4.1, shows that interstitial diffusion continues even in the relaxed structure.

A redistribution of atoms *within* the layers can occur at much lower temperature due to the lower activation energy for vacancy diffusion in graphene or nanotubes [51, 63, 68]. Such a thermal distribution would lead to morphological changes of the layers but not to considerable changes of their diameter as discussed above which was indeed observed at 1200°C for some particles. The shape of the particles changed slightly but the compression was preserved (shown in Figure 4.4). Therefore, it is concluded that the activation energy for atom migration *within* the basal plane of the layers (via vacancy diffusion) is obviously smaller than that for jumps between the layers, although a precise value for *in*-plane diffusion cannot be derived from the present observations. Other scenarios for atom migration such as the recently reported inter-layer dislocations in nanotubes [100] may also be taken into account, but no experimental evidence for dislocations was found in this study.

4.3.2 Irradiation Experiments

The morphological evolution of carbon nanoparticles under extremely intense (300 keV, 1500 A/cm^2) electron irradiation at 600°C is shown in Figure 4.6. The hollow polyhedral nanoparticle in the starting material produced by the arc-discharge technique before irradiation is shown in Figure 4.6 (a). Figure 4.6 (b)–(j) shows the same particle after irradiation with an extremely intense electron beam for 5 s, 10 s, 15 s, 20 s, 25 s, 30 s, 40 s, 50 s, and 60 s, respectively.

Under intense electron irradiation, a polyhedral carbon nanoparticle with an inner hollow collapsed and deformed to a spherical carbon onion in a self-compressed state, as shown in Figures 4.6 (a)–(d). Continuous irradiation made the onion shrink by sputtering, as shown in Figures 4.6 (d)–(j).

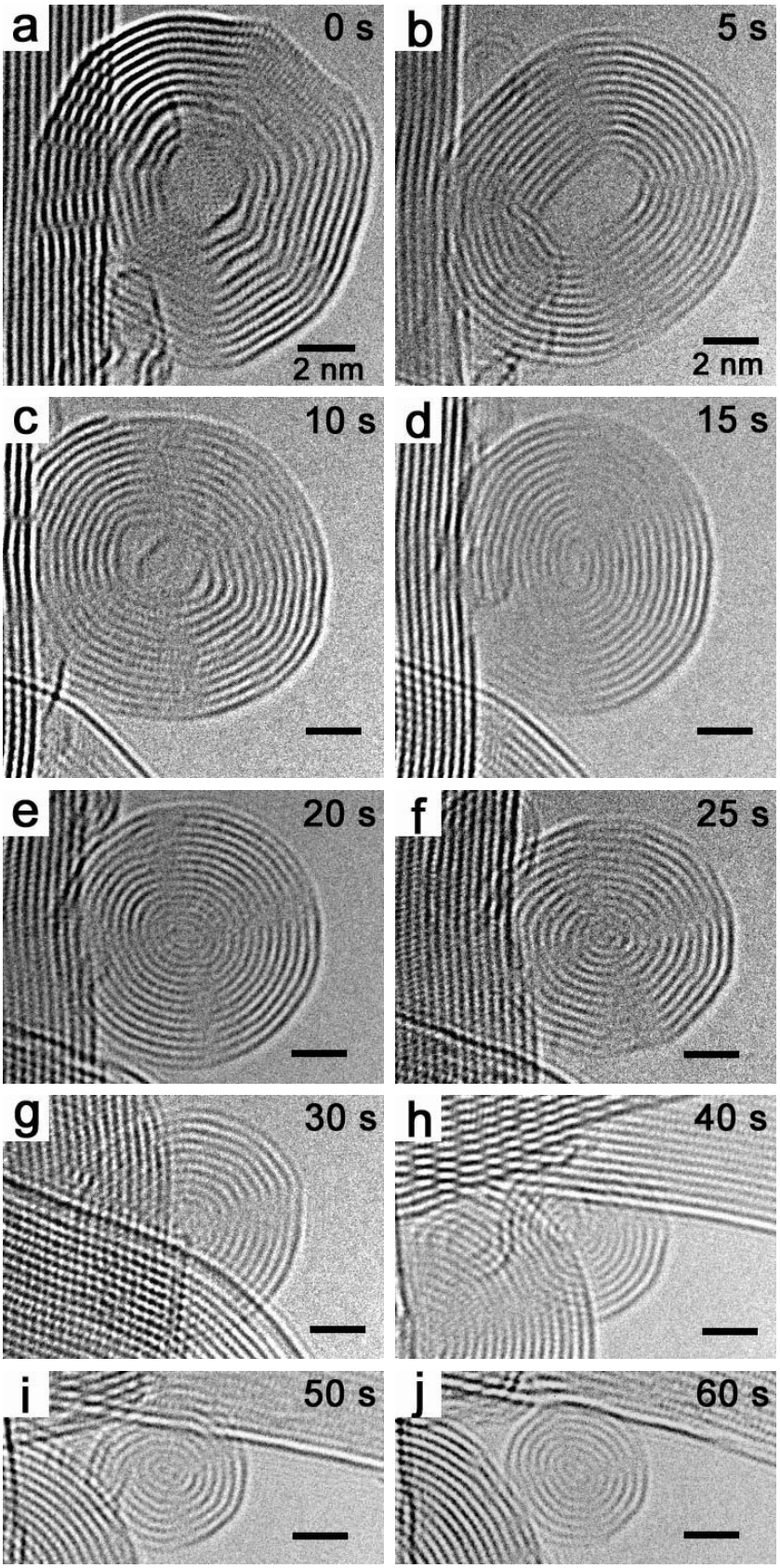

Figure 4.6: Morphological evolution of a carbon nanoparticle under extremely intense (1500 A/cm^2) electron irradiation at 600°C.

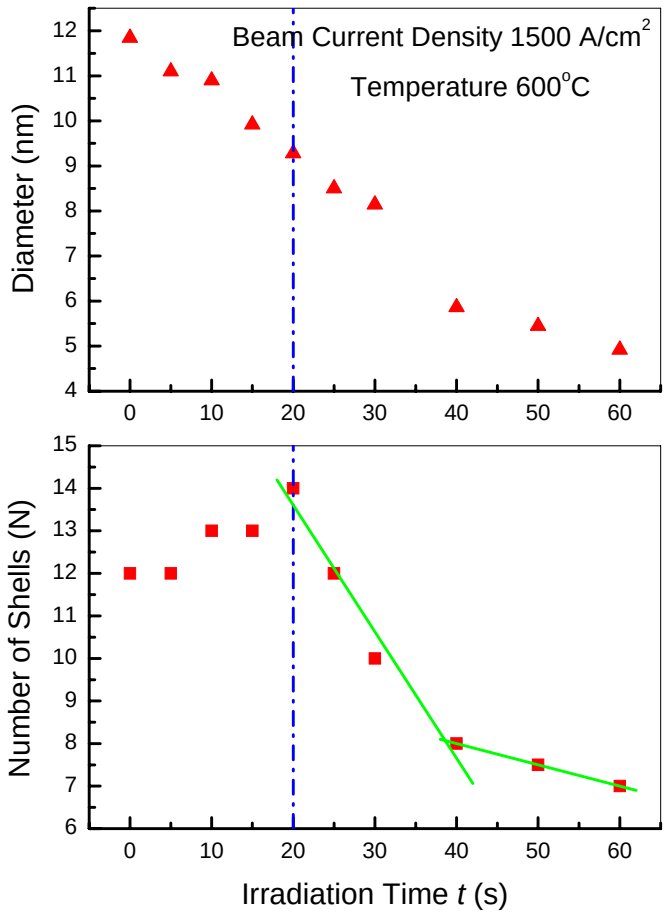

Figure 4.7: Diameter and number of shells of a carbon nanoparticle as a function of the irradiation time.

The size and the number of shells of the nanoparticle as a function of irradiation time are plotted in Figure 4.7. Considering the uncertainties due to the shape of the nanoparticles, the number of shells as a function of the irradiation time should give more direct information. The shrinkage of the onions due to sputtering is clearly visible. In the first 20 seconds the number of shells increased, corresponding to the collapse and deformation of the hollow polyhedral carbon nanoparticle into a spherical onion (Figures 4.6 (a)–(d)). In the range of 20 to 60 seconds there are two slopes (green lines) in the lower figure: one is in the range of 20 to 40 seconds and the other is in that after 40 seconds. The slope (k) with a negative value represents the decrease of the number of

shells in unit time ($k = -\left|\frac{\Delta N}{\Delta t}\right|$). Thus, a slope with a higher absolute value shows a lower stability of the onion. From Figure 4.7 it can be seen clearly that the smaller the onion is, the more stable it is.

An early study by M. S. Zwanger *et al.* indicated that carbon onions generated with an electron beam at room temperature are unstable after irradiation [52]. It has been proposed that dangling bonds in adjacent unstructured material may initiate the breaking up of the outer shells and imperfections in the shells should accelerate it. However, in the present work annealing at the observation temperature of 600°C obviously improves the stability and perfection of the carbon nanostructures under moderate electron irradiation because the shells are coherent. And it was also found that the stability of carbon onions increases with decreasing size, which is not explained theoretically to date. It is very difficult to observe the evolution of smaller onions with less than 5 layers, because on the one hand such small onions frequently jump or move behind large carbon nanoparticles under intense electron irradiation, which makes their imaging impossible; on the other hand they are so stable that a much longer time would be needed to peel off one layer. Theoretical work on the stability of carbon onions is also difficult due to the uncertainty of their precise structure and the size of the system. Detailed calculations on the stability of large multilayer carbon onions are not yet available.

Chapter 5 Diffusion of Carbon Atoms inside Single-Walled Carbon Nanotubes

The mobility of interstitial carbon atoms in SWCNTs along the axial direction was determined by the combination of electron irradiation experiments in the TEM with kinetic Monte Carlo (kMC) simulations. Accompanying simulations were carried out by the group of Dr. A. Krasheninnikov and Prof. K. Nordlund at the University of Helsinki. The irradiation dose necessary to cut nanotubes with a focused electron beam was measured repeatedly as a function of the separation between the two cuts at different temperatures. As the cutting speed is related to the migration of displaced carbon atoms trapped inside the tube and their recombination with vacancies at the gap, information about the mobility of atoms was available. A migration barrier of about 0.25 eV for carbon atoms diffusing inside nanotubes is obtained. This is an experimental confirmation of the remarkably high mobility of interstitial atoms inside carbon nanotubes, which shows that nanotubes have potential applications as pipelines for the transport of carbon atoms.

5.1 Introduction

Carbon nanotubes, especially SWCNTs promise applications in many fields of nanotechnology due to their novel structures and properties. Many methods are developed to tailor them locally in order to get new structures and properties. In addition to chemical methods, this can also be achieved by spatially localized irradiation with energetic particles, combined with high-temperature annealing. Recent experiments demonstrated that the morphology of nanotubes can be changed with nearly atomic precision by irradiation with electron or ion beams of high energy [23–27]. Moreover, in many cases particle irradiation may lead to structural

self-organization or self-assembly in carbon nanostructures [20]. All these phenomena are due to a delicate balance between defect creation, migration and annealing. Therefore, detailed knowledge of creation, migration and annihilation of defects in nanostructured carbon materials is highly indispensable.

Point defects created by particle irradiation in carbon nanotubes are mainly vacancies and interstitials. The former can locally change the curvature of the shell, and the latter can occupy two possible positions: carbon interstitial atoms can be attached to the nanotube on the inner or outer surface. In this chapter we denote carbon atoms inside SWCNTs as interstitials, and atoms absorbed on the outer surface as adatoms. A lot of theoretical work on diffusion of point defects in SWCNTs systems has already been done [42–46] because this subject is ideally suited for computational studies, as no van der Waals interaction (as in MWCNTs) has to be taken into account. However, until now, no quantitative experimental information on the mobility of such defects was available. Although recent *in-situ* experiments in the TEM made it possible to create defects in nanotubes with energetic electrons and monitor the defect evolution at room [26, 109] and elevated [68] temperatures, the low visibility of point defects and the limited time resolution in the TEM made the direct measurement of defect migration barriers difficult. The situation in nanotubes is not the same as in graphite because graphene sheets in nanotubes are curved and the separation between the sheets and the stacking order of MWCNTs are completely different from graphite. Moreover, recent theoretical results [47, 48] are inconsistent with the old experimental data on migration energies of point defects in graphite [15]. Particularly, an early study [45] has qualitatively shown that the hollow inside nanotubes plays an important role in defect evolution because interstitial carbon atoms have a high mobility in the channel and nanotubes may act as pipelines for the transport of carbon atoms. Thus, quantitative experimental information on the mobility of carbon interstitials in SWCNTs is desired and valuable.

In the present study, quantitative experimental information on the mobility of carbon interstitials in SWCNTs was obtained by cutting SWCNT bundles with an

intensely focused electron beam at various temperatures in the TEM. As the cutting speed is related to the defect annealing rate, such a set-up makes it possible to measure the migration barrier for carbon atoms trapped inside SWCNTs. Collaboration with a group carrying out kMC simulations was necessary to validate the interpretation of the results and get a complete picture of defect migration.

5.2. Experimental

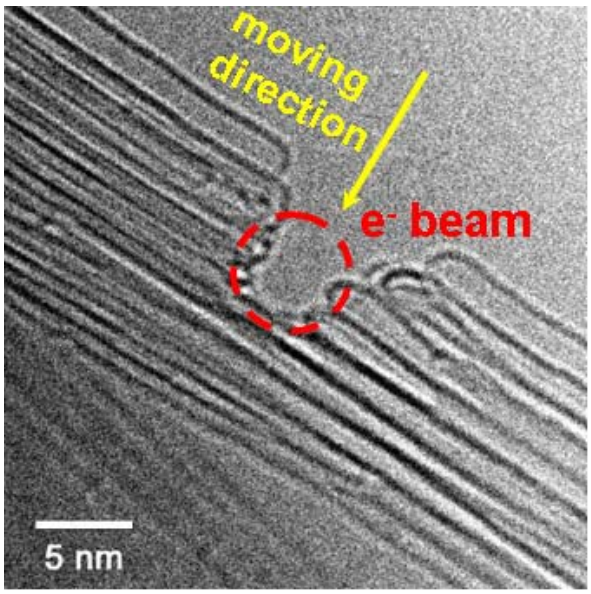

Figure 5.1: TEM picture of a SWCNT bundle partially cut by an electron beam. Red dashed circle represents the electron beam diameter and the moving direction of the electron beam is arrowed in yellow.

Commercially available powder of SWCNTs bundles was ultrasonicated in pure ethanol for a few minutes. The well-dispersed solution was dropped on a pure Mo grid, and then dried in air. In the present study, Mo grids were used instead of Cu grids in order to withstand temperatures up to 900°C. The experiments were carried out in the TEM, where the specimens were heated up to temperatures in the range of 400–900°C by a heating stage during cutting and inspection. A SWCNT bundle was cut by focusing the electron beam on a spot of 4–5 nm in diameter (FWHM of the Gaussian beam

profile, the dashed circle in Figure 5.1) with typical beam current densities of 2000–4000 A/cm^2 and slowly moving the beam across the bundle (direction is arrowed in Figure 5.1). Although irradiation in a spot does not offer good imaging conditions, the tube under the beam was still visible during cutting.

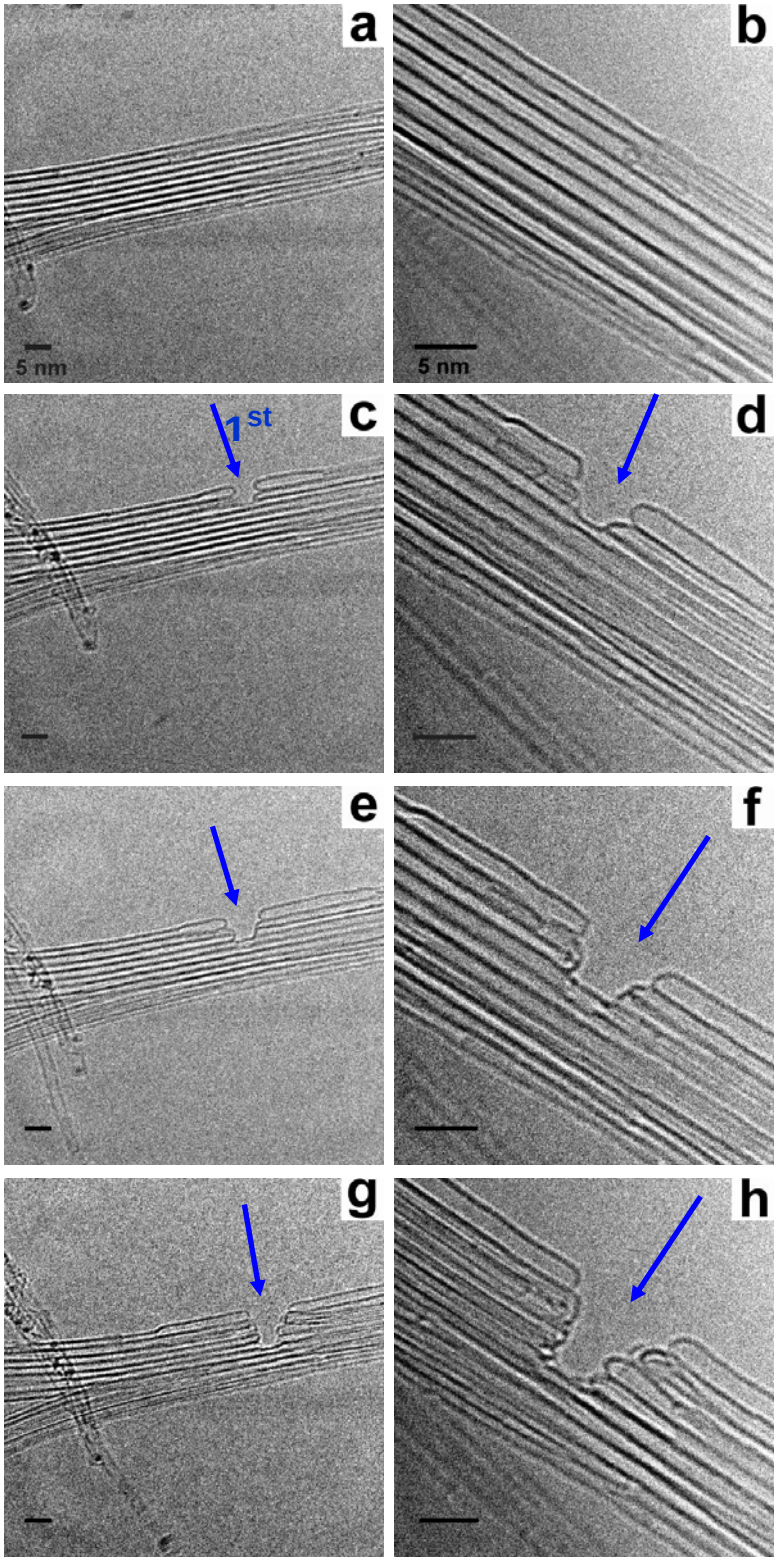

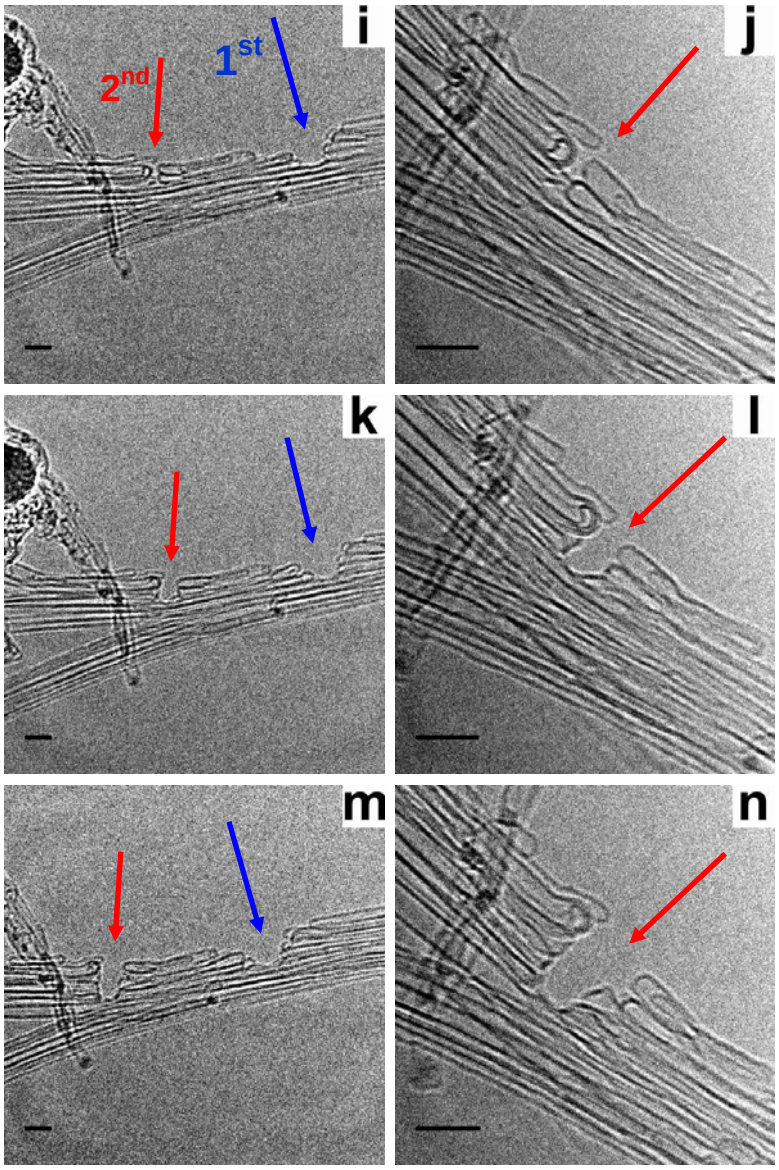

Figure 5.2: The procedure of cutting a SWNT bundle: before cutting at low (a) and high (b) magnification; the first cut of the bundle is shown step by step at low (c, e, g) and high (d, f, h) magnification; the second cut is shown step by step at low (i, k, m) and high (j, l, n) magnification. The arrows in blue and red point to the gap made by 1st cut and 2nd cut, respectively. Scale bar: 5 nm.

The procedure of cutting a SWCNT bundle is shown in Figure 5.2. At first, a clean SWCNTs bundle was chosen (in Figure 5.2 (a) and (b)) and cut somewhere far away from the ends (arrowed in blue in Figure 5.2 (c) and (d)). The electron dose necessary for cutting and the cutting speed were measured by moving the electron beam across the SWCNT bundle. It is worthy to be noted that such a cutting speed is critical, i.e. a lower

speed would waste electrons because the gap has already been achieved; a higher speed would result in damage but not complete cutting. The first cutting speed (ν_1 in units of nm/s) was obtained by measuring the depth of the gap (in units of nm) and the cutting time (in units of seconds), and dividing depth by time, according to the figures 5.2 (c)–(g). Afterwards, at a certain distance from the first cut, the bundle was cut for the second time (arrowed in red in Figures 5.2 (i)–(n)) and the second cutting speed ν_2 was measured in the same way.

The procedure was carried out for various distances between the cuts at 400, 600 and 900°C, respectively. For each measurement of the cutting speed, a fresh SWCNT bundle was chosen, i.e. a new first cut was made and then the speed for the second cut at a certain distance from the first cut was measured.

5.3 Results

Figure 5.3 shows the relative cutting speed ν_2/ν_1 at various temperatures as a function of separation between two cuts L, and the dashed line represents the speed of the first cut. It shows that the second cutting speed (ν_2) was lower than the first one ν_1, which means the dose necessary for the second cut was higher. This is consistent with the results from previous studies [43, 45, 110]. It is evident that the second cutting speed is affected by the presence of the first cut at small separations, but this effect decreases gradually and eventually vanishes with increasing L. At large separations between the cuts the cutting speed for the second cut ν_2 saturated towards ν_1 within the experimental error, as expected. The deviations between ν_1 and ν_2 ($L \rightarrow \infty$) are around 14% at 400°C, but less than 5% at 600 and 900°C. It is also obvious that for a certain L the ratio decreases with increasing temperature after rescaling to $\nu_1 = \nu_2$ ($L \rightarrow \infty$), as more clearly shown in Figure 5.8.

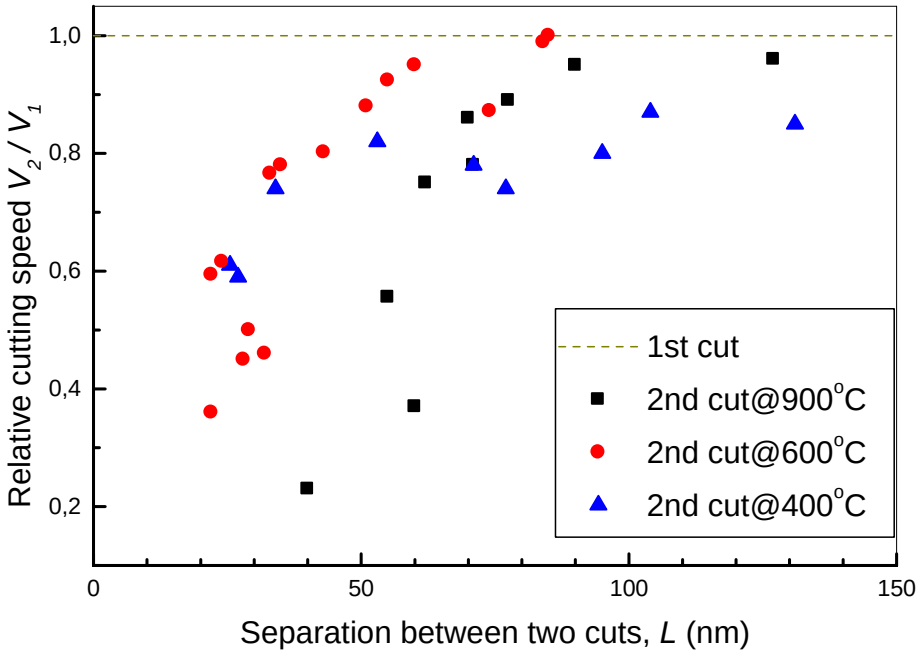

Figure 5.3 Relative cutting speed v_2/ v_1 at various temperatures as a function of separation L between the two cuts. The dashed line represents the cutting speed of the first cut.

5.4 Discussions

Early studies [43, 45] have indicated that the diffusivity of interstitials inside the tube is higher than that of adatoms migrating on the outer surface. Figure 5.4 schematically shows the situation of cutting a SWCNT. When a SWCNT is cut by an electron beam with high energy, at first the shell shrinks and then quickly breaks, leaving an open end due to the knock-on displacement by electron irradiation. Thus, there is a certain number of vacancies and interstitial atoms. As mentioned in Chapter 2, above 300°C vacancies tend to migrate in the shell and coalesce with others which results in the curvature of the shell and eventually closing of the open ends with two fullerenic caps. Such a cap blocks the interstitials generated by the electron beam and limits their migration inside the tube. When a second cut is made, the interstitials diffuse inside the tube and are reflected at the closed end. When they migrate back to the

second cut from where they stem, they annihilate with vacancies in the gap, which makes the cutting speed low. The interstitial also can penetrate the nanotube shell by an atom exchange mechanism, but this needs an activation energy which is at least one order of magnitude higher than for the diffusion along the axis [111]. Therefore, the diffusion of the interstitials along the axis governs the cutting speed.

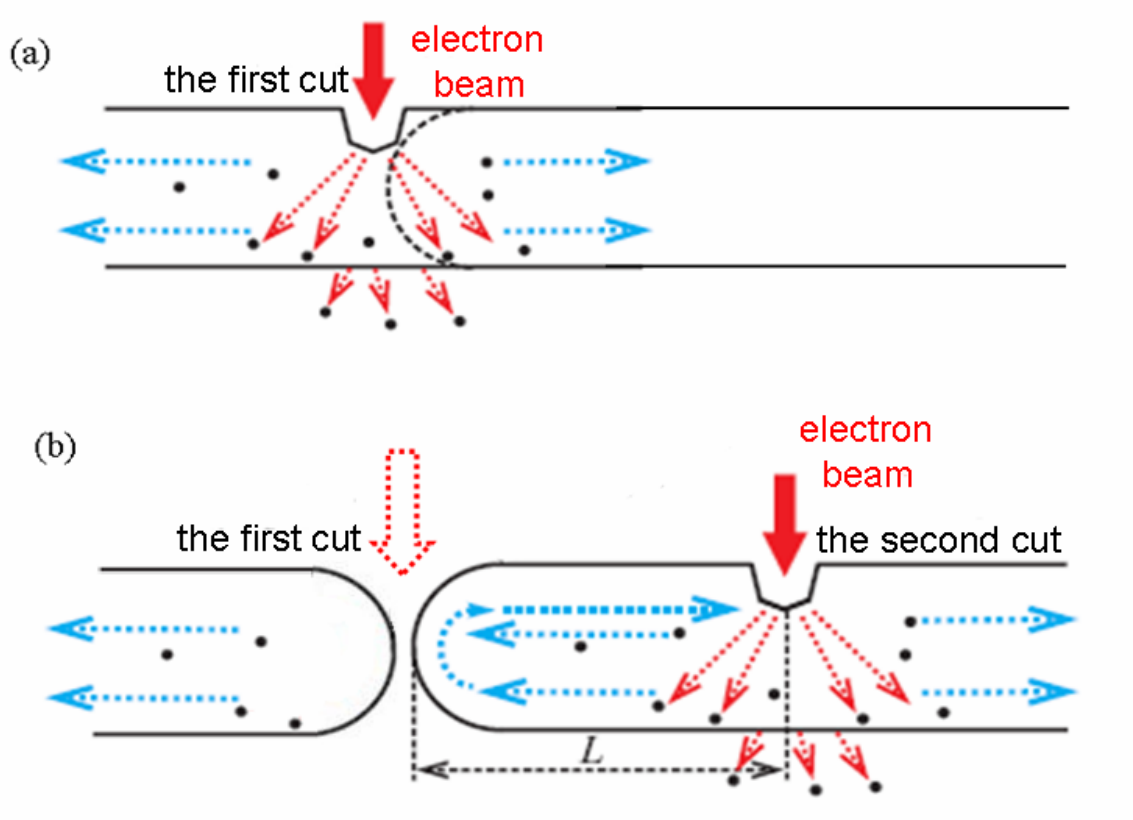

Figure 5.4: Schematic representation of a SWCNT within the bundle cut by the electron beam. (a) The first cut is being made. The interstitials created by the beam move away from the cut in both directions and disappear. Finally, a gap forms due to the agglomeration of vacancies and two fullerenic caps close both open ends. (b) During the development of the second cut, the interstitials have a higher probability for arriving at the cut due to 'reflection' from the cap and annihilating with vacancies thus slowing down the second cutting speed.

In order to get rid of the influence from surrounding, the SWCNT bundles which were cut in this study were chosen as clean as possible, just like the bundle in Figure 5.2. There are often contaminations, such as amorphous carbon (shown in Figure 5.5 (a))

and metal nanoparticles (arrowed in Figure 5.5 (b)) remaining as catalysts from the process of production of SWCNTs. These contaminations may have an influence on the diffusion of interstitial atoms in carbon nanotubes, but this has not been studied yet.

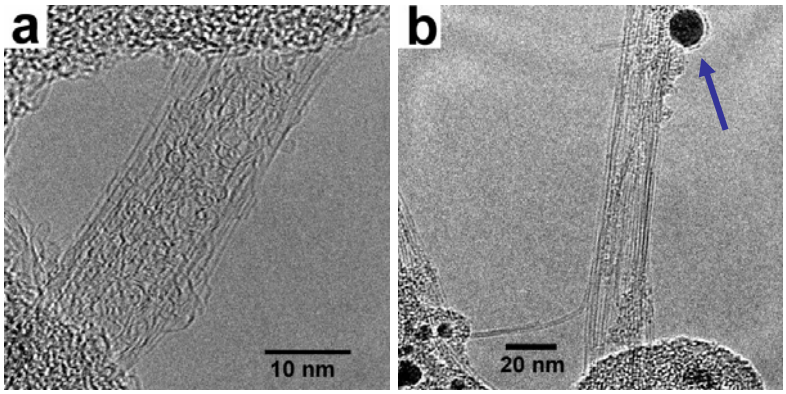

Figure 5.5: Contamination on commercially available bundles of SWCNTs: (a) amorphous carbon and (b) metal nanoparticle.

It is very difficult to achieve a second cut very close to the first cut, for example at distances less than 20 nm, as shown in Figure 5.6. In this case, the SWCNT bundle bends rather than breaks. Thus, there are no experimental data available when the separation between two cuts is less than 20 nm in Figure 5.3.

Several complications have to be taken into account. We deal with SWCNT bundles instead of individual SWCNTs because of the better accuracy in the determination of the cutting time (somewhat less than 4 seconds for one tube under the present conditions.). The mobility of atoms on the outer surface could possibly be influenced by adjacent tubes. For comparison, several isolated SWCNTs were cut at 400 and 600°C (in Figure 5.7) to get a value for the cutting speed of the first cut. With the measurement of the electron beam current density which can be done by measuring the current on the screen in the viewing chamber of the electron microscope and the irradiation time, a typical electron dose for the cutting of a pristine SWCNT (first cut) at 600°C is estimated to be approximately 10^9 electrons/nm^2

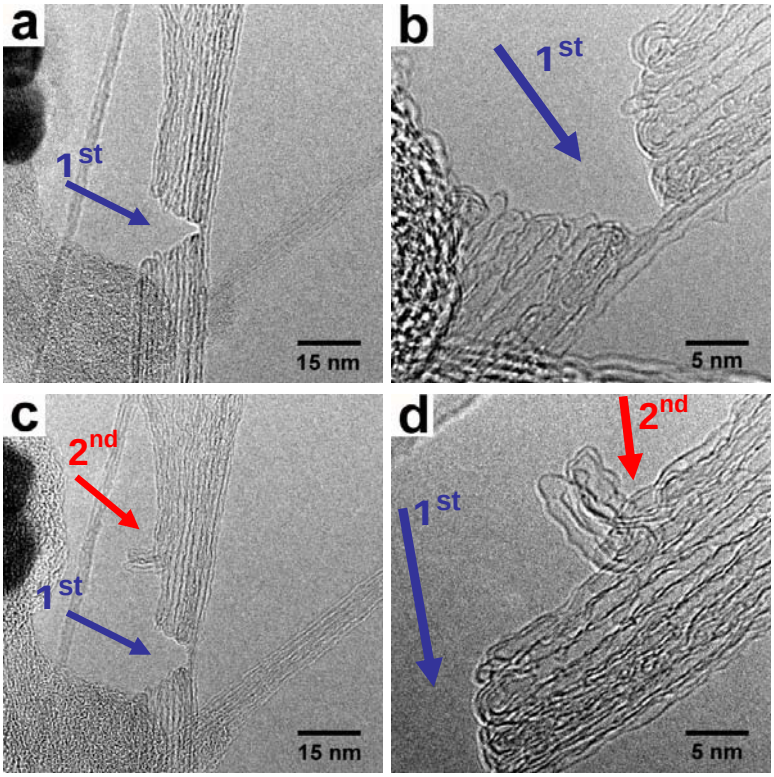

Figure 5.6: The case that the second cut is very close to the first one: (a) and (b) are the first cut at low and high magnification, respectively; when the second cut is very close to the first cut, the SWCNT bundle bends instead of breaking (c and d). The first cut is arrowed in blue and the second cut is arrowed in red.

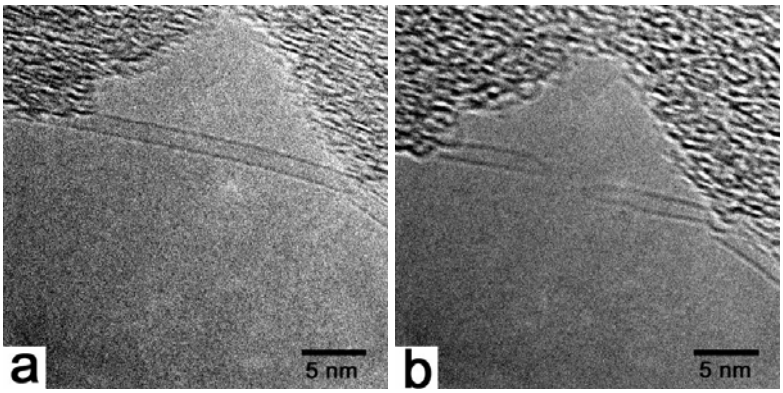

Figure 5.7: The cutting of an isolated SWCNT: (a) before and (b) after cutting.

Table 5.1 shows at the same temperature the absolute cutting speed of the first cut for the SWCNTs bundles which is generally lower than that for an isolated SWCNT in the investigated temperature range. The presence of nearby tubes and reduction of open

space which would make the migration of carbon atoms inside inter-tube channels slower than for free-standing SWCNTs should be responsible for it. Secondly, the first cutting speed increases with decreasing temperature both for an isolated SWCNT and the bundles, because the annealing is faster at higher temperature.

Table 5.1: The absolute cutting speed of the first cut for both SWCNT bundles and isolated SWCNTs at various temperatures.

	400°C	**600°C**	**900°C**
Isolated	(0.5 ~ 0.8) nm/s av. 0.65 nm/s	0.50 nm/s	
Bundle	(0.25 ~ 0.39) nm/s av. 0.32 nm/s	0.30 nm/s	0.20 nm/s

Moreover, it is found that the cutting speed for the first cut ν_1 is influenced by the structural perfection of the tubes and varies from bundle to bundle, especially at 400°C. By measuring ν_1 on many independent SWCNT bundles in the same specimen, an experimental error of about 20%, including uncertainties in the measurement of the cutting speed and possible variations of the necessary dose to cut tubes with different structures, is obtained from the scatter in the data. To account for minor deviation between ν_1 and ν_2 ($L \rightarrow \infty$), it is assumed that $\nu_1 = \nu_2$ ($L \rightarrow \infty$) and the relative cutting speed ν_2/ν_1 is used for the analysis. As mentioned above, at 400°C ν_2 ($L \rightarrow \infty$) saturates towards a value which is 14% less than ν_1. This is not fully understood. A possible explanation is the different annealing of pre-existing defects such as small carbon clusters at different temperatures or the agglomeration of defects created during the first cut.

The following analysis of the data has been carried out by our collaborators, the group of Dr. A. Krasheninnikov and Prof. K. Nordlund at the University of Helsinki.

If a drop in the cutting speed at small separations originates from a different distribution of interstitials in nanotubes, which is affected by temperature and the presence of the cap at the first cut, the cutting speed can be assumed as:

$$\nu_2 = \nu_1 - \Delta\nu \tag{5.1}$$

where Δν is a drop in the cutting speed due to the recombination of vacancies at the second cut with the interstitials 'reflected' back from the gap induced by the first cut. Δν is proportional to the number n of the interstitials which recombined with vacancies. The higher the n, the slower the cutting process is. It can be further assumed that $n \sim \tau^{-1}$, where τ is the time required for the interstitial to travel to the cap of the tube induced by the first cut and back.

It is known that in a quasi-one-dimensional system [112],

$$\tau \sim L^2 / D \tag{5.2}$$

where D is the diffusivity of the created defects,

$$D = D_0 \exp\left[-E_m / k_B T\right] \tag{5.3}$$

where D_0 is a constant prefactor, E_m is the migration barrier, k_B is the Boltzmann's constant and T is the absolute temperature.

By combining equations (5.1)–(5.3), the relative cutting speed ν_2/ν_1 in terms of E_m and L can be expressed as:

$$\nu_2 / \nu_1 = 1 - A(T) / L^2 \tag{5.4}$$

$$A(T) = A_0 \exp\left[-E_m / k_B T\right] \tag{5.5}$$

The migration barrier E_m can now be deduced from the experimental data (symbols in Figure 5.8) by fitting coefficients A with equations (5.4) and (5.5) at different temperatures, and all curves are rescaled: less than 5% at 600 and 900°C; 14% at 400°C (shown in Figure 5.8). The best fit gave E_m = 0.25±0.05 eV. The lower and the upper limits on E_m can also be calculated as 0.1 and 0.4 eV by taking into account two lower (400 and 600°C) and higher (600 and 900°C) temperatures, respectively. Thus, based on the experimental results, it can be concluded that the migration energy along the tube

axis of single interstitials inside the open hollow of the nanotubes is indeed quite small, in the range of 0.2–0.3 eV, corroborating the predicted theoretical results [43, 45].

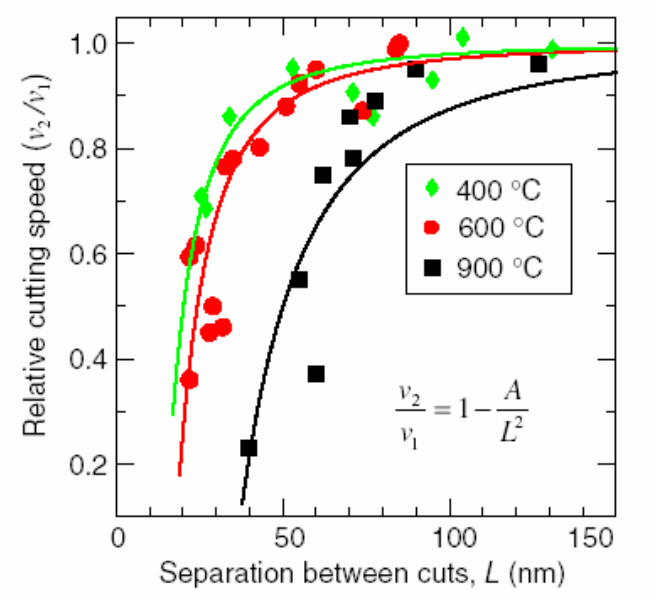

Figure 5.8: Relative cutting speed v_2/v_1 at various temperatures as a function of separation between the cuts L. Symbols stand for the experimental data, solid lines are fits obtained with the equation (5.4). All curves were scaled to $v_1 = v_2$ ($L \rightarrow \infty$): less than 5% at 600 and 900°C, 14% at 400°C. The error of each measurement is approximately 20%.

Actually, various diffusion paths for point defects are possible, because a nanotube is not a real 1D system. A kMC code has been recently developed by our collaborators [111] and used to gain insight into the atomic scale processes which occurs during the electron irradiation. The response of the SWCNT to electron irradiation was available by simulating the migration, annihilation and clustering of point defects on a SWCNT, including single vacancies, adatoms and interstitials, on a macroscopic timescale up to several minutes. Thus, the migration energies and annihilation characteristics were obtained from density functional based calculations [43, 45, 46].

The Helsinki group developed a model by taking an armchair (10, 10) nanotube with a length of 2 μm and diameter of 1.3 nm close to the nanotubes used in the experiments in size (shown in Figure 5.7 (a)). The closure of the structure due to the

first cut was modeled as a hard wall which reflects all incoming interstitials. Based on the experimental conditions and estimation of displacement cross-section [113, 114], the beam was assumed to produce 2.5 displacements $atom^{-1}s^{-1}$ with a Gaussian probility distribution around the center of the beam.

The results of the simulations at T = 400, 500 and 600°C and for L in the range of 10–90 nm are shown in Figure 5.9. The simulations at temperatures higher than 600°C could not be achieved due to computational limitations, because the simulation time needed to cut a SWCNT increases exponentially with temperature in the computational model. This resulted in a high scatter in the kMC results at 600°C so that the data could not be fit well.

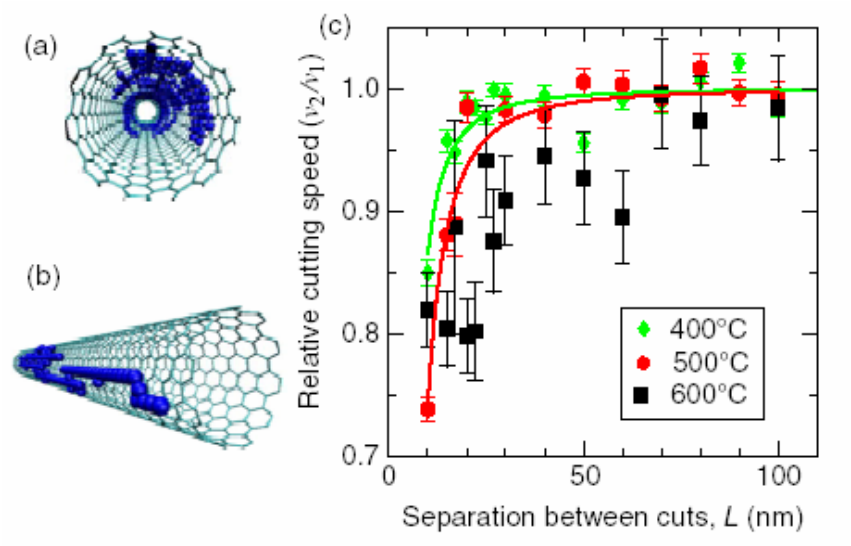

Figure 5.9: Results of kMC simulations carried out by the group of Dr. A. Krasheninnikov at the University of Helsinki. (a) Trajectory of an interstitial inside a (10, 10) nanotube at T = 500°C during 30 ns. (b) Trajectory of an adatom at T = 500°C during 1 ms. Note the difference in the timescale. (c) Relative velocity for the second cut as obtained by the kMC simulations as a function of the separation between the cuts. Solid lines show the theoretical curves obtained through equation (5.5) at different temperatures.

The theoretical result confirms that the drop of cutting speed can be understood

within the simple theoretical model described by equation (5.2). A detailed analysis of the trajectories showed that interstitials tend to spiral inside the tube, while the trajectories of adatoms are closer to straight lines due to curvature effects [43], as shown in Figure 5.9 (a) and (b). Although adatoms with a migration barrier of about 0.7 eV also contribute to annealing at temperatures over 500°C, it is undoubted that the probability for an interstitial to 'meet' a vacancy is higher. More detailed theoretical work can be found in our paper [115].

Here, two facts are worth to be mentioned. Firstly, the migration barrier of carbon interstitials inside the inner hollow of SWCNTs obtained from the present work is an average value because the diffusivity of interstitials in a particular tube should depend on its chirality. Secondly, the theoretical simulation is just qualitatively consistent with the more complicated experimental situation due to two reasons. The kMC simulations were carried out on a fixed lattice. It is known that carbon nanotubes shrink under irradiation [45], and there may be a barrier for recombination of interstitials and vacancies due to the formation of new bonds at pentagons [46], especially in divacancies. Furthermore, in actual experiments interstitials may be incorporated into the lattice at the first cut and annihilate with pre-existing defects due to restructuring of the carbon network, which is beyond the kMC model.

Chapter 6 Diffusion of Metal Atoms in Graphene

Metal atoms play an important role in technology of carbon nanostructures, especially in the catalytic formation of carbon nanotubes. In the present work, the location and migration of individual gold and platinum atoms in graphene layers in a temperature range of 600–700°C were monitored in real-time by high-resolution TEM. Au and Pt atoms are located on vacancies in the graphene lattice and migrate by thermal jumps between different lattice sites. The activation energy was obtained to be 2.5 eV for migration of Pt and Au within graphene planes. However, Pt atoms migrate along in the axial direction in MWCNTs and the open edge of graphene with a lower activation energy of 2.3 eV, which means the diffusion in curved layers of carbon nanotubes is faster than in planar graphene sheets.

6.1 Introduction

The discovery of graphene, a single layer of carbon atoms packed into a benzene-ring structure, has sparked much interest in the past decade. It is regarded as the basic building block for all graphite materials. Graphene with its real one-layer structure became first available in the cylindrically closed shape of SWCNTs [88, 89]. However, recently flat sheets of graphene have been isolated by either chemical intercalation [116, 117] or mechanical exfoliation [118], but graphene planes prepared by the former method tend to scroll to multilayered sheets. It has been found that graphene as well as SWCNTs have unique and outstanding mechanical and electrical properties [49, 119, 120].

Metal atoms have strong interaction with carbon atoms in graphene and their presence in carbon nanostructures consisting of one or several graphene layers has a major influence on the properties of these systems. In addition, metal atoms also play a

central role in the catalytic formation and growth of graphitic structures such as carbon nanotubes [121]. However, their catalytic action is difficult to investigate in experiments because individual metal atoms can hardly be observed by techniques of microscopic imaging during the catalytic process. A lot of theoretical work on the interaction between metal and carbon atoms has already been done mainly based on energy calculations and molecular dynamics [42, 44, 121–123]. Therefore, an experimental observation of the behaviour of individual metal atoms in graphene layers is highly desirable.

In the TEM the scattering of the electron beam at single carbon atoms is quite low, but heavy atoms can be seen under favourable conditions [124]. It should be stressed that the limiting factor in the visibility of single atoms is not the lateral resolution of the TEM, as it is usually believed, but the signal-to-noise ratio in the image recording. It is also well known that TEM image contrast arises because of the scattering of the incident beam by the specimen and the regions of the specimen with heavy atoms scatter more electrons than those with light atoms at the same thickness. Therefore, in TEM images the regions of heavy atoms appear darker than those of light atoms. Individual heavy atoms on light substrates have already been observed in early TEM studies by Iijima [125] and later the migration of single tungsten atoms on MgO (001) surfaces was investigated by using *in-situ* high-resolution TEM techniques [126]. The early study also has demonstrated individual metal atoms (Co and Au) in graphitic nanostructures can be seen in TEM images due to the large mass difference between carbon and heavy metal atoms [127]. As mentioned above, recently monoatomic graphene layers have been isolated successfully. They have already been subject of TEM studies [128] and can be considered as the thinnest possible substrates. Therefore, heavy atoms in or on graphene should give a clearly detectable contrast for unambiguous imaging.

In the present work, individual Au or Pt atoms in graphene planes consisting of one or two layers have been monitored in real time at high temperatures by using high-resolution TEM. Information about the location of metal atoms in graphene, the bonding between metal and carbon, and the diffusion mechanisms were obtained.

Activation energies for diffusion of metal atoms in graphene layers were also obtained in a temperature range close to the temperature of the technically important metal-assisted CVD process.

6.2 Experimental

In the present work, graphene with one or a few layers was synthesized by the arc-discharge technique. A mixture of Au or Pt powder and pure graphite powder was filled into the hole at the tip of pure graphite anode in the electric arc-discharge apparatus [129, 130]. An arc (40 V, 55 A) was operated in a helium atmosphere (330 mbar) for 5–10 seconds. The deposit on the cathode was dispersed in ethanol and ultrasonicated for a few minutes. And then the well-dispersed material was dropped on standard Cu or Mo grids and dried in air for electron microscopy studies. Imaging and irradiation were carried out in the TEM. The specimens were heated up to 600 or 700°C by a heating stage in the TEM during both observation and imaging in order to speed up the migration of metal and carbon atoms and heal the radiation damage in the graphene layer which may occur under the electron beam. For the sake of improving the visibility of individual metal atoms, the electron dose in the TEM was kept as low as possible for getting a clear image, which was achieved with a beam current density of about 30 A/cm^2. Images with lattice resolution were recorded with a slow-scan CCD camera. Although a longer exposure time can improve the resolution of the TEM image, it should not exceed the residence time of an atom on a lattice site. Therefore, as a compromise, an exposure time of 0.3 seconds was chosen. Every 10–30 seconds still images with an exposure time of 0.3 seconds were taken. The contrast of the micrographs was enhanced by image processing to improve the visibility of the metal atoms.

6.3 Results and Discussions

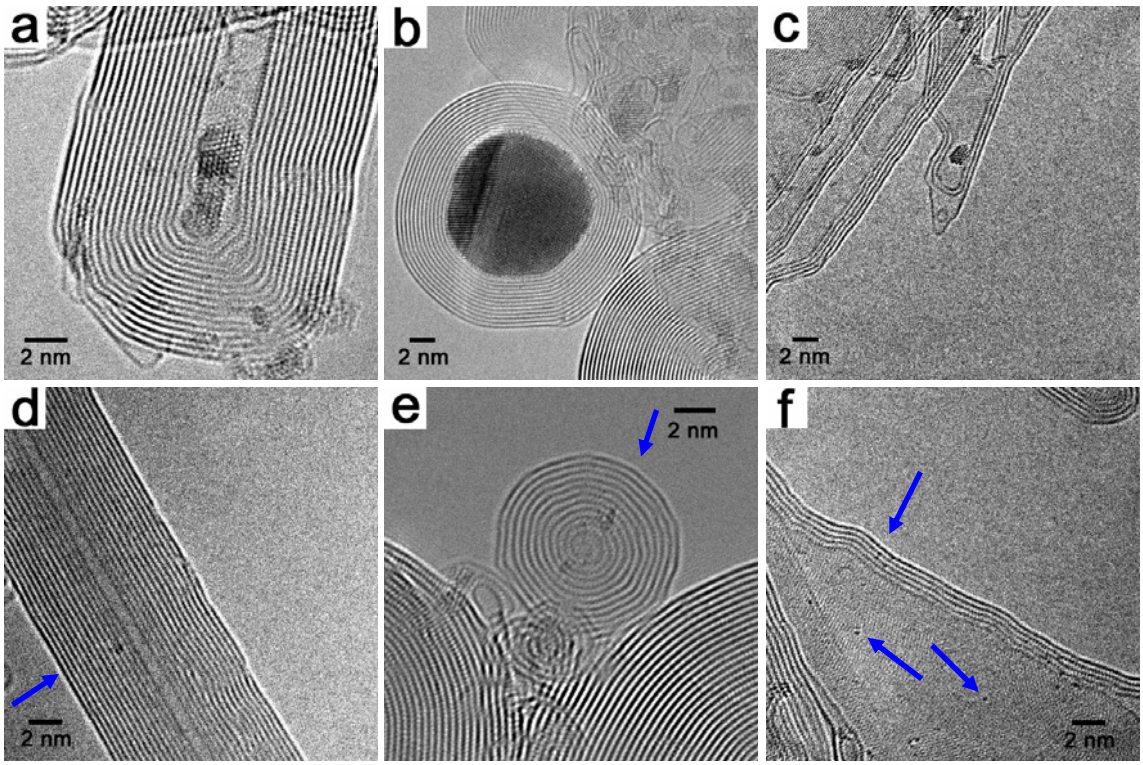

Figure 6.1: Pt nanoparticles or clusters in or on a MWCNT (a), onion-like graphite nanoparticle (b) and graphenic layers (c); single Pt atoms (arrowed in blue) in or on a MWCNT (d), onion-like graphite nanoparticle (e) and graphenic layers (f).

The material synthesized by arc-discharge consisted of MWCNTs (shown in Figure 6.1 (a) and (d)), onion-like graphitic nanoparticles (Figure 6.1 (b) and (e)), and some more or less isolated graphenic sheets with one or a few graphene layers (Figure 6.1 (c) and (f)). The metal (Pt in Figure 6.1) prevailed as nanometer-sized crystals and small clusters of a few atoms in or on the graphitic structures (shown in Figure 6.1 (a), (b) and (c)), or single atoms appearing as dark dots in or on the flat or curved graphenic layers (blue arrow in Figure 6.1 (d), (e) and (f)). However, the contrast of individual metal atoms varies from image to image due to their migration during the recording of the image. The contrast is prominent when the atom remains on a lattice site during the exposure. However, the contrast is weak or even vanishes when the metal atom jumps over one or several lattice distances while the still image is recorded. This was observed

in all image sequences.

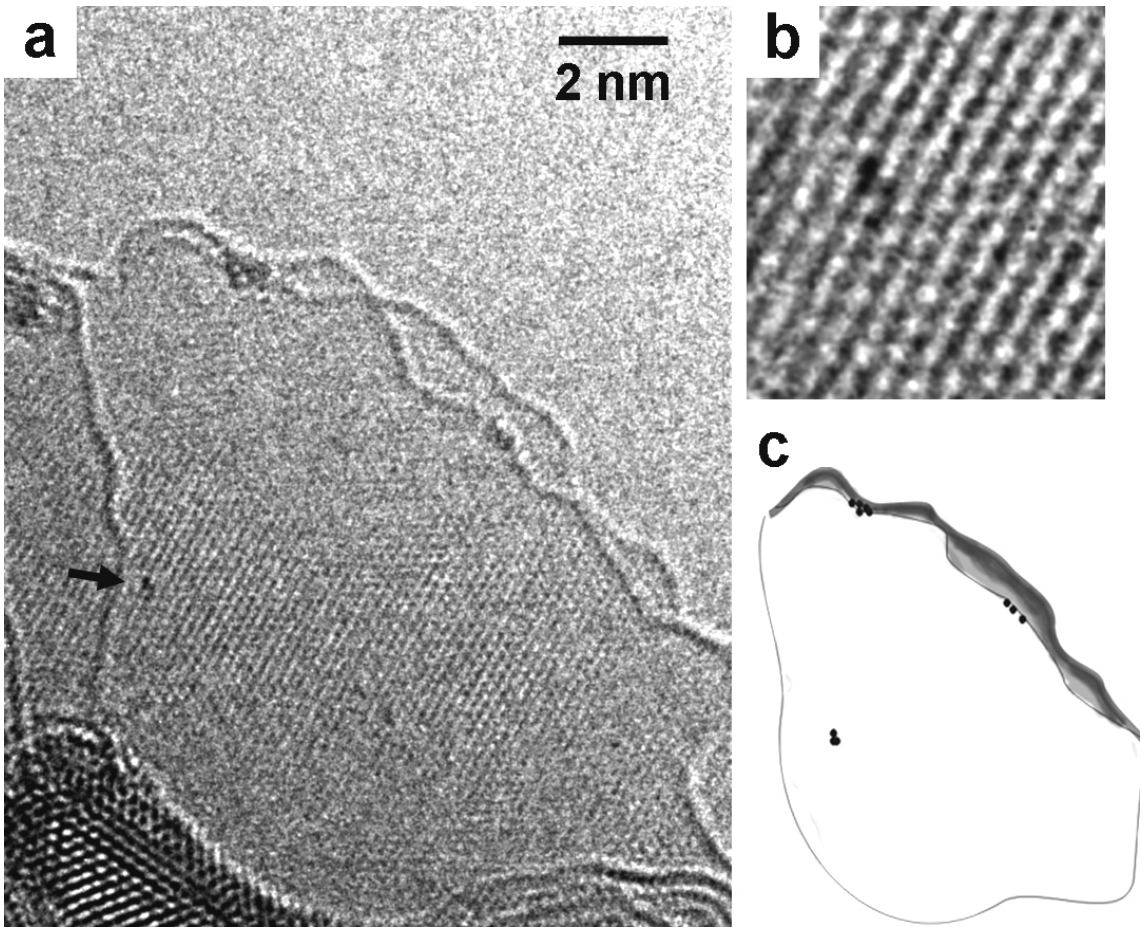

Figure 6.2: (a) Plan-view (viewing direction normal to the layer) of a monolayer of graphene with Pt atoms (arrowed) at 700°C. The geometry is visualized in the drawing in (c). The open edge of the layer rolls up at the top. The edge is the line where some Pt atoms are sitting (inner fringe in the center of the image). A larger Pt crystal is visible on the bottom. (b) An enlarged view of the group of in-plane Pt atoms (black arrow in (a)). The lattice contrast in (b) has been slightly enhanced by Fourier filtering.

In principle, the number of monoatomic layers in the graphitic stacks can be determined only when the layers are in a side-view orientation (viewing direction parallel to the layer surface). However, in most cases, the number of monoatomic layers also can be determined even when the layers are in a plan-view orientation (viewing direction normal to the layer). The edges of the layers are always bent or rolled up,

which makes the determination of the number of layers possible. Generally, the number of fringes with inter-fringe distance of 0.34 nm should correspond to the number of layers (shown in Figure 6.1 (c) and (f)). However, this is only true for bending angles between 90° and somewhat more than 180°. Rolling up with an angle of 270° increases the number of fringes by a factor of two and so on for larger angles, because each graphene layer appears twice in the projection. Figure 6.2 shows a monolayer of graphene with Pt atoms at 700°C. Although there are two fringes at the edge (top), the absence of graphitic fringes with inter-fringe distance of 0.34 nm shows that it is really a monoatomic layer. The contrast of the hexagonal lattice can be seen clearly in the bottom of the area, although the layer is curved. There are Pt crystals formed by the clustering of Pt atoms, as shown in the left bottom in Figure 6.2 (a). Besides these, there are some Pt atoms sitting at the edge of the layer (top). Figure 6.2 (b) shows the magnified view of the area where there is a cluster of about four Pt atoms located in the layer, as arrowed in Figure 6.2 (a). It can be clearly seen that the positions of the Pt atoms coincide well with the positions of carbon atoms in the graphene lattice, which indicates that the Pt atoms are localized on regular lattice sites of carbon atoms.

In order to further determine the locations of the metal atoms, whether they are located in the graphene plane or just sitting on the top of the layers, some images were recorded in side-view direction, as shown in Figure 6.3. This is normally the case at the periphery of curved layers. Figure 6.3 (a) shows a curved two-layered graphenic structure with Au atoms. One atom (arrowed in Figure 6.3 (a)) is located at the periphery which appears here as an edge in the projection because the viewing direction is parallel to the layer. The contrast of the Au atom is high (apparently the atom remained immobile during the exposure) and clearly overlaps with the contrast of the outermost graphene layers. Therefore a location of the Au atom on top of the layer can be excluded. Another example is shown for Au atoms in a MWCNT in Figure 6.3 (b). Although hundreds of such images were recorded, no example of a metal atom sitting clearly on top of the surface of a graphenic layer was found. However, as explained later, the strongest evidence against a location of metal atoms on top of the layer is that the

very low activation energy would make surface diffusion much too fast for giving contrast in still images. In the case of more than one graphene layer, possible inter-layer positions of metal atoms (intercalation) have to be considered, although no strong evidence was found. Even if the metal atoms are located perfectly in-plane, the appearance of an inter-layer position may occur due to projection effects in curved structures. It can be expected that there exists a slight off-layer position of metal atoms when the metal atoms occupy single vacancies in graphene, because the metal-carbon bond is somewhat longer than a carbon-carbon bond [123, 131], and the metal-carbon bond can adjust its length without inducing strains in the graphene layer. An indication for a slight off-layer position might be seen in Figure 6.3 (a). Nevertheless, no clear indications for a considerable off-layer position were seen in the present study.

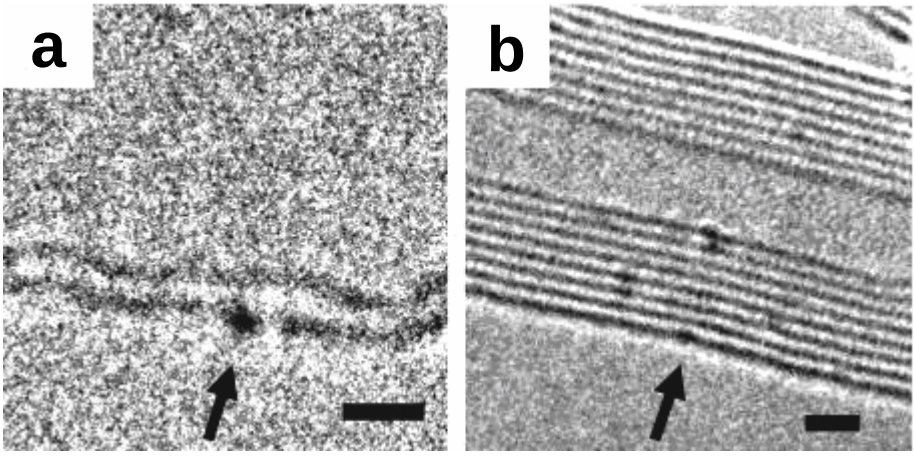

Figure 6.3: Au atoms in curved layers, seen in side-view at 600°C. (a) shows the rolled edge of a two-layer graphene sheet, (b) is a MWCNT. The position of the Au atoms in the outermost layer is arrowed. No considerable off-layer position is detectable. The scale bar is 1 nm.

Figure 6.4 shows Pt atoms in a graphenic structure at 600°C. After migration for approximately one minute, two individual Pt atoms (arrowed in black in Figure 6.4 (a)) join and form a cluster (arrowed in black in Figure 6.4 (b)). However, another Pt atom (arrowed in red) remains almost immobile. Such clusters of two or several Au or Pt atoms were often observed in the present study and in many cases they can be

distinguished from single atoms by the lateral extension of the cluster. The clusters remained stable for a certain time and then dispersed after some time. It is apparent that an attractive force, though weak, acts between the metal atoms within the graphitic lattice.

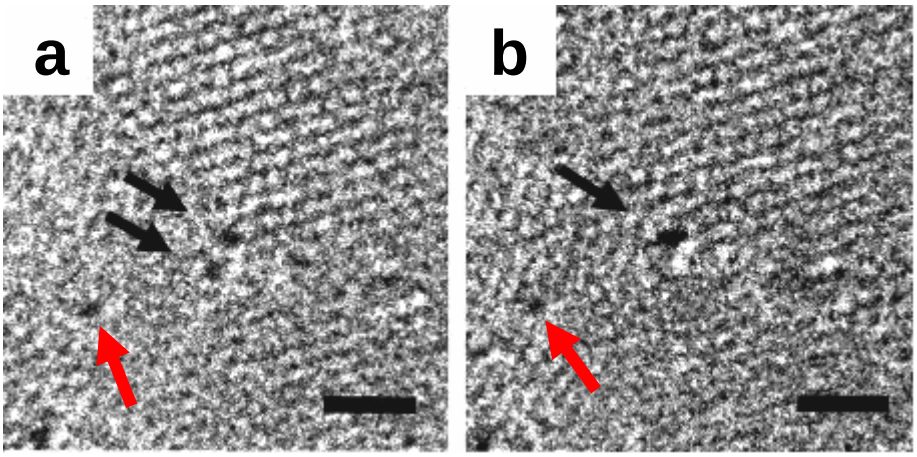

Figure 6.4: Pt atoms in a graphenic sheet at 600°C, seen in plan-view. The image (b) was recorded approximately one minute after (a). Two Pt atoms (arrowed in black) merge and form a cluster, while another Pt atom (arrowed in red) remains almost immobile. The scale bar is 1 nm.

Figure 6.5 shows a sequence of plan-view images for the migration of Pt atoms in the plane of a graphenic layer at 600°C. The brighter area is a hole in a three-layered sheet, so it can be assumed that only single- or two-layers are left in the area of the hole. There is no rolling or bending at this edge due to van der Waals interaction between the layers. Some atoms diffusing two-dimensionally *within* the layer are labelled with "L". The hole in the layer also gives us the possibility to study the tendency of metal atoms to stick to open edges of graphene layers and the one-dimensional diffusion of the atoms (labelled with "E") along the edge. It is obvious that metal atoms prefer edge sites rather than in-plane positions. The preferential residence of metal atoms at the edges of graphenic sheets suggests a more stable configuration at the edges, which is not surprising in view of the presence of dangling bonds. A saturation of the open edges by hydrogen is possible, but hydrogen atoms cannot be detected by electron microscopy. The small cluster of Pt atoms at the open edge (labelled with "E") disperses when the

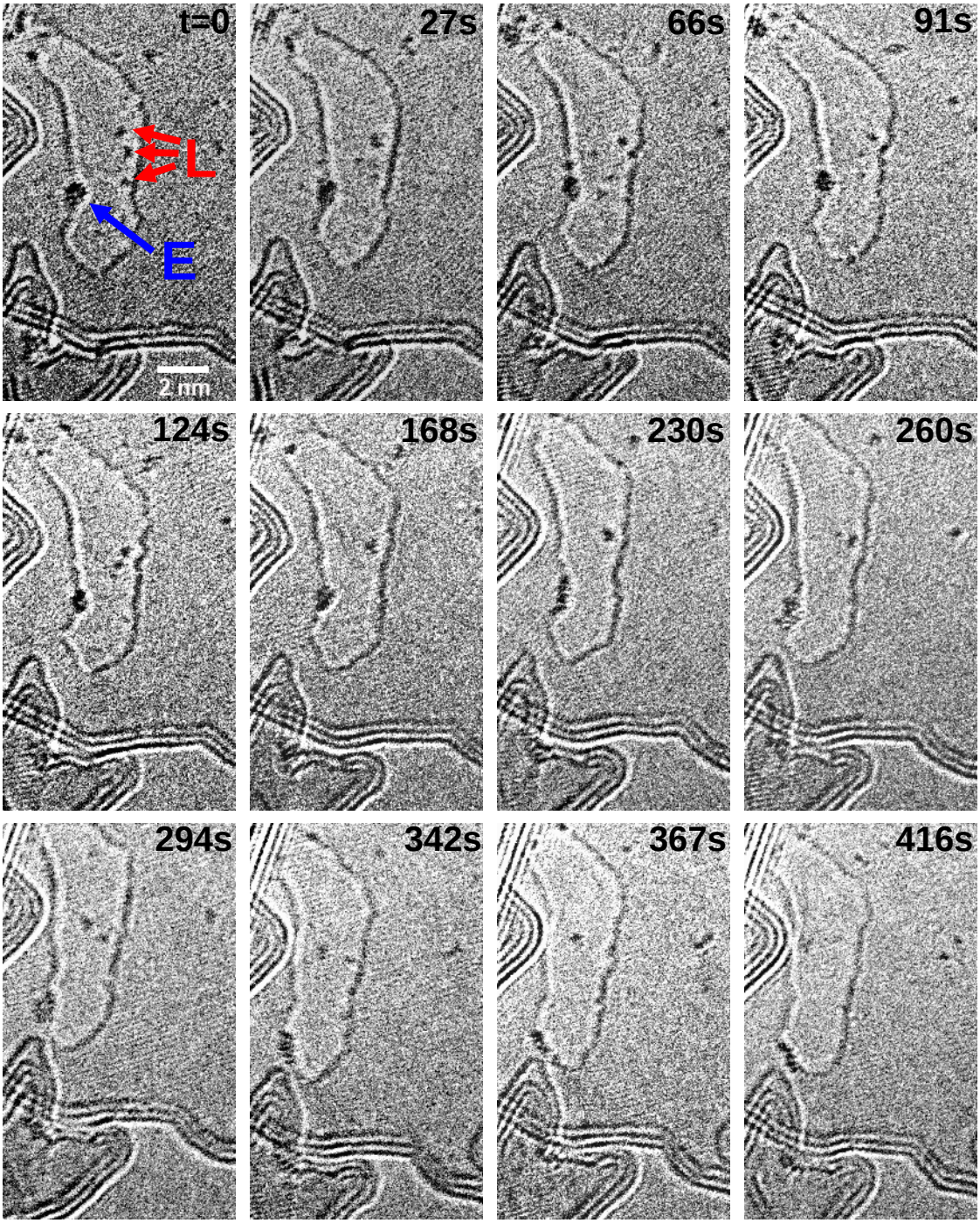

Figure 6.5: Series of images showing the diffusion of Pt atoms at 600°C. Within the vertically elongated hole (the slightly brighter area) in a 2–3-layer graphene sheet we may have a 1–2-layer sheet where Pt atoms are diffusing two-dimensionally (marked with "L"). A cluster of Pt atoms sitting at the edge of the remaining layer (marked with "E") disperses, and the atoms migrate one-dimensionally along the open edge of the graphene layer. The observation time is indicated in each image.

atoms migrate towards the bottom of the edge. The sequence of images clearly shows how the individual Pt atoms change their position by diffusion.

Figure 6.6 shows the two-dimensional migration distance of Au and Pt atoms in graphenic layer (measured in the lateral direction, i.e., along the layer) as a function of time at different temperatures. The data of Pt atoms at 600°C come from the series of atoms labelled with "L" in Figure 6.5. There is considerable scatter in the data because of the statistical nature of diffusion and the experimental error of measuring the jump distance. Nevertheless, it is still clear that the data follow roughly the square-root law of diffusion.

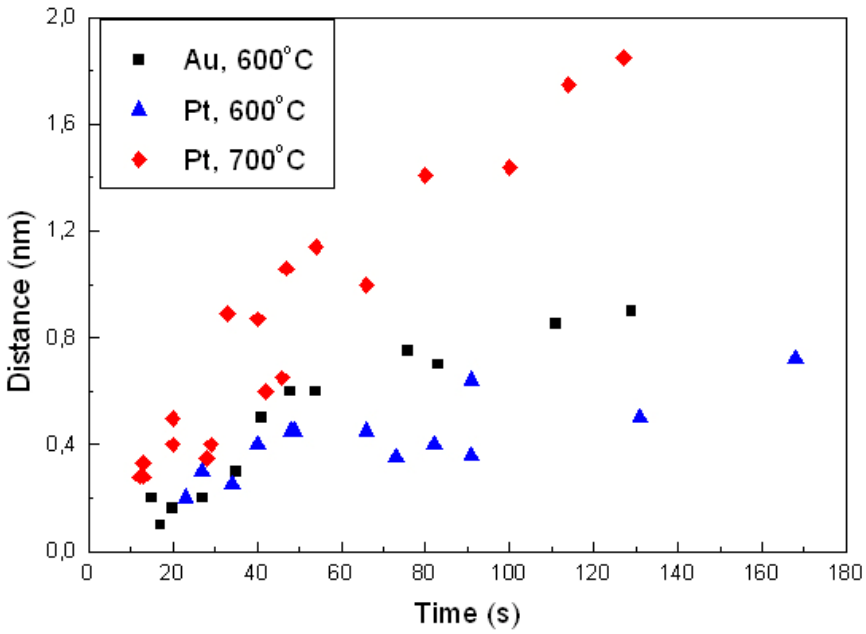

Figure 6.6: Two-dimensional migration length of Au and Pt atoms in graphenic layers measured from micrographs as a function of time at different temperatures.

The two-dimensional diffusion coefficients of Pt and Au atoms in a graphene plane at 600 and 700°C can be derived from the data in Figure 6.6. For an atom migrating in a graphene plane over a mean distance $\bar{x}$ within a time interval t, the coefficient for two-dimensional diffusion is given by

$$D = \frac{\bar{x}^2}{4t} \tag{6.1}$$

The diffusion coefficients D are calculated to be in the range of 6×10^{-22} – 2×10^{-21} m^2/s for Au and 4×10^{-22} – 1×10^{-21} m^2/s for Pt, both at 600°C. The coefficient of Pt at 700°C is in the range of 1 – 7×10^{-21} m^2/s. The dependence of the diffusion coefficient on the activation energy E_a for atom jumps is given by

$$D = ga^2\nu_0 \exp\left(\frac{E_a}{k_B T}\right) \tag{6.2}$$

where g is a geometrical factor slightly smaller than unity, a is the lattice constant, ν_0 is an attempt frequency for atom jumps of the order of the Debye frequency, k_B is Boltzmann's constant, and T is the absolute temperature. At the temperatures of our experiments an activation energy of approximately $E_a \approx 2.5$ eV for both Au and Pt two-dimensionally diffusing in the graphenic planes is obtained. The pre-exponential factor $ga^2\nu_0$ is somewhat uncertain, but is has only minor influence on the activation energy.

Figure 6.7 shows the one-dimensional migration distance for Pt atoms along the open edge of graphene layer (labelled with “E” in Figure 6.5) at 600°C. The diffusion coefficient is obtained to be 3×10^{-21} – 1×10^{-20} m^2/s, based on the data in Figure 6.7 with the formula:

$$D = \frac{\bar{x}^2}{2t} \tag{6.3}$$

Correspondingly, an activation energy of 2.3 eV is obtained with the formula (6.2). Similar values for the migration of Pt atoms along the open edge have been obtained in a theoretical study [123]. Of course, our values are influenced by the facts that a cluster of atoms migrates instead of a single atom and the adjacent graphene plane is present. Therefore, the real value of the activation energy for edge migration might be somewhat lower. As mentioned above, a saturation of the open edges by hydrogen is possible and could lead to a lower diffusivity of metal atoms because hydrogen atoms have to be displaced during the diffusion.

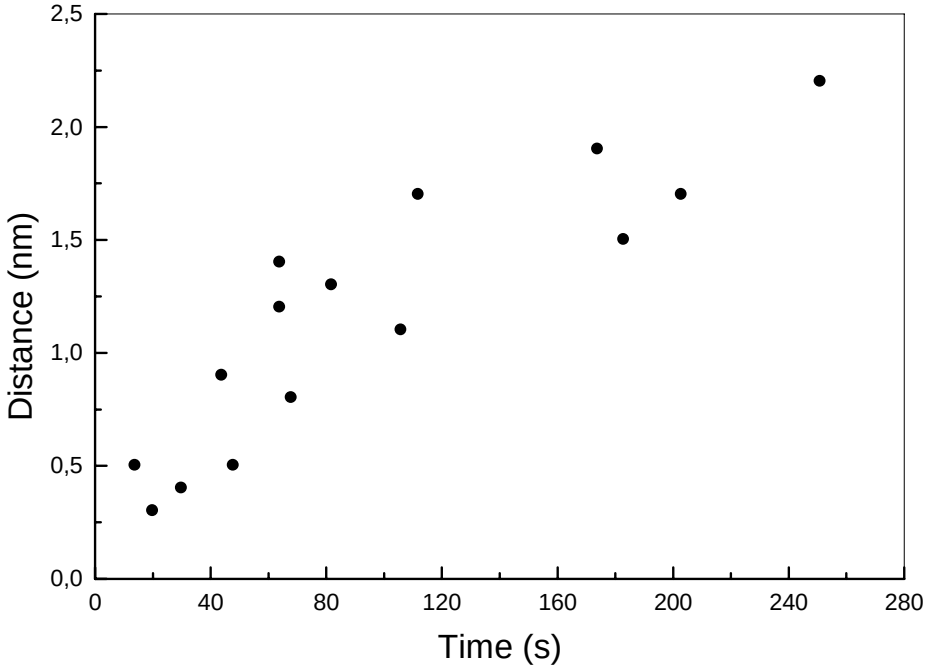

Figure 6.7: One-dimensional migration length measured from micrographs as a function of time for Pt atoms along the open edge of the graphene layer (labelled with "E" in Figure 6.5) at 600°C.

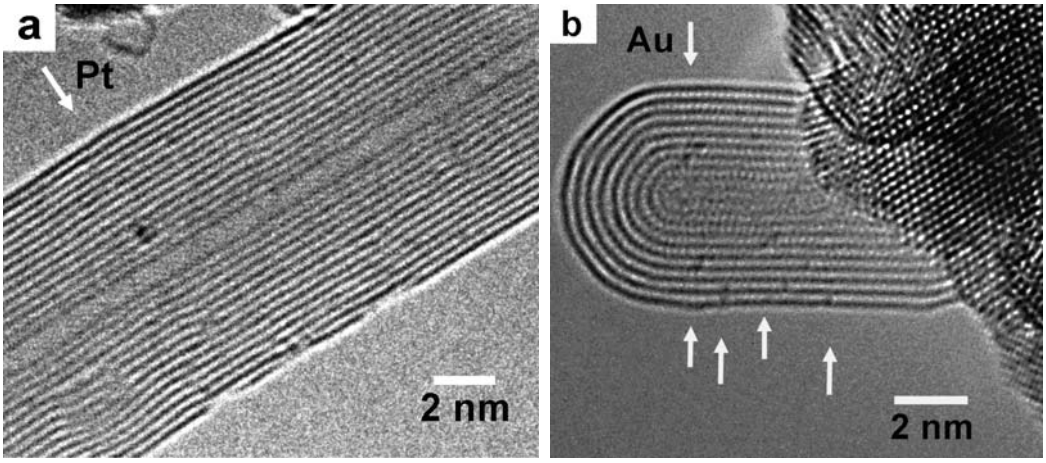

Figure 6.8: Pt (a) and Au (b) atoms in MWCNTs. The metal atoms are arrowed. The nanotube in (b) is attached to a Au crystal.

The migrations of Au and Pt atoms in MWCNTs were also studied. Figure 6.8 (a) shows 2 – 4 Pt atoms in the layers of a MWCNT at 600°C. It is difficult to determine

the exact number of atoms because a migration of the atoms during the exposure of the image cannot be excluded in this case. Figure 6.8 (b) shows a MWCNT whose right end is terminated by a Au crystal. It is clear that in the layers of the MWCNT there are several Au atoms which migrated from the Au crystal at the right end, and the contrast of the Au atoms mostly overlaps with the lattice fringes of the tube wall. The migration of the metal atoms along the circumference of the MWCNT cannot be determined unambiguously because of projection effects, but a diffusion in the axial direction can be quantified. Another feature in Figure 6.8 (b) is the bonding between the nanotube and the Au crystal. Although the spacing of the (002) planes in the nanotube (0.34 nm) is much lager than the (111) spacing in Au (0.23 nm), a semi-coherent interface appears in some regions.

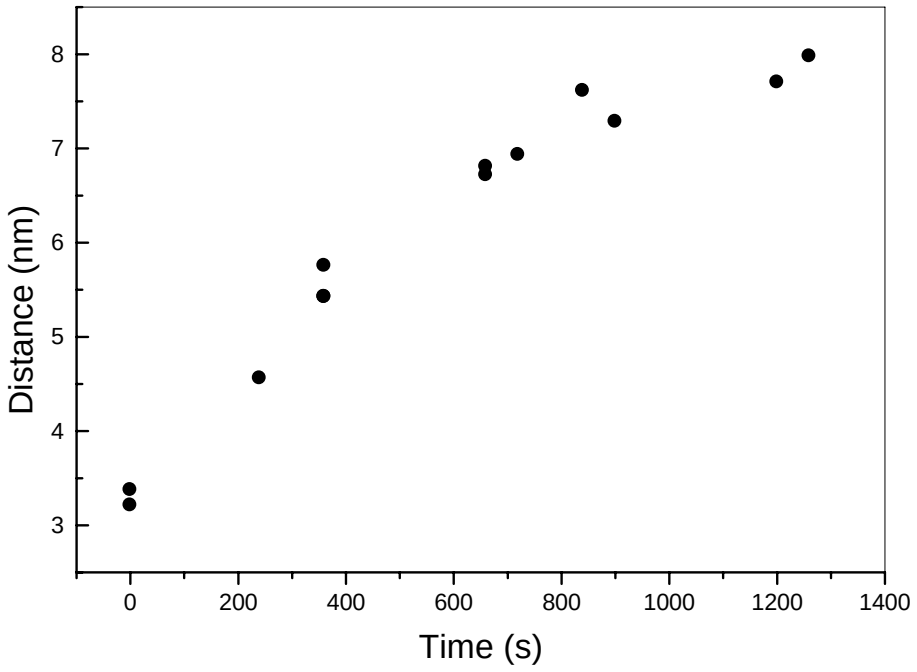

Figure 6.9: Migration length measured from micrographs as a function of time for Pt atoms along the axial direction in the layers of a MWCNT at 600°C.

Figure 6.9 shows the migration distance for Pt atoms along the axial direction in the layers of a MWCNT as a function of time. The diffusion coefficient and the corresponding activation energy were obtained to be $2 - 4\times10^{-20}$ m^2/s and approximate 2.3 eV, respectively. However, no reliable data were obtained for Au atoms in nanotubes in the present study.

The range of diffusion coefficients *D* for Pt and Au atoms obtained above are shown in Table 6.1. It is obvious that the diffusion of metal atoms in the curved layers of MWCNTs is faster than in planar graphene. However, surprisingly there is only a minor difference between the two-dimensional diffusivities of metal atoms within the graphene layer and the one-dimensional diffusivity along its edge.

Table 6.1: The diffusion coefficients *D* of Pt and Au at 600°C and 700°C

	D **(m^2/s)** (diffusion coefficient)	***E_a*** **(eV)** (activation energy)
Au @ 600°C *within* the graphene planes	$6\times10^{-22} \sim 2\times10^{-21}$	2.5
Pt @ 600°C *within* the graphene planes	$4\times10^{-22} \sim 1\times10^{-21}$	
Pt @ 700°C *within* the graphene planes	$1\times10^{-21} \sim 7\times10^{-21}$	
Pt @ 600°C in MWCNTs	$2\times10^{-20} \sim 4\times10^{-20}$	2.3
Pt @ 600°C along the open edge of graphene	$3\times10^{-21} \sim 1\times10^{-20}$	

The rather high activation energy of 2.3–2.5 eV indicates a strong covalent bonding between metal and carbon atoms within the graphenic network [123]. An early study has already given the activation energy of 1.2 eV for site exchange of carbon atoms (self-diffusion) in graphene [51]. It is obvious that the migration of metal atoms in the network is several orders of magnitude slower than the migration of carbon atoms. More importantly, a surface migration mechanism of the observed atoms can be

excluded, since early studies show that the activation energies of surface migration for Pt and Au are 0.14 (theoretical value) [123] and 0.28 (experimental value) [132] eV, respectively. Although the measurement of the displacement distances in the present study are not very precise and influenced by the statistics of diffusion, an activation energy of smaller than 2 eV can be safely excluded because the atoms would migrate much too fast to be visible in TEM images with such low activation energy. Of course, an additional mechanism of faster diffusion (such as surface diffusion) may also occur, but is not detectable by TEM. The upper limit of detectability would be about 2.8 eV, where the atoms would remain immobile within the observation times of our study.

Although the *in-situ* TEM experiments hardly permit the direct observation of the diffusion mechanism, several conclusions can be drawn. In the absence of vacancies, there are no interstitial sites for foreign atoms in a monolayer of graphene, because the center of a hexagon would be extremely unfavourable. Hence, it has to be assumed that the metal atoms are located on either single or multiple vacancies in the graphene layer. On one hand, as mentioned above, no clear off-plane positions were observed in the present study, which indicates that the metal atoms are located in double or triple vacancies. On the other hand, the metal atoms appear to be located on regular lattice positions (in Figure 6.2 (b)), which indicates that the metal atoms should be located in single vacancy. In any case, diffusion should occur by site exchange of a carbon and a metal atom. However, there should be no vacancies in thermal equilibrium at the temperatures of our experiments, including single and multiple vacancies, because of a high formation energy of more than 7 eV. Therefore, it is more reasonable that carbon atoms are replaced by metal atoms, i.e., metal atoms are on substitutional sites. Such a replacement mechanism may also play a role in the catalytic formation and growth of carbon nanotubes [42]. So the activation energies derived from our experiments can also be considered as those for the two-dimensional diffusion of Au or Pt atoms within a graphene layer by site exchange with carbon atoms. Although the C–Au interaction is weaker than the C–Pt interaction [122], it is surprising that only a small difference between the diffusivity for Au and Pt was obtained in our study. A lower formation

energy and a higher diffusivity for vacancies in curved graphenic structures should be responsible for the slightly smaller activation energy of metal diffusion in the layers of MWCNTs.

Undoubtedly, the influence of the unavoidable electron irradiation on the migration behaviour of metal atoms has to be considered in this experiment. It is well known that the displacement of carbon atoms induced by irradiation can lead to vacancies in the graphitic layers [20]. By assuming a displacement threshold of 15 eV and a beam current density of approximately 30 A/cm^2, one displacement of every carbon atom in 180 seconds is obtained with the formula (6.4) [17]:

$$p = \sigma j \tag{6.4}$$

where p is the displacement rate of each atom, σ is the displacement cross section and j is the beam current density. σ is taken as 30 barns with a displacement threshold of 15 eV [17]. However, the annealing rate of the vacancies and the interstitials is quite high in the graphenic layers because of their low migration barrier, for example, in SWCNTs E_a = 1.2 eV for vacancies and E_a = 0.3–0.8 eV for interstitials [45, 46]. Unlike carbon atoms, the heavy metal atoms can hardly be displaced by the knocks of the electrons. Therefore, electron irradiation should have only minor influence on the migration of metal atoms although the irradiation may slightly enhance the diffusion of the atoms.

Chapter 7 Summary

In the present work, the formation and migration of point defects induced by electron irradiation in carbon nanostructures, including carbon onions, nanotubes and graphene layers, were investigated by *in-situ* TEM. The mobility of carbon atoms normal to the layers in graphitic nanoparticles, the mobility of carbon interstitials inside SWCNTs, and the migration of foreign atoms in graphene layers or in layers of carbon nanotubes were studied. The quantitative analysis of the results gave values for the previously unknown activation energies of these processes.

1. Migration of carbon atoms normal to the layers of carbon nanoparticles

It has been demonstrated earlier that Carbon onions can be in a state of heavy self-compression when irradiated with an electron beam [13, 67]. In the present work, the diffusion of carbon atoms in carbon onions was investigated by annealing carbon onions and observing the relaxation of the compressed clusters in the temperature range of 1200 – 2000^{o}C. Annealing at temperatures above 1500°C leads to a relaxation of the pressure in the centre of the onions by an exchange of atoms between the shells. The formation of an internal hollow of up to 5 nm in diameter with a corresponding expansion of the onions was observed, which made it possible to determine the activation energy for atom migration between graphitic layers. The compression of the onions was preserved and no considerable relaxation occurred after annealing below 1500°C even for several hours. An activation energy of 5.0±0.3 eV was obtained. This rather high activation energy for atom exchange between the layers not only prevents the exchange of carbon atoms between the layers at lower temperature but also explains the high morphological and mechanical stability of graphite nanostructures. Hence, the application of graphitic structures such as nanotubes in materials of high strength is not

limited by diffusional creep up to at least 1200°C. It was also shown that in this work spherical carbon onions, even when they are in a self-compressed state, have a surprising morphological stability at temperatures up to more than 1200°C. This makes them interesting for several applications, e.g., in tribology [133] or coating of nanoparticles. Moreover, the stability of carbon onions with different sizes was also studied and it was found that carbon onions under irradiation showed an increasing stability with decreasing size.

2. Migration of carbon atoms inside single-walled carbon nanotubes

A previous study has qualitatively shown that interstitial carbon atoms can improve the stability of SWCNTs against electron irradiation damage when the channels in the tubes are blocked or filled with carbon atoms [110]. Here, the migration of carbon atoms in SWCNTs was investigated quantitatively by cutting SWCNT bundles repeatedly with a focused electron beam at different temperatures. The mobility of interstitial carbon atoms in SWCNTs was determined by the combination of electron irradiation experiments with kinetic Monte Carlo simulations carried out by collaborators at the University of Helsinki. The irradiation dose which is necessary to cut SWCNT bundles with a focused electron beam was measured as a function of separation between the two cuts at different temperatures. As the cutting speed is related to the migration of displaced carbon atoms trapped inside the tubes and their recombination with vacancies at the second gap, information about the mobility of interstitial carbon atoms is available. A migration barrier of about 0.25 eV was obtained for the diffusion of carbon atoms inside SWCNTs. This is an experimental confirmation of the high mobility of interstitial atoms inside carbon nanotubes, which corroborates previously developed theoretical models of interstitial diffusivity. It is confirmed that nanotubes may act as efficient pipelines for the transport of carbon atoms. It is also of importance in all applications where point defects are created in the tube [23–27, 45, 110] and thermal annealing [109, 134] is used to heal the defect structures.

3. Migration of metal (Au and Pt) atoms in graphene layers and carbon nanotubes

Metal atoms play an important role in technology of carbon nanostructures, especially in the catalytic formation of carbon nanotubes. In the present study, individual Au and Pt atoms in one- or two-layered graphene planes and MWCNTs were monitored in real time at high temperatures by high-resolution TEM. The direct observation of the behavior of Au and Pt atoms in graphenic structures in a temperature range of 600 – 700°C allows us to determine the sites occupied by the metal atoms in the graphene layer and the diffusivities of the metal atoms. It was found that metal atoms were located in single or multiple carbon vacancies, not in off-plane positions, and diffused by site exchange with carbon atoms. Metal atoms showed a tendency to form clusters those were stable for a few seconds. An activation energy of around 2.5 eV was obtained for the in-plane migration of both Au and Pt atoms in graphene (two-dimensional diffusion). The rather high activation energy indicates covalent bonding between metal and carbon atoms. Metal atoms were also observed to diffuse along the open edge of graphene layers (one-dimensional diffusion) with a slightly lower activation energy of about 2.3 eV. It is also found that the diffusion of metal atoms in curved graphenic layers of MWCNTs is slightly faster than in planar graphene. The knowledge of the bonding between metal and carbon atoms and of the location and diffusivity of metal atoms in graphene layers allows the refinement of the models of catalytic growth of carbon nanotubes and other nanostructures.

References

[1] H. W. Kroto, J. R. Heath, S. C. O'Brien, R. F. Curl and R. E. Smalley. C_{60}: Buckminsterfullerene. *Nature*, **318**,162 (1985).

[2] J. Baggott. *Perfect symmetry: the accidental discovery of buckminsterfullerene*. Oxford University Press, 1994.

[3] H. Aldersey-Williams. *The most beautiful molecule.* Aurum Press, London, 1995.

[4] H. W. Kroto. Symmetry, space, stars and C60. (Nobel lecture) *Rev. Mod. Phys.*, **69**, 703 (1997).

[5] R. E. Smalley. Discovering the fullerenes. (Nobel lecture) *Rev. Mod. Phys.*, **69**, 723(1997).

[6] S. Iijima. Helical microtubules of graphitic carbon. *Nature*, **354**, 56 (1991).

[7] D. Ugarte. Curling and closure of graphitic networks under electron-beam irradiation. *Nature*, **359**, 707 (1992).

[8] P. J. F. Harris. *Carbon Nanotubes and Related Structures.* Cambridge University Press, Cambridge, 1999.

[9] R. H. Baughman, A. A. Zakhidov, and W. A. de Heer. Carbon Nanotubes--the Route Toward Applications. *Science*, **297**, 787 (2002).

[10] M. Wilkens. *Proceedings of the 5th conference on high voltage electron microscopy,* Kyoto, edited by T. Imura and H. Hashimoto (1977).

[11] M. Makin. *Proceedings of the 9th international conference on electron microscopy,* Toronto, edited by J. M. Sturgess (1978).

[12] K. Urban. Radiaion-induced processes in experiments carried out *in-situ* in the high-voltage electron microscope. *Phys. Status Solidi* (a), **56**, 157 (1979).

[13] F. Banhart and P. M. Ajayan. Carbon onions as nanoscopic pressure cells for diamond formation. *Nature*, **382**, 433 (1996).

[14] L. D. Marks. Experimental studies of small particle structures. *Rep. Prog. Phys.*, **57**, 603 (1994).

[15] P. A. Thrower and R. M. Mayer. Point defects and self-diffusion in graphite. *Phys. Stat. Sol.* (a), **47**, 11 (1978).

[16] B. T. Kelly. *The physics of graphite*. Applied Science, London, 1981.

[17] F. Banhart. Irradiation effects in carbon nanostructures. *Rep. Prog. Phys.*, **62**, 1181 (1999).

[18] F. Banhart. Formation and transformation of carbon nanoparticles under electron irradiation. *Phil. Trans.* A, **362**, 2205 (2004).

[19] F. Banhart. Irradiation of carbon nanotubes with a focused electron beam in the electron microscope. *J. Mat. Sci.*, 11, 4505 (2006).

[20] A. V. Krasheninnikov and F. Banhart. Engineering of nanostructured carbon materials with electron or ion beams. *Nature Mater.*, **6**, 723 (2007).

[21] F. Banhart (Editor). *In-situ Electron Microscopy at High Resolution*. World Scientific Singapore, 2008.

[22] B. W. Smith, M. Monthioux and D. E. Luzzi. Encapsulated C_{60} in carbon nanotubes. *Nature*, **396**, 323 (1998).

[23] A. Kis, G. Gsányi, J. P. Salvetat, T. N. Lee, E. Couteau, A. J. Kulik, W. Benoit, J. Brugger and L. Forró. Reinforcement of single-walled carbon nanotube bundles by intertube bridging. *Nature Mater.*, **3**, 153 (2004).

[24] C. Gómez-navarro, P. J. De Pablo, J. Gómez-Herrero, B. Biel, F. J. Garcia-Vidal, A. Rubio and F. Flores. Tuning the conductance of single-walled carbon nanotubes by ion irradiation in the Anderson localization regime. *Nature Mater.*, **4**, 534 (2005).

[25] M. Terrones, H. Terrones, F. Banhart, J.-C. Charlier and P. M. Ajayan. Coalescence of single-walled carbon nanotubes. *Science*, **288**, 1226 (2000).

[26] A. Hashimoto, K. Suenaga, A. Gloter, K. Urita and S. Iijima. Direct evidence for atomic defects in graphene layers. *Nature*, **430**, 870 (2004).

[27] W. Mickelson, S. Aloni, W. Q. Han, J. Cumings and A. Zettl. Packing C_{60} in Boron Nitride nanotubes. *Science*, **300**, 467 (2003).

[28] M. Terrones, F. Banhart, N. Grobert, J.-C. Charlier, H. Terrones and P. M. Ajayan. Molecular junctions by joining single-walled carbon nanotubes. *Phys. Rev. Lett.*,

89, 075505 (2002).

[29] L. Sun, F. Banhart, A. V. Krasheninnikov, J. A. Rodríguez-Manzo, M. Terrones and P. M. Ajayan. Carbon nanotubes as high-pressure cylinders and nanoextruders. *Science*, **300**, 1199 (2006).

[30] P. Wesolowski, Y. Lyutovich, F. Banhart, H. D. Carstanjen and H. Kronmüller. Formation of diamond in carbon onions under Mev ion irradiation. *Appl. Phys. Lett.*, **71**, 1948 (1997).

[31] Y. Lifshitz, Th. Köhler, Th. Frauenheim, I. Guzmann, A. Hoffman, R. Q. Zhang, X. T. Zhou and S. T. Lee. The mechanism of diamond nucleation from energetic species. *Science*, **297**, 1531 (2002).

[32] Y. Yao, M. Y. Liao, Th. Köhler, Th. Frauenheim, R. Q. Zhang, Z. G. Wang, Y. Lifshitz and S. T. Lee. Diamond nucleation by energetic pure carbon bombardment. *Phys. Rev.* B, **72**, 035402 (2005).

[33] J. X. Li and F. Banhart. The engineering of hot carbon nanotubes with an electron beam. *Nano. Lett.*, **4**, 1143 (2004).

[34] H. Stahl, J. Appenzeller, R. Martel, Ph. Avouris and B. Lengeler. Intertube coupling in ropes of simgle-wall carbon nanotubes. *Phys. Rev. Lett.*, **85**, 5186 (2000).

[35] B. Q. Wei, J. D'Aecy-Gall, P. M. Ajayan and G. Ramanath. Tailoring structure and electrical properties of carbon nanotubes using kilo-electron-volt ions. *Appl. Phys. Lett.*, **83**, 3581 (2003).

[36] M. S. Raghuveer, P. G. Ganesan, J. D'Arcy-Gall and G. Ramanath. Nanomachining carbon nanotubes with ion beams. *Appl. Phys. Lett.*, **84**, 4484 (2004).

[37] P. Esquinazi, D. Spemann, R. Höhne, A. Setzer, K.-H. Han and T. Butz. Induced magnetic ordering by proton irradiation in graphite. *Phys. Rev. Lett.*, **91**, 227201 (2003).

[38] S. Talapatra, P. G. Ganesan, T. Kim, R. Vajtai, M. Huang, M. Shima, G. Ramanath, D. Srivastava, S. C. Deevi and P. M. Ajayan. Irradiation-induced magnetism in carbon nanostructures. *Phys. Rev. Lett.*, **95**, 097201 (2005).

[39] D. Cherns, F. J. Minter and R. S. Nelson. Sputtering in the high voltage electron

microscope. *Nucl. Instr. Meth.*, **132**, 369 (1976).

[40] W. A. McKinley and A. Feshbach. The coulomb scattering of relativistic electrons by neclei. *Phys. Rev.*, **74**, 1759 (1948).

[41] H. Föll and B. Kolbesen. Agglomerate von Zwischengitteratomen (Swirl-Defekte) in Slizium-ihre Bedeutung für Grundlagenforschung und Technologie. *Jahrbuch der Akademie der Wissenschaften in Göttingen*, 1976.

[42] Y. H. Lee, S. G. Kim and D. Tománek. Catalytic growth of single-wall carbon nanotubes: an *ab initio* study. *Phys. Rev. Lett.*, **78**, 2393 (1997).

[43] A. V. Krasheninnikov, K. Nordlund, P. O. Lehtinen, A. S. Foster, A. Ayuela and R. M. Nieminen. Adsorption and migration of carbon adatoms on carbon nanotubes: density-functional *ab initio* and tight-binding studies. *Phys. Rev.* B, **69**, 073402 (2004).

[44] A. Maiti, C. J. Brabec and J. Bernholc. Kinetics of metal-catalyzed growth of single-walled carbon nanotubes. *Phys. Rev.* B, **55**, R6097 (1997).

[45] F. Banhart, J. X. Li and A. V. Krasheninnikov. Carbon nanotubes under electron irradiation: stability of the tubes and their action as pipes for atom transport. *Phys. Rev.* B, **71**, 241408(R) (2005).

[46] A. V. Krasheninnikov, P. O. Lehtinen, A. S. Foster and R. M. Nieminen. Bending the rules: contrasting vacancy energetics and migration in graphite and carbon nanotubes. *Chem. Phys. Lett.*, **418**, 132 (2006).

[47] L. Li, S. Reich and J. Robertson. Defect energies of graphite: density-functional calculations. *Phys. Rev.* B, **72**, 184109 (2005).

[48] R. H. Telling, C. P. Ewels, A. A. El-Barbary and M. I. Heggie. Wigner defects bridge the graphite gap. *Nature Mater.*, **2**, 333 (2003).

[49] A. K. Geim and K.S. Novoselov. The rise of graphene. *Nature Mater.*, **6**, 183 (2007).

[50] M. S. Dresselhaus, G. Dresselhaus and P. C. Eklund. *Science of fullerenes and carbon nanotubes*. San Diego: Academic Press, 1996.

[51] P. J. F. Harris, S. C. Tsang, J. B. Claridge and M. L. H. Green. High-resolution

electron microscopy studies of a microporous carbon produced by arc-evaporation. *J. Chem. Soc. Faraday Trans.*, **90**, 2799 (1994).

[52] M. S. Zwanger, F. Banhart and A. Seeger. Formation and decay of spherical concentric-shell carbon clusters. *J. Cryst. Growth*, **163**, 445 (1996).

[53] L.-C. Qin and S. Iijima. Onion-like graphitic particles produced from diamond. *Chem. Phys. Lett.*, **262**, 252 (1996).

[54] H. W. Kroto. Carbon onions introduced a new flavour to fullerene studies. *Nature*, **359**, 670 (1992).

[55] M. S. Zwanger and F. Banhart. The structure of concentric-shell carbon onions as determined by high-resolution electron microscopy. *Philos. Mag.* B, **72**, 149 (1995).

[56] E. T. Thostenson, Z. Ren and T.-W. Chou. Advances in the science and technology of carbon nanotubes and their composites: a review. *Composites Science and Technology*, **61**, 1899 (2001).

[57] Y. Hu, O. Shenderova, Z. Hu, C. W. Padgett and D. W. Brenner. Carbon nanostructures for advanced composites. *Rep. Prog. Phys.*, **69**, 1847 (2006).

[58] S. G. Louie. Electronic properties, junctions and defects of carbon nanotubes. *Top. Appl. Phys.*, **80**, 113 (2001).

[59] N. Hamada, S. Sawada and A. Oshiyama. New one-dimensional conductors: graphite microtubules. *Phys. Rev. Lett.*, **68**, 1579 (1992).

[60] R. Saito , M. Fujita, G. Dresselhaus and M. S. Dresselhaus. Electronic structure of chiral graphene tubules. *Appl. Phys. Lett.*, **60**, 2204 (1992).

[61] J. W. Mintmire, B. I. Dunlap and C. T. White. Are fullerene tubules metallic? *Phys. Rev. Lett.*, **68**, 631 (1992).

[62] C. H. Xu, C. Z. Wang, C. T. Chan and K. M. Ho. Simulated-annealing studies of structural trends in carbon clusters. *Phys. Rev.* B, **47**, 9878 (1993).

[63] A. A. El-Barbary, R. H. Telling, C. P. Ewels, M. I. Heggie and P. R. Briddon. Structure and energetics of the vacancy in graphite. *Phys. Rev.* B, **68**, 144107 (2003).

[64] E. Kaxiras and K. C. Pandey. Energetics of defects and diffusion mechanisms in graphite. *Phys. Rev. Lett.*, **61**, 2693 (1988).

[65] P. O. Lehtinen, A. S. Foster, A. Ayuela, A. Krasheninnikov, K. Nordlund and R. M. Nieminen. Magnetic properties and diffusion of adatoms on a graphene sheet. *Phys. Rev. Lett.*, **91**, 017202 (2003).

[66] A. P. Burden and J. Hutchsion. Real-time observation of fullerene generation in a modified electron microscope. *J. Cryst. Growth*, **158**, 185 (1996).

[67] F. Banhart, T. Füller, Ph. Redlich and P. A. Ajayan. The formation, annealing and self-compression of carbon onions under electron irradiation. *Chem. Phys. Lett.*, **269**, 349 (1997).

[68] K. Urita, K. Suenaga, T. Sugai, H. Shinohara and S. Iijima. *In-situ* observation of thermal relaxation of interstitial-vacancy pair defects in a graphite gap. *Phys. Rev. Lett.*, **94**, 155502 (2005).

[69] P. M. Ajayan, V. Ravikumar and J.-C. Charlier. Surface reconstructions and dimensional changes in single-walled carbon nanotubes. *Phys. Rev. Lett.*, **81**, 1437 (1998).

[70] N. G. Chopra, F. M. Ross and A. Zettl. Collapsing carbon nanotubes with an electron beam. *Chem. Phys. Lett.*, **256**, 241 (1996).

[71] A. V. Krasheninnikov and K. Nordlung. Irradiation effects in carbon nanotubes. *Nucl. Instr. Meth. Phys. Res.* B, **216**, 355 (2004).

[72] L. Sun, J. A. Rodriguez-Manzo and F. Banhart. Elastic deformation of nanometer-sized metal crystals in graphitic shells. *Appl. Phys. Lett.*, **89**, 263104 (2006).

[73] M. Zaiser. Self-compression and diamond nucleation in irradiated carbon onions-a theoretical model. *Mater. Res. Soc. Symp. Proc.*, **540**, 243 (1999).

[74] F. Banhart. The transformation of graphitic onions to diamond under electron irradiation. *J. Appl. Phys.*, **81**, 3440 (1997).

[75] A. Thess. R. Lee, P. Nikolaev, H. Dai, P. Petit, J. Robert, C. Xu, Y. H. Lee, S. G. Kim, A. G. Rinzler, D. T. Colbert, G. E. Scuseria, D. Tománek, J. E. Fischer and R.

E. Smalley. Crystalline ropes of metallic carbon nanotubes. *Science*, **273**, 483, (1996).

[76] T. Guo, P. Nikolaev, A. G. Rinzler, D. Tománek, D. T. Colbert and R. E. Smalley. Self-assembly of tubular fullerenes. *J. Phys. Chem.*, **99**, 10694 (1995).

[77] T. Guo, P. Nikolaev, A. Thess, D. T. Colbert and R. E. Smalley. Catalytic growth of single-walled nanotubes by laser vaporization. *Chem. Phys. Lett.*, **243**, 49 (1995).

[78] M. José-Yacamán, M. Miki-Yoshida, L. Rendón and J. G. Santiesteban. Catalytic growth of carbon microtubules with fullerene structure. *Appl. Phys. Lett.*, **62**, 657 (1993).

[79] M. Endo, K. Takeuchi, S. Igarashi, K. Kobori, M.Shiraishi and H. W. Kroto. The production and structure of pyrolytic carbon nanotubes (PCNTs). *J. Phys. Chem. Solids*, **54**, 1841 (1993).

[80] H. Dai, A. G. Rinzler, P. Nikolaev, A. Thess, D. T. Colbert and R. E. Smalley. Single-wall nanotubes produced by metal-catalyzed disproportionation of carbon monoxide. *Chem. Phys. Lett.*, **260**, 471 (1996).

[81] Y. Ando, X. Zhao, T. Sugai and M. Kumar. Growing carbon nanotubes. *Materials Today*, **7**, 22 (2004).

[82] T. W. Ebbesen and P. M. Ajayan. Large-scale synthesis of carbon nanotubes. *Nature*, **358**, 220 (1992).

[83] T. W. Ebbesen, H. Hiura, J. Fujita, Y. Ochiai, S. Matsui and K. Tanigaki. Patterns in the bulk growth of carbon nanotubes. *Chem. Phys. Lett.*, **209**, 83 (1993).

[84] Y. Saito, T. Yoshikawa, M. Tomita and T. Hayashi. Growth and structure of graphitic tubules and polyhedral particles in arc-discharge. *Chem. Phys. Lett.*, **204**, 277 (1993).

[85] G. H. Taylor, J. D. Fitzgerald, L. Pang and M. A. Wilson. Cathode deposits in fullerene formation-microstructural evidence for independent pathways of pyrolytic carbon and nanobody formation. *J. Cryst. Growth*, **135**, 157 (1994).

[86] S. Seraphine, D. Zhou, J. Jiao, J. C. Withers and R. Loufty. Effect of processing conditions on the morphology and yield of carbon nanotubes. *Carbon*, **31**, 685

(1993).

[87] Y. Ando and S. Iijima. Preparation of carbon nanotubes by arc-discharge evaporation. *Jpn. J. Appl. Phys.*, **32**, L107 (1993).

[88] D. S. Bethune, C. H. Klang, M. S. de Vries, G. Gorman, R. Savoy, J. Vazquez, R. Beyers. Cobalt-catalysed growth of carbon nanotubes with single-atomic-layer walls. *Nature*, **363**, 605 (1993).

[89] S. Iijima and T. Ichihashi. Single-shell carbon nanotubes of 1-nm diameter. *Nature*, **363**, 603 (1993).

[90] D. B.Williams and C. B. Carter. *Transmission electron microscopy*. vol.: **1–4**. Plenum Press, New York, 1996.

[91] G. R. Hennig. Diffusion of Boron in graphite. *J. Chem. Phys.*, **42**, 1167 (1965).

[92] F. S. Feates. The diffusion of carbon in single crystal graphite. *J. Nucl. Mater.*, **27**, 325 (1968).

[93] C. H. Xu, C. L. Fu and D. F. Pedraza. Simulations of point-defect properties in graphite by a tight-binding-force model. *Phys. Rev.* B, **48**, 13273 (1993).

[94] Y. Ma. Simulation of interstitial diffusion in graphite. *Phys. Rev.* B, **76**, 075419 (2007).

[95] I. Suarez-Martinez, A. A. EI-Barbary, G. Savini and M. I. Heggie. First-principles simulations of Boron diffusion in graphite. *Phys. Rev. Lett.*, **98**, 015501 (2007).

[96] G.-D. Lee, C. Z. Wang, E. Xoon, N.-M. Hwang, D.-Y. Kim and K.-M. Ho. Diffusion, coalescence, and reconstruction of vacancy defects in graphene layers. *Phys. Rev. Lett.*, **95**, 205501 (2005).

[97] R. G. Amorim, A. Fazzio, A. Antonelli, F. D. Novaes and A. J. R. da Silva. Divacancies in graphene and carbon nanotubes. *Nano Lett.*, **7**, 2459 (2007).

[98] C. Jin, K. Suenaga and S. Iijima. Vacancy migrations in carbon nanotubes. *Nano Lett.*, **8**, 1127 (2008).

[99] J. Y. Huang, S. Chen, Z. Q. Wang, K. Kempa, Y. M. Wang, S. H. Jo, G. Chen, M. S. Dresselhaus and Z. F. Ren. Superplastic carbon nanotubes. *Nature*, **439**, 281 (2006).

[100] J. Y. Huang, F. Ding and B. Yakobson. Dislocation dynamics in multiwalled carbon nanotubes at high temperatures. *Phys. Rev. Lett.*, **100**, 035503 (2008).

[101] T. D. Yuzvinsky, W. Mickelson, S. Aloni, G. E. Begtrup, A. Kis and A. Zettl. Shrinking a carbon nanotube. *Nano Lett.*, **6**, 2718 (2006).

[102] H. R. Gutiérrez, U. J. Kim, J. P. Kim and P. C. Eklund. Thermal conversion of bundled carbon nanotubes into graphitic ribbons. *Nano Lett.*, **5**, 2195 (2005).

[103] M. J. López, A. Rubio, J. A. Alonso, S. Lefrant, K. Méténier and S. Bonnamy. Patching and Tearing single-wall carbon-nanotube ropes into multiwall carbon nanotubes. *Phys. Rev. Lett.*, **89**, 255501 (2002).

[104] S. Iijima. Direct observation of the tetrahedral bonding in graphitized carbon black by high resolution electron microscopy. *J. Crystal Growth*, **50**, 675 (1980).

[105] J. Y. Huang. In-situ observation of quasimelting of diamond and reversible graphite-diamond phase transitions. *Nano Lett.*, **7**, 2335 (2007).

[106] M. Terrones and H. Terrones. The role of defects in graphitic structures. *Fullerene Sci. Technol.*, **4**, 517 (1996).

[107] G. Lulli, A. Parisini and G. Mattei. Influence of electron-beam parameters ont eh radiation-induced formation of graphitic onions. *Ultramicroscopy*, **60**, 187 (1995).

[108] H. Terrones, M. Terrones, E. Hernandez, G. Grobert, J.-C. Charlie and P. M. Ayajan. New metallic allotropes of planar and tubular carbon. *Phys. Rev. Lett.*, **84**, 1716 (2000).

[109] K. Suenaga, H. Wakabaya, M. Koshino, Y. Sato, K. Urita and S. Iijima. Imaging active topological defects in carbon nanotubes. *Nature Nanotech.*, **2**, 358 (2007).

[110] F. Banhart, J. X. Li and M. Terrones. Cutting single-walled carbon nanotubes with an electron beam: evidence for atom migration inside nanotubes. *Small*, **1**, 953 (2005).

[111] J. Kotakoski, A. V. Krasheninnikov and K. Nordlund. Kinetic Monte Carlo simulations of the response of carbon nanotubes to electron irradiation. *J. Comput. Theor. Nanosci.*, **4**, 1153 (2007).

[112] V. Meunier, J. Kephart, C. Roland and J. Bernholc. *Ab initio* investigations of

lithium diffusion in carbon nanotube systems. *Phys. Rev. Lett.*, **88**, 075506 (2002).

[113] A. V. Krasheninnikov, F. Banhart, J. X. Li, A. S. Foster and R. M. Nieminen. Stability of carbon nanotubes under electron irradiation: role of tube diameter and chirality. *Phys. Rev.* B, **72**, 125428 (2005).

[114] A. Zobelli, A. Gloter, C. P. Ewels, G. Seifert and C. Colliex. Electron knock-on cross section of carbon and boron nitride nanotubes. *Phys. Rev.* B, **75**, 245402 (2007).

[115] Y. Gan, J. Kotakoski, A. V. Krasheninnikov, K. Nordlund and F. Banhart. The diffusion of carbon atoms inside carbon nanotubes. *New Journal of Physics.* **10,** 023022 (2008).

[116] H. Shioyama. Cleavage of graphite to grapheme. *J. Mater. Sci. Lett.*, **20**, 499 (2001).

[117] L. M. Viculis, J. J. Mack and R. B. Kaner. A chemical route to carbon nanoscrolls. *Science*, **299**, 1361 (2003).

[118] K. S. Novoselov, D. Jiang, F. Schedin, T. J. Booth, V. V. Khotkevich, S. V. Morozov and A. K. Geim. Two-dimensional atomic crystals. *Proc. Nat. Acad. Sci.*, **102**, 10451 (2005).

[119] Y. Zhang, Y. W. Tan, H. L. Stormer and P. Kim. Experimental observation of the quantum Hall effect and Berry's phase in graphene. *Nature*, **438**, 201 (2005).

[120] A. Jorio, M. Dresselhaus and G. Dresselhaus (Eds): *Carbon Nanotubes: Advanced Topics in the Synthesis, Strucure, Properties and Applications*. Springer Topics in Applied Physics Vol. 111, Springer, (2007).

[121] A. Moisala, A. G. Nasibulin and E. I. Kauppinen. The role of metal nanoparticles in the catalytic production of single-walled carbon nanotubes - a review. *J. Phys. Cond. Matter*, **15**, S3011 (2003).

[122] A. Maiti and A. Ricca. Metal-nanotube interactions-binding energies and wetting properties. *Chem. Phys. Lett.*, **395**, 7 (2004).

[123] K. Kong, Y. Choi, B.-H. Ryu, J.-O. Lee and H. Chang. Investigation of metal/carbon-related materials for fuel cell applications by electronic structure

calculations. *Mater. Sci. Eng.* C, **26**, 1207 (2006).

[124] J. H. C. Spence. *Experimental High-Resolution Electron Microscopy*. Oxford University Press: Oxford, 1988.

[125] S. Iijima. Observation of single and clusters of atoms in bright field electron microscopy. *Optik*, **48**, 193 (1977).

[126] N. Tanaka, H. Kimata and T. Kizuka. Time-resolved high-resolution electron microscopy of surface-diffusion of tungsten atoms on MgO (001) surfaces. *J. Electron Microsc.*, **45**, 113 (1996).

[127] F. Banhart, Ph. Redlich and P. M. Ajayan. The migration of metal atoms through carbon onions. *Chem. Phys. Lett.*, **292**, 554 (1998).

[128] J. C. Meyer, A. K. Geim, M. I. Katsnelson, K. S. Novoselov, T. J. Booth and S. Roth. The structure of suspended graphene sheets. *Nature*, **446**, 60 (2007).

[129] R. Saito, T. Matsumoto and K. Nishikubo. Encapsulation of carbides of chromium, molybdenum and tungsten in carbon nanocapsulates by arc-discharge. *J. Crystal Growth*, **172**, 163 (1997).

[130] J. Li and F. Banhart. The deformation of single nanometer-sized metal crystals in graphitic shells. *Adv. Mater.*, **17**, 1539 (2005).

[131] F. Banhart, J.-C. Charlie and P. M. Ajayan. Dynamic behavior of nickel atoms in graphitic networks. *Phys. Rev. Lett.*, **84**, 686 (2000).

[132] R. Anton and I. Scheidereit. *In situ* TEM investigations of dendritic growth of Au particles on HOPG. *Phys. Rev.* B, **58**, 13874 (1998).

[133] R. Tenne. Inorganic nanotubes and fullerene-like nanoparticles. *Nature Nanotech.*, **1**, 103 (2006).

[134] F. Ding, K. Jiao, Y. Lin and B. I. Yakobson. How evaporating carbon nanotubes retain their perfection. *Nano Lett.*, **7**, 681 (2007).

Publications

(1) **Yanjie Gan**, J. Kotakoski, A. V. Krasheninnikov, K. Nordlund and F. Banhart. The diffusion of carbon atoms inside carbon nanotubes. *New Journal of Physics.* **10,** 023022 (2008).

(2) **Yanjie Gan**, Litao Sun and Florian Banhart. One- and two-dimensional diffusion of metal atoms in graphene. *Small*. **4,** 587, (2008).

(3) **Yanjie Gan** and Florian Banhart. The mobility of carbon atoms in graphitic nanoparticles studied by the relaxation of strain in carbon onions. *Advanced Matertials.* (in press).

(4) L. Sun, **Y. Gan**, J.A. Rodriguez-Manzo, M. Terrones, A.V. Krasheninnikov and F. Banhart. In-situ electron irradiation studies of metal-carbon nanostructures. *Proceedings of the 14th European Microscopy Congress*, Vol. **2**: Materials Science, pp. 121-122, Eds.: S. Richter and A. Schwedt, Springer, Berlin 2008.